Squeeze-out and Flow of Pions from 1.15 GeV/nucleon Au + Au

by

Jessica Challinor Kintner

B.A. (DePauw University) 1988
M.S. (University of California, Davis) 1992

DISSERTATION

Submitted in partial satisfaction of the requirements for the degree of

DOCTOR OF PHILOSOPHY

in

PHYSICS

in the

OFFICE OF GRADUATE STUDIES

of the

UNIVERSITY OF CALIFORNIA

DAVIS

Approved:

Committee in charge

1995

Abstract

Transverse flow and out-of-plane squeeze-out have been studied as functions of impact parameter and transverse momentum for pions and protons from the reaction 1.15 GeV/n Au + Au. This work extends previous studies of nucleon flow to pions.

In this thesis, the first S-curves for pions are presented. The behavior of pions will be contrasted with that of protons. It will be shown that the pions exhibit an "anti-flow" behavior, defined as preferiential emission to the side opposite that of the protons, for both π^+ and π^- in peripheral collisions. This effect reverts to positive flow or no flow for central collisions. The magnitude of the observed flow and the cross-over point are reproduced by nuclear transport models, but are not sensitive to the stiffness of the nuclear equation of state.

Nucleon collective flow and squeeze-out are thought to be signatures of compression in the early stage of the reaction process. The pion flow and squeeze-out are believed to be the results of a different mechanism entirely: scattering and absorption by nucleons in the participant region, as well as the target and projectile spectator matter.

Acknowledgments

I would like to thank my advisor, Daniel Cebra, for providing a wonderful atmosphere in which to do exciting physics, and for his wise guidance and perpetual optimism and support. I would also like to thank Paul Brady for guidance and patience early in my graduate career, and for all the opportunities he provided. I am grateful to have been a member of the UCD Nuclear Physics Group. There are others in the group who provided valuable insights and assistance, especially Jim Draper and Juan Romero.

I would also like to thank all the members of the EOS Collaboration without whom this would not have been possible: especially Martin Partlan for stimulating discussion of his results; Dean Chacon for all his help finding plots and pions; and Eric Hjort for all his work on the Plutos.

I am grateful to Hans-Georg Ritter and Gulshan Rai for their leadership of the EOS Collaboration. Without their guidance, much would not have been possible.

I would like to thank Wolfgang Bauer for providing the BUU code and stimulating discussions of the results.

Finally I would like to thank my family: my parents for their constant support and understanding, and Ray for the calm and strength necessary to complete this awesome undertaking.

This work was supported by UC Davis, Associated Western Universities, and the National Science Foundation under grant PHY-91-23301.

Contents

List of Figures

List of Tables

Chapter 1

Introduction

1.1 Overview

This thesis presents a study of directed collective flow and squeeze-out of pions and protons from the reaction $1.15 GeV/n$ Au + Au. The goal of this work is to study pion flow and squeeze-out as a function of impact parameter and transverse momentum and compare and contrast these results with the nucleon collective behavior. This work will present the first $\langle p_x/m \rangle$ vs y spectra, or "S-curves," for pions, and extend and improve the measurements of pion collective effects.

The thesis is organized as follows: Chapter 1 presents an overview of background information and previous measurements in the field; Chapter 2 presents the detector and experimental information; Chapter 3 discusses the data processing up to actual physics analysis; Chapter 4 discusses the detector acceptance effects; Chapter 5 presents the new physics analysis; Chapter 6 presents results; Chapter 7 compares the data to theory; and Chapter 8 discusses conclusions and future work.

1.2 The Nuclear Equation of State

An equation of state for nuclear matter would describe the relationship between Pressure (P), Volume (V), and Temperature (T). In nuclear physics, it is common to use the variables Energy per baryon (W), density (ρ), and Temperature (T). The total energy per nucleon as a function of density and temperature is [Stoc86]:

$$W(\rho, T) = E_T(\rho, T) + E_C(\rho) + W_0 \tag{1.1}$$

where the first term (E_T) is the thermal energy, the second term (E_C) is the compressional energy, and the last term (W_0) is the rest energy of a nucleon at equilibrium density. The thermal part of the energy is defined to be zero at $T = 0$.

$$E_T = 0 \;\text{ for }\; T = 0$$

The rest energy per nucleon at equilibrium density is:

$$W_0 = 923\,MeV$$

This is evaluated excluding the Coulomb energy and the long range part of the Yukawa energy which lead to divergences if infinite systems are considered. This is the origin of the binding energy of 16 MeV/n rather than 8 MeV/n. Thus the value of the rest energy is:

$$W_0 = 939\,MeV - 16\,MeV$$
$$W_0 = 923\,MeV$$

where $939\,MeV$ is the rest mass of a free nucleon, and $16\,MeV$ is the binding energy of the nucleon in a nucleus. It is worth mentioning that infinite nuclear matter is only present at the big bang, supernova, and star interiors. However, local equilibrium is closely approached even on rather short time scales.

Two constraints are known about equation 1.1: $E_C = 0$ for infinitely dilute nuclear matter, or $\rho = 0$, and $E_C(\rho)$ is a minimum for $\rho = \rho_0$. The compressional energy per nucleon, $E_C(\rho)$ is usually considered to be the equation of state (eos) and in finite nuclear matter is modeled as:

$$E_C(\rho) = \alpha(\rho/\rho_0) + \beta(\rho/\rho_0)^\sigma \tag{1.2}$$

where $\sigma > 1$, α is attractive, and β is repulsive. α and β can be fixed by demanding the correct binding energy and equilibrium density, and the third parameter, σ, will be set by the compressibility. This equation is often called the Skyrme parameterization. It is the mean field potential that a nucleon feels as a function of density. This will be important to the theory as discussed in Chapter 7.

Little is known about the nuclear equation of state. In Figure 1.1 the suggested phase diagram for nuclear matter is shown. The only region which has been studied in detail in this diagram is that around ρ_{nm} and $T = 0$. It is difficult to measure

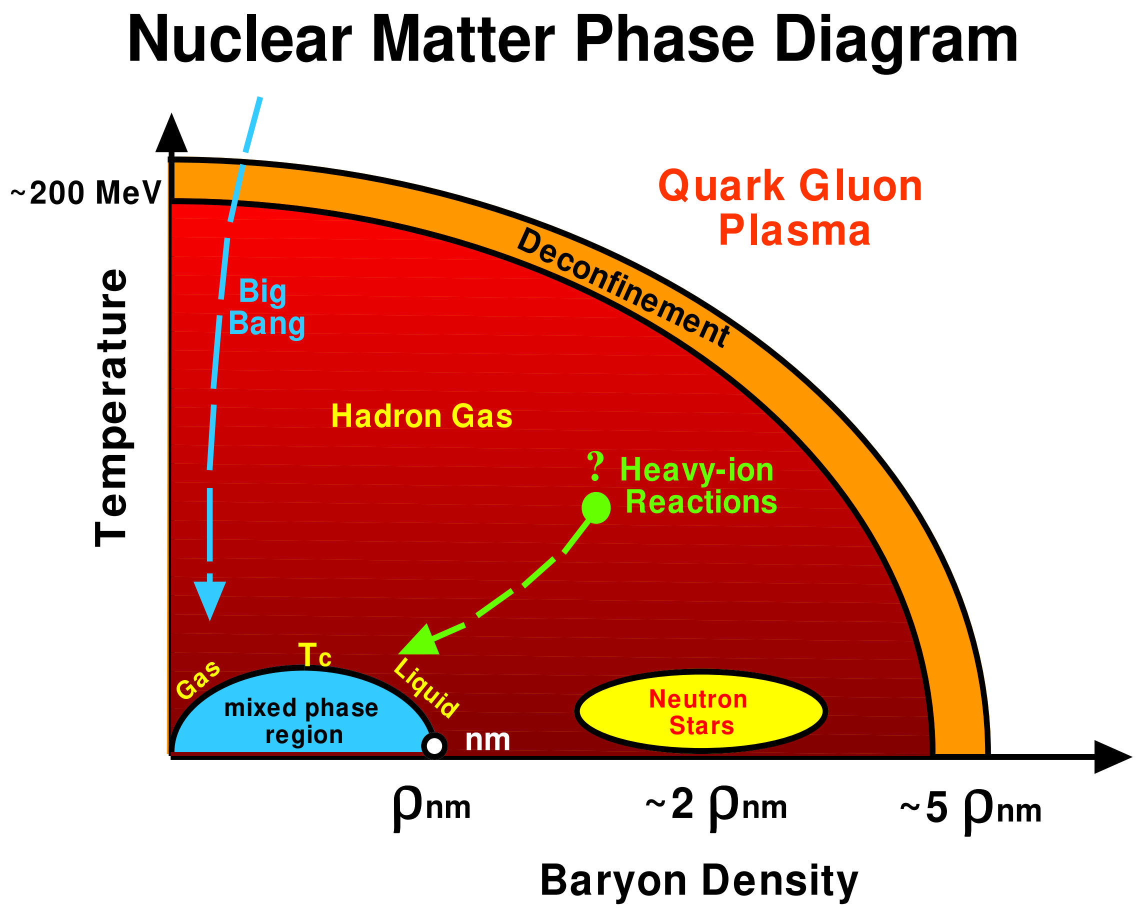

Figure 1.1: Suggested phase diagram of nuclear matter. The only point around which definitive studies have been made is for normal nuclear matter at ρ_{nm} and $T = 0$.

temperature and density of the the collision directly; one cannot simply insert a thermometer into the reaction. In nuclear physics, one does not have the luxury of time that the solid state physicist has to measure these quantities. A typical time scale of compression is on the order of 30 Fm/c, or about $10^{-22}s$.

The compressibility of nuclear matter provides some insight into the equation of state. The compression modulus (or incompressibility), κ, is defined as:

$$\kappa = 9\rho^2 \frac{\partial E_C(\rho)}{\partial \rho^2}\bigg|_{\rho=\rho_0} \tag{1.3}$$

Several methods have been developed to determine κ from experimental information. κ is not directly measurable. One approach to determining the nuclear incompressibility is through the analysis of monopole resonances [Blai76]. The isoscalar monopole vibration is a radial expansion and contraction of a large spherical nucleus, also called the "breathing" mode. From monopole resonance analysis, the incompressibility has been determined to be $\kappa = 210 \pm 30\ MeV$.

It has been found that for $\rho \gg 1.2\rho_0$, the nuclear eos is quite sensitive to κ [Bogu83]. Differences of several hundred percent are possible for variations in κ of only $10 - 20\%$ [Stoc86]. But minimal differences are seen for $\rho < 1.2\rho_0$. Thus, measurements at normal nuclear matter densities do *not* show sensitivity to the nuclear equation of state.

Compressing and heating normal matter only affects the electrons and atoms. How does one compress nuclei? Historically, there was no way to induce large density and temperature changes in the lab. However, astrophysical measurements provided some clues. The incompressibility can be inferred from astrophysical measurements where densities are estimated to be between $3 - 5\rho_0$. The analysis of neutron stars is one such method [Glen86]. Models of neutron stars are correlated with the observed mass and radius to determine the compressibility of nuclear matter. This analysis can only put a lower limit on the incompressibility which is found to be $\kappa > 200\ MeV$.

Another method is the modeling of supernova. Calculations predict that κ should not be greater than $220\,MeV$ or the supernova would not explode after it begins to collapse [Baro85]. These measurements point to a "softer" nuclear equation of state.

Finally, with the development of heavy-ion beams, it has become possible to compress nuclear matter in the laboratory. These new experiments hope to produce a range of compressions up to several times normal nuclear matter density [Sche74]. Experiments at the Bevalac and other heavy ion accelerators have placed the value of the compressibility between either a soft ($\kappa \approx 200\,MeV$) or a hard ($\kappa \approx 380\,MeV$) equation of state.

Analysis of a second generation of experiments designed to do improved measurements of relativistic heavy ion collisions with high statistics is in progress. The EOS experiment at the Bevalac at Lawrence Berkeley Laboratory is one such experiment and is the subject of this thesis.

1.3 Brief Description of Hydrodynamic Models

This discussion follows the arguments of Stöcker and Greiner [Stoc86]. The principle difference between hydrodynamic and other models (such as Cascade and purely statistical models) is the appearance of collective effects such as: stopping, compression, sideward emission, and bounce-off of nuclear matter. In this section, the fluid dynamical model of relativistic heavy ion collisions will be described.

First, the overlap zones of the nuclei are stopped and a strong non-linear shock wave is formed. At this stage, the highest densities and temperatures are created. This is the "compression" phase of the reaction.

The temperature drops as the stopped part undergoes hydrodynamic, quasi-adiabatic expansion. The entropy (S) remains nearly constant. The system expands due to large internal pressure, and at densities on the order of 0.5 to $0.7\rho_0$ collisions between particles cease, and the the hydrodynamic description loses validity. The nuclear fluid breaks up into light fragments: π, p, d, t, ^3He, and α. This is "freeze-out."

These fragments, which are formed at a later stage of the reaction, are the only messengers which can be measured experimentally. These have gone through the later, cooler, freeze-out stage. Thus, any final temperature measurement, such as from the slope of a single particle spectrum, does not give a measure of the initial temperature of the reaction, since during expansion the temperature has dropped.

1.4 Collective Flow and Squeeze-out

In order to quantify the nuclear equation of state, one needs to find messengers from the earlier compression stage. These would be quantities which are integrated in the equations of motion. Density is one such quantity, but it rises early in the reaction and then falls; it has no saturation value. After about 30 Fm/c, the mean kinetic energy does saturate. But the scalar kinetic energy contains limited information. What is of more interest is the quantity F_{ij}, the kinetic flow tensor (see Equation 5.3). This is the "global momentum tensor analysis," or flow analysis. A strong sideward emission should be observed.

To perform this analysis, it is necessary to measure, on an event-by-event basis, the momentum of each charged particle emitted. Then one transforms to the center-of-momentum frame. And then the maximum momentum and kinetic energy flow are determined by performing a principal axis transform. This analysis can be done with 4π detectors such as emulsions, streamer chambers, the Plastic Ball, and now EOS and various experiments at GSI. The main methods are thrust, sphericity, and kinetic energy flow analyses.

Collective flow is thought to be a signature of the compression created during the initial stage of the reaction. The basic picture is this: when nuclear matter is stopped and compressed during the collision, it tries to expand and escape. The matter emitted from the reaction exhibits a characteristic pattern. Matter is observed to be emitted preferentially in the plane of the reaction at a finite angle to the beam axis. This effect is known as "directed collective flow" [Buch84]. Matter is also observed to exhibit a preferential emission perpendicular to the reaction plane, and this is known as "squeeze-out" [Gutb90a]. The squeezed-out matter escapes the reaction without being hindered much by the target or projectile mass and reflects the pure hydrodynamical part of the reaction. Looking at squeezed-out pions may provide an undistorted view of the earliest, densest stage of the reaction.

1.5 Why are Pions of Particular Interest?

Pions are unique in that they are produced particles, not present in the initial colliding nuclei. Cascade calculations have shown that the pions decouple from the baryonic "heat bath" early in the collision, or at the high density stage of the reaction [Cugn80, Stoc82]. The time dependence of total pion production rises rapidly to a maximum at 10 Fm/c and drops to a stable final value by 20 Fm/c [Moli85]. The pion yield approaches an asymptotic value at a time nearly coinciding with the moment of highest compression and temperature. The pions can therefore serve as messengers from the early, high density stage of the reaction.

It is possible to extract temperatures from the pion multiplicity [Hahn85]. New models indicate that the temperature as a function of multiplicity is not as sensitive to the equation of state as once thought. But it has been suggested that for studying the stiffness of the equation of state, pion flow as a function of impact parameter *is* a sensitive probe. And for testing the momentum dependence, pion flow and squeeze-out as a function of transverse momentum may be quite sensitive [Bass95].

Pion flow was first observed by the Plastic Ball in Au + Au collisions [Kean86] and later by the DIOGENE group in 2 GeV/n Ne + Pb collisions [Goss89]. In the DIOGENE experiment, results indicated that pions were emitted preferentially away from the massive target spectator. The nucleons, however, demonstrated an enhanced emission on the projectile side in forward rapidities, and on the target side in backward rapidities. Thus the pions and nucleons seem to be emitted in opposite directions. It has been suggested that the pion flow away from the baryonic matter is caused by either absorption [Li91b] or reflection [Bass93] of the pions initially generated in the direction of the heavy spectator.

More recently, another manifestation of hydrodynamic flow has been observed in the nucleon distributions from heavy-ion reactions. This new observable is out-of-plane "squeeze-out" at center-of-mass rapidities [Gutb90a, Leif93]. Experimental studies at GSI have recently observed squeeze-out for neutral [Vene93] and positively charged [Bril93, Trza94] pions. Pion squeeze-out has been explained as a result of rescattering the pions originally produced in the reaction plane by the cold baryonic spectator matter [Bass93b]. Thus, it is suggested that pions emitted out of the reaction plane at center-of-mass rapidities offer an unobscured view of the earliest phase of the reaction.

1.6 Pion Interactions

In Chapter 7, an overview of available models will be presented, and the results from Chapter 6 will be compared to two models: a BUU model [Li91] and an IQMD model [Bass95]. In both of these models, pion production is extremely important, and both authors cite the work of VerWest and Arndt [VerW82] as their source of pion production cross section information. VerWest and Arndt have neatly summarized the available data. The relevant plots are reproduced here. The fits shown are VerWest and Arndt's parameterization, and the data is from reference [Byst78].

Figure 1.2: Reaction cross sections for the reactions $pp \Rightarrow pp\pi^0$ and $pp \Rightarrow pn\pi^+$

Figure 1.4: Cross section for $np \Rightarrow nn\pi^+ + pp\pi^-$.

Figure 1.3: Cross sections for the reactions $pp \Rightarrow \pi^+d$ and $np \Rightarrow \pi^0d$.

Figure 1.5: Cross sections for the reactions $np \Rightarrow np\pi^0 + d\pi^0$ and $np \Rightarrow np\pi^0$.

Figure 1.2 shows the reaction cross sections for reactions $pp \Rightarrow pp\pi^0$ and $pp \Rightarrow pn\pi^+$. Figure 1.3 shows the cross sections for the reactions $pp \Rightarrow \pi^+ d$ and $np \Rightarrow \pi^0 d$. Figure 1.4 shows the cross section for $np \Rightarrow nn\pi^+ + pp\pi^-$. Figure 1.5 shows the reaction cross sections for $np \Rightarrow np\pi^0 + d\pi^0$ and $np \Rightarrow np\pi^0$. Finally, the total reaction cross sections for single pion production from pp and np scattering are shown in Figure 1.6. In all of the above figures, T_L is the kinetic energy of the projectile in the laboratory frame.

There are no nn reactions shown here, but Clebsch-Gordan coefficients can be used to show that

$$\sigma(nn \Rightarrow np\pi^-) = \sigma(pp \Rightarrow pn\pi^+) \tag{1.4}$$

$$\sigma(np \Rightarrow pp\pi^-) = \sigma(np \Rightarrow nn\pi^+) \tag{1.5}$$

To get a first order estimate of the $\pi^-{:}\,\pi^+$ ratio, one can consider only the four reactions in Equations 1.4 and 1.5. Using combinatorics, one expects the ratio of $pp{:}pn{:}nn$ reactions to be $(79 \times 79) : 2(79 \times 118) : (118 \times 118)$. There are 79×79 possible ways to have pp in $^{197}_{79}\mathrm{Au} + {}^{197}_{79}\mathrm{Au}$, and similarly 118×118 ways to have nn. The combinatoric ratio is multiplied by the relative cross sections $\sigma_{pp}{:}\sigma_{np}{:}\sigma_{nn}$. The ratio $\sigma_{pp}{:}\sigma_{nn}$ (1:1) is given in Equation 1.4. The ratio $\sigma(pp \Rightarrow pn\pi^+)$ to $\sigma(np \Rightarrow pp\pi^- + nn\pi^+)$ can be inferred from Figures 1.2 and 1.4 to be about 18:5. So, the scaled ratios from all of the above information indicates a ratio of $\pi^-{:}\,\pi^+$ of $1.87 : 1$. This is slightly higher than the EOS experimental data suggests. In Chapter 7, scattering and absorption will be discussed in more detail, and it will be suggested that, due

Figure 1.6: The total reaction cross sections for single pion production from pp and np scattering.

to the excess neutrons expected in the participant ("fireball") region, more π^- are absorbed than π^+. Multiplicities from Figure 7.1 can be summed to show that EOS data results in a $\pi^-:\pi^+$ ratio of about $1.5:1$.

A distinction will be made between direct pion production ($NN \Rightarrow NN\pi$), and pion production via the Δ resonance ($NN \Rightarrow N\Delta \Rightarrow NN\pi$). The previous figures (1.2 – 1.6) include both processes since there is no observable difference in the final products. In the Bevalac energy range, Δ decay into a pion ($\Delta \Rightarrow N\pi$) is the most important contribution to the pion yield. Shown in Figure 1.7 are the contributions of various processes to the pion yield as a function of bombarding energy. It is clear that near the 1 GeV/n energy range, the Δ resonance dominates.

Pion interactions with nucleons will be discussed in more detail in Chapter 7. However, it is useful to see the cross section of pion interactions with nucleons here as

Figure 1.7: Various contributions to the pion yields for a C + C reaction. Dotted line: Δ resonance; dashed line: free pion gas; solid line: Bose condensed pions; dashed-dotted: heavy resonances [Hahn85].

a function of energy. Figure 1.8 [Perk87] shows the variation of total cross section for π^+ and π^- on protons with incident pion energy. The symbol Δ refers to resonances of $I = \frac{3}{2}$; N refers to $I = \frac{1}{2}$. In particular, the $\Delta(1232)$ is of most importance in this energy range [Stoc86]. Shown in Figure 1.9 is a more detailed energy dependence of the π^+p cross section for the $\Delta(1232)$ resonance. Information about the pions on neutrons can be inferred from isospin Clebsch-Gordan coefficients as follows:

$$\begin{array}{ccc}
\pi p \text{ Reaction} & \pi n \text{ Reaction} & \text{Relative cross section} \\
\sigma(\pi^+ p \Rightarrow \pi^+ p) & \sigma(\pi^- n \Rightarrow \pi^- n) & 9 \\
\sigma(\pi^- p \Rightarrow \pi^- p) & \sigma(\pi^+ n \Rightarrow \pi^+ n) & 1 \\
\sigma(\pi^- p \Rightarrow \pi^0 n) & \sigma(\pi^+ n \Rightarrow \pi^0 p) & 2
\end{array} \tag{1.6}$$

Figure 1.8: Variation of total cross section for π^+ and π^- on protons with incident pion energy. The symbol Δ refers to resonances of $I = 3/2$; N refers to $I = 1/2$ [Perk87].

Figure 1.9: The π^+p total cross section as a function of kinetic energy of the incident pion and the π^+p mass, in the region of the 1232 MeV, $I = 3/2$ resonance. The maximum cross section, $8\pi\lambda^2$, allowed by conservation of probability is shown dashed [Perk87].

Chapter 2

Instrumentation

2.1 Overview

The EOS experiment was designed to study relativistic heavy ion reactions for beams of nuclei up to a maximum mass and energy of ^{197}Au at 1.15 MeV/n. Detectors were used to measure the charge, energy loss, and momentum of all outgoing charged particles. The experiment was performed at the Bevalac at Lawrence Berkeley Laboratory (LBL).

Figure 2.1 shows a perspective view of the overall detector set-up. The detectors used included beam counters, Plutos, TPC, MUFFINS, and TOF wall. Directly in the beam line there were several scintillation detectors: the beam counters and Plutos. These provided beam triggering and beam tracking information. The TPC itself was placed between the poles of the HISS [Enge88] magnet. This magnet provided a $13kG$

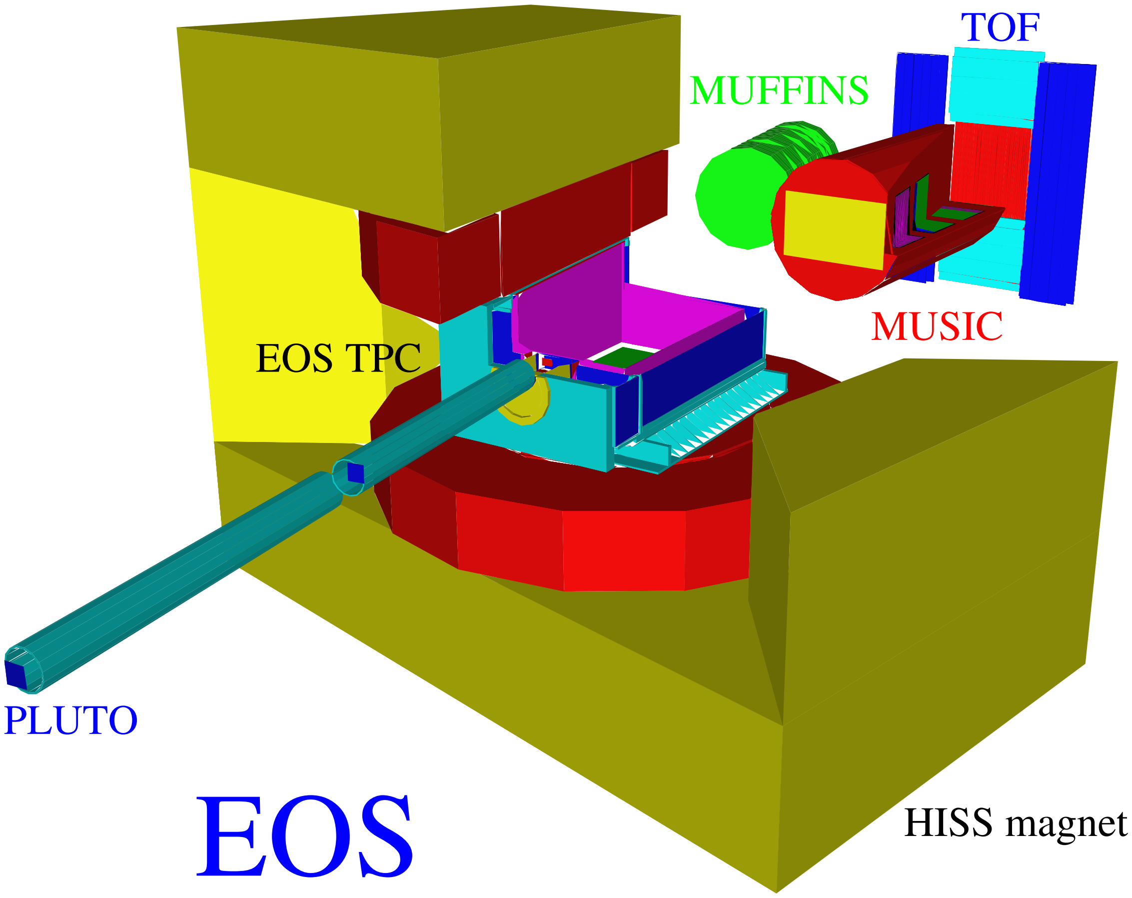

Figure 2.1: Perspective view of the EOS experimental detector set-up. The EOS TPC (shown in cut-away at the center of the HISS magnet) is the main subject of this work.

dipole field. The HISS magnet has a $2.1m$ diameter pole tip and a $1m$ gap. The TPC was able to measure tracks for particles with charge up to and including $Z = 7$. Anything larger than $Z = 7$ saturated the electronics of the TPC. Particles with $9 < Z \leq 79$ ($Z = 79$ for Au) were seen with the MUltiple Sampling Ionization Chamber (MUSIC) [Chri87]. The Time of Flight (TOF) wall was designed to determine the velocity and mass of the fastest fragments, as well as provide some redundancy with both the TPC and MUSIC. The MUFFINS [Albe92] detector was designed to detect neutrons.

2.2 The Facility

The Bevelac facility at LBL was a combination of two older accelerators. The Bevatron, built in 1954, was a weakly focusing synchrotron, designed to discover the anti-proton. The other accelerator facility was the SuperHilac, a high intensity heavy ion linear accelerator. The SuperHilac could deliver beams with energy up to $8\,MeV/n$. The two machines were combined to form the Bevalac.

2.3 The Beams

The SuperHilac injected the partially stripped Au ions into the Bevatron. The Bevatron then accelerated a particular charge state of the Au ions depending on the desired intensity and energy of the beam. Final stripping of the Au ions was

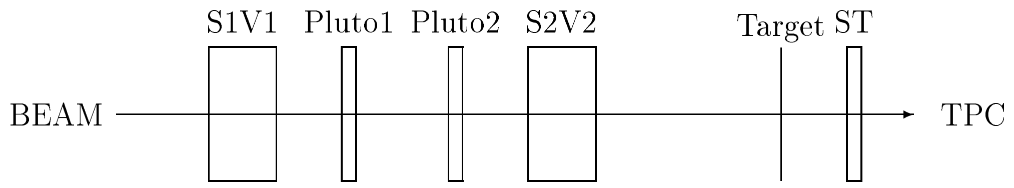

Figure 2.2: Beam Line Counters

achieved with a tantalum foil after the beam was extracted from the Bevatron. The Bevatron was a pulsed accelerator providing beam spills with times from 1 to 5 s, and a period of 8s. For the EOS experiment, the beam intensity was generally kept low, at about a thousand beam particles per second. The rate of recorded events was on the order of 30 per beam spill for the Au + Au combination. This varied somewhat with the trigger and beam energy. The data rate was predominantly limited by the tape writing speed. For central Au + Au events, there were more pad signals above the read-out threshold value, and thus more information to write to tape than for peripheral events.

2.4 Beam Line Detectors

There were four detectors in the beam line before the target. These were, in order as they appeared to the beam, S1V1, Pluto1, Pluto2, and S2V2. There was also a scintillator directly following the target, ST. The arrangement of these is shown in Figure 2.2 (not to scale).

The scintillation detectors S1V1 and S2V2 were used to define a good beam. Each of these was actually a pair of scintillators. The S1 detector, a thin scintillating sheet at 45° to the beam direction, was air coupled to two phototubes which were placed at 90° to the beam (45° to the scintillator). This arrangement provided better light collection than the typical method where the phototubes are placed on the edges of the scintillator. The signal from the west phototube ($S1_W$) was also the time zero (t_0) reference point used for the trigger. V1 is a thin scintillator with a hole in it to reject beam particles which are not in line. A hit in V1 meant a poorly collimated beam particle and was rejected. So, S1 in anti-coincidence with V1 formed part of the trigger.

The Pluto detectors were used as position detectors for the beam. The Pluto detectors were perpendicular to the beam. They each had four phototubes—one on each edge. The amplitudes of the pairs top-bottom and right-left were used to determine the y and x positions of the beam respectively. Calibration of the Pluto detectors was done with a scintillating fiber grid which consists of horizontal and vertical fibers. The horizontal and vertical fibers were viewed separately by two more phototubes. Signals from the fiber grid were correlated with the Pluto scintillator to provide a calibration of the Pluto signals. With two space points defined, one from each Pluto detector, the beam vector was defined for each event. This was necessary for determination of the reaction plane on an event-by-event basis.

The S2V2, which was identical in design and implementation to S1V1, was used as a final check for the quality of the beam. The ST detector will be discussed below.

2.5 The Trigger

There were four conditions which were met before an event was accepted and written to tape. First, as was discussed in the previous section, there must have been well defined beam particles on the target. Second, there must have been interaction in the target. Third, there can have been no additional beam particles during a sufficient amount of time for the ionization from the first event to have cleared and the TPC gas returned to normal. And finally, the computer must have been ready to receive an event.

1. Well defined beam particle

   The information from the beam counters was sufficient to determine this. Remember that V1 and V2 were scintillators with holes. B1 was defined as S1 in anti-coincidence with V1 (B1 = S1 • $\overline{\text{V1}}$). B2 was similarly defined. A coincidence B1 and B2 meant good beam particles.

2. Interaction in the target

   As mentioned, there was another thin scintillator immediately following the target. This scintillator was called the Target Scintillator (ST). The ST detector had to operate in the magnetic field. A meshdynode Hamamatsu R3432 phototube designed to work in such fields was used. Signals in a scintillator are approximately proportional to the square of the charge (Z^2) going through it. Thus, a signal from a beam particle (Z^2_{beam}) is generally larger than a signal from the fragments which would be produced in an interaction.

$$Z_{beam}^2 > Z_{f1}^2 + Z_{f2}^2 + Z_{f3}^2 + \cdots + Z_{fn}^2 \tag{2.1}$$

where $Z_{f1} + Z_{f2} + Z_{f3} + \cdots + Z_{fn} \leq Z_{beam} + Z_{target}$. Equation 2.1 of course does not always hold true, but the cases where it does not are quite rare. In a central event, the fragments are all relatively small, and the relation holds true. For peripheral events, the large target remnants usually do not have enough momentum to make it into the TPC, therefore, the relation still holds true. Thus, a simple threshold cut is sufficient; if the signal was above a certain level, it was *not* accepted as an interaction in the target.

There were some difficulties with this method. The first is simply that adding another detector put more mass in the path of the fragments. The fragments lost more energy by the time they reached the TPC. And the possibility exists, that although there was an interaction somewhere before the ST, it did not take place in the target.

At this stage, the trigger consists of coincidence in B1 and B2 and anticoincidence with the ST (B1 $\bullet$ B2 $\bullet$ $\overline{\text{ST}}$) as shown in Figure 2.3.

3. Pile-up

For an event to be acceptable, the TPC must have recovered from the previous beam particles which passed through the active volume, as well as not be seeing any signal from the next beam particles. This window of time, or "memory

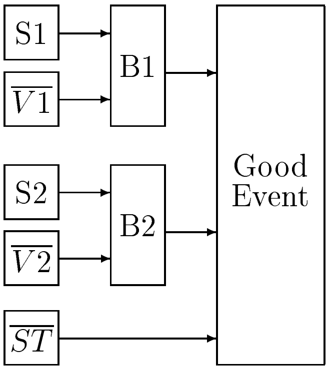

Figure 2.3: Trigger at Step 2

time," is related to the drift time of the ionization in the TPC. Any additional stuff in this window of time is called "pile-up" and will contaminate the data.

There are two kinds of pile-up to be eliminated: pre-pile-up and post-pile-up. Pre-pile-up events are those in which a non-triggering beam particle passed through the TPC prior to the trigger interaction, and insufficient time passed to allow the TPC gas to return to normal. Pre-pile-up events are eliminated in the trigger electronics by a special module called an "Up-Dating One Shot" (UDOS). This module inhibits any additional triggers for a period of $10\,\mu s$ after a beam particle signal is received in S1.

Post-pile-up events are those which have a second beam particle passing through the detection system after an interaction had been accepted by the trigger as a good event. These events are written to tape and eliminated with software cuts. Using a hardware cut would have required termination of data acquisition and resetting the electronics. The EOS collaboration made the decision to run with a low beam intensity so that post-pile-up events accounted for less than

10% of the data. A multi-hit TDC was used to record the beam signals and thus to identify these pile-up events during the data analysis.

4. Busy

   Finally, the data acquisition system must be ready. If the above triggering conditions were met, the TPC would begin transmitting data to the computer — regardless of whether the computer was ready to receive data. To avoid this, the data aquisition system generated a computer busy signal which blocked further triggers until events already waiting in the computer memory were cleared by the event builder.

2.6 The EOS TPC

The main detector used for this work is the EOS Time Projection Chamber (TPC). The TPC was designed to reconstruct a 3 dimensional picture of the track as well as energy loss information. These two things constitute sufficient information to reconstruct the momentum of the particle and its identification.

The TPC consists of a large, active drift volume, a multi-wire proportional section, and a large pad plane. The active volume of the TPC is $150cm \times 96cm \times 75cm$. There is a field cage surrounding the active area which provides the drift field. Under the drift volume is the multi-wire proportional area and below that, the pad plane. This arrangement is shown in Figure 2.4. The pad plane consists of 128 rows of 120 pads

(15360 pads) each of which is $12mm \times 8mm$.

When a charged particle enters the active volume of the TPC, it ionizes the gas. Then the ionization electrons drift down toward the anode wires in the multiwire proportional region. These electrons then undergo avalanche multiplication. It is actually the image charge induced on the pads by the positive ions after electron collection [Fern86] which is used. This allows full 3 dimensional reconstruction: 2 dimensions, x and z, from the location of the pad and the 3rd dimension, y, can be reconstructed by knowing the drift time and drift velocity for the gas.

The raw signal on the pad is then input to a charge sensitive preamp. The output signal shows the integrated charge over time. This signal is then put into a shaper which differentiates and integrates the signal to produce an output signal with a semi-gaussian shape. The amplitude of this signal as a function of time is proportional to the charge on the pad. The shaper signal is then sampled at 10 MHz ($100ns$ intervals) and the samples are stored in a Switched Capacitor Array [Klei88, Klei90]. The analog signal is read-out and digitized at 50 kHz (20 μs intervals). The SCA is a series of sample and hold circuits. The signal from each time sample is stored on a different capacitor by switches which are turned on and off in sequence. The SCA stores a signal by charging a capacitor to a potential which equals the difference between the analog input signal and a reference voltage.

Figure 2.4 shows the three sets of wire planes: the gating grid, ground plane (or Frisch grid), and anode/field wires. The ground plane and field wires are at zero potential. The anode wires are operated at 1175 volts. The anode and field wires are $2mm$ apart. The separation between the anode plane and ground plane is $4mm$, as is the separation between anode plane and pad plane. The gating grid prevents the positive ions from drifting back into the active region. The gating grid also prevents ionization electrons from unwanted events in the TPC from ever reaching the proportional region. The gating grid is closed by creating a small voltage difference between adjacent wires, $V_{gg} \pm \Delta V_{gg}$, forming a dipole plane. The field lines from the drift field are made to terminate on the gating grid plane. The offset voltage, V_{gg}, is matched to the drift field at the location of the gating grid. The gating grid must be opened, $\Delta V_{gg} = 0$, in order for the TPC to process an event.

2.7 Data Acquisition

The raw data from the TPC consists of signals from the 15360 pads. The pads were sampled over 256 time intervals of $100ns$. The signals were then digitized, and electronic pedestals were subtracted. Only signals that lasted longer than one time interval and were larger than 7 ($3 \times$ the noise) were written to tape.

Because of the large number of pads (15360), it was not cost effective to use off-the-shelf electronics. Therefore, an effort was mounted to develop a set of custom integrated circuits and electronics boards. The signal first passed through a preamp (4 per custom IC), then through a discrete component shaper amp. The signal from the shaper amp filled a Switched Capacitor Array (16 per custom IC). At the completion

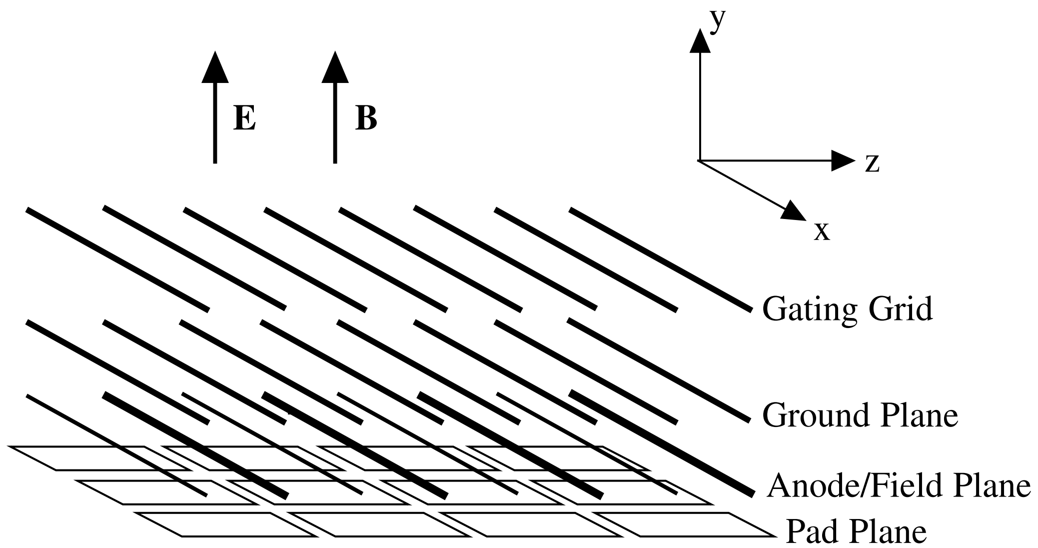

Figure 2.4: Detailed view of the wire planes located below the active gas region in the EOS TPC.

of the analog data storage for an event (all 256 time buckets of the SCA filled), the SCA were read out through a multiplexer (64 to 1) to an ADC. The digital information was sent off the board on a fiber optic link. The amplification, shaping, analog storage, multiplexing, and digitization of the signals were done in electronic hardware located directly beneath the TPC [Naka91]. In this way, the digitized signals were transmitted from the TPC via 128 fiber optical cables to the data acquisition system. (15360 cables would have been necessary with conventional electronics.)

The signals from the TPC were received over optical fiber by a VME interface and stored in a local memory. A digital signal processor applied pedestal and gain corrections to the signals before sending the information off to the taping crates [Bies91]. The data aquisition system consisted of 7 VME crates. Four of these crates were used to receive and process the data from the TPC. One VME crate was used to process the CAMAC modules from the other detectors. One VME crate was used to process the events from the receivers (the event builder). One VME crate was used to transfer the data to tape; this was called the taper. The taper crate distributed the data to a set of 3 Exabyte 8mm high density tape drives operating in parallel. Thus, since the time to write out events was the limiting factor, increasing the speed by a factor of 3 was helpful.

Chapter 3

Data Processing

3.1 Introduction

Once the raw TPC signals were recorded to tape, there were several processes which had to be performed on the data before it was ready for the final analysis and physics results. The raw signals were converted to space points, or hits; the hits were reconstructed as tracks; from the tracks, the rigidities were calculated; knowing the rigidity and energy loss allowed calculation of Particle IDentification (PID) and momentum. In addition to these steps, the detector response was studied. After all these tasks had been performed, interesting physics analysis could begin.

3.2 Space Point Reconstruction

The track spatial coordinates are reconstructed from the recorded raw TPC pad signals. In the reference frame of the TPC (which is not the same as the lab frame, or even the correct frame for physics analysis, the beam frame), the x and z coordinates are aligned with the pad plane, the y coordinate is perpendicular and points up from the pad plane: the same direction as the **E** and **B** fields. The pads are oriented in rows. The pads are $8mm \times 12mm$, so that the z coordinate follows the long direction of the pad, and can be found from the pad row of the hit, and the x coordinate of the hit can be found from the position of the hit along the row and follows the smaller dimension of the pad.

If the ionization from a track makes an avalanche whose signal is only sensed by one pad, the x, z position of the hit is taken as the center of that pad. In the case where the ionization produces a signal over two or more adjacent pads in a pad row, the signals from the pads were fit with a gaussian function, and the position is then taken as the centroid of that fit. The position resolution of the multi-pad signals is much better than the single pad signals. The multi-pad position resolution is of the order of $\sigma_{2,3p} \approx 0.7mm$ while the single pad resolution is given by the standard deviation of a uniform distribution spanning the width of one pad:

$$\sigma_{1p} = 8mm/\sqrt{12} = 2.3mm \tag{3.1}$$

The third coordinate, y, is perpendicular to the pad plane and was determined from the drift time of the ionization to the pad plane and a knowledge of the drift velocity. The signals on a pad in two or more time intervals were fit to determine the time of arrival of the signal. The width of a time bin was 100 ns. Fitting the signals in the time domain gives a timing resolution on the order of 20 ns. With a drift velocity of 5.4 $cm/\mu s$, the position resolution in the y direction is on the order of $1mm$.

Quite a few factors influence the position resolution of the TPC: transverse and longitudinal diffusion, signal-to-noise ratio in the electronics, the position of the avalanche relative to the pad, the track angle, the pad response function, energy loss fluctuations, and finally, the geometry of the wires and pads. The effect of diffusion on the drifting ionization is to broaden the track. The diffusion was measured and determined to be proportional to the square root of the drift distance. In the presence of a magnetic field, the transverse diffusion is reduced, while the longitudinal diffusion is unchanged.

This is only true for the case where the **E** and **B** fields are parallel over the entire drift distance. Although this was designed to be the case in the TPC, there were significant deviations near the edges of the HISS magnet pole tip where the **B** field is curved. The space points were corrected for the distortion in the drift path of the ionization caused by a drift velocity component perpendicular to the **E** and **B** fields. To correct for this distortion one must know the drift field, the magnetic field and the drift velocity. The magnetic field was mapped. This map has been verified by comparing the reconstructed invariant mass of $p\pi^-$ and $\pi^+\pi^-$ pairs with the known masses of the Λ and K_0^s, respectively.

The drift field was constructed to be uniform and is assumed to be so. The drift velocity was calculated by using the known distance between two laser tracks in the TPC and the measured drift time. A distortion correction table was constructed by using a transport model to simulate the propagation of the ionization through the measured fields and the TPC gas to the pad plane. The distortion correction is stored in a look-up table, and, given a measured position (x, y, z) it returns the corrected position (x', y', z') of the primary ionization.

The TPC was built so that a grid of 18 UV laser beams could be fired through the active volume. Since laser tracks are inherently straight, the signals from the laser beams provided a spatial calibration in the TPC. The position of each laser beam was nominally known to within $\pm 1mm$. Verification of the distortion table was made by applying the correction to the TPC laser tracks made in the presence of the magnetic field. The magnetic field distorted the path of the drifting ionization making the reconstructed laser track appear curved. At the end of the tracks, the distortions were up to a few mm. The distortion correction was able to remove the global distortions to better than $0.5mm$ over the length of the laser track in the TPC.

3.3 Track Reconstruction

Once the spatial coordinates had been reconstructed and corrected for distortions, one could then reconstruct the tracks of the fragments in space. The reconstruction process was complicated by the fact that there were many tracks, and many track crossings. When tracks cross, the signals from the tracks merge creating ambiguities as to which points to assign to which tracks. The track finding code uses conventional track reconstruction algorithms [Regl90] which find a segment of track and project to the next point on the track. The track reconstruction program starts from the downstream end of the TPC where the tracks are better separated. The program first finds a "spore" of 3 space points in a straight line on three adjacent pad rows. A straight line projection is made to find the next two points. If five points are found, a helical fit is made and used to project to the next point. As subsequent points are found, the track is continually refit. The track reconstruction uses a progressive fitting method in that information from the track is used as it is found to predict the position of the next point on the track. Once the track finding has been completed, the vertex of the event can be found as the point of closest approach of all of the tracks. The found tracks that come within $2.5cm$ of the event vertex are then refit using the event vertex as a point on the track. The majority of the tracks come within $2.5cm$ of the target. The distribution of the Distance of Closest Approach, DCA, is shown here in Figure 3.1.

Once the tracks have been reconstructed, the program uses the curvature to return

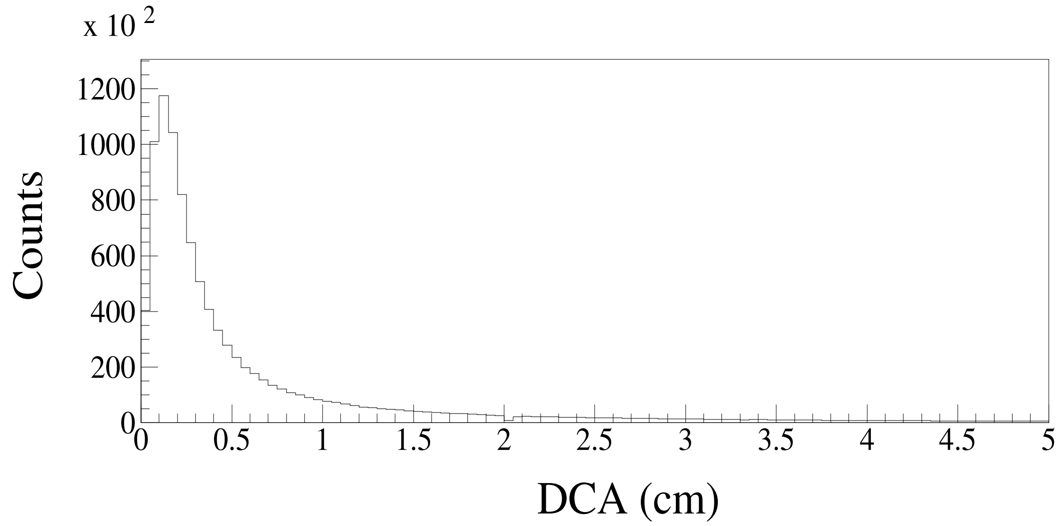

Figure 3.1: Distance of Closest Approach (DCA) of all particles. All the tracks within 2.5 cm of the vertex are refit with the vertex as a point on track

the x, y, and z components of rigidity at the target and several other points, such as the beginning and end of the TPC. The program also returns an average value of the kinetic energy loss along the track. The program does not take into account this energy loss as it fits the tracks. This is acceptable since the energy loss is small. It is worth noting, however, that the fitting algorithm does use the correct magnetic field from the map as discussed in the last section.

The kinetic energy loss was reconstructed from the size of the signals induced on the pads. However, the energy lost per pad row by an ionizing particle in traversing the TPC gas volume has large statistical fluctuations, called Landau fluctuations, which are due to delta rays. Because of this, the energy loss samples from the pad signals of a track were truncated to the lower 70% of the distribution. The truncated energy loss distributions are then approximately Gaussian. The combination of the trucated mean energy loss and rigidity is used in particle identification [Alli80].

3.4 dE/dx Resolution and Particle Identification

The Bethe-Block energy loss formula for ionizing particles shows that energy loss is proportional to $Z^2/m\beta^2$ for fragments with $p/A < 3\,GeV/c$. Plotting energy loss against rigidity shows a distinct band structure where the bands are related to the charge and mass of the fragments. The log(mean energy loss) vs. rigidity is shown in Figure 3.2 for 1.15 GeV/n Au + Au. For the lighter fragments ($Z < 3$), the bands correspond to different charge and mass states. For the heavier fragments, different charge states can be discerned. The resolution is insufficient to distinguish the isotope bands for the heavier fragments and the lighter fragments at high rigidities.

The dE/dx resolution for a track with 110 samples is $\approx 5\%$ after correction for all systematic biases [Scot93]. This is in approximate agreement with the theoretical prediction of Allison and Cobb [Alli80] for the conditions encountered in the EOS TPC. The resolution is sufficient to clearly identify the light fragments: $\pi^{\pm}$, protons, deuterons, tritons, ^3He, alphas, and the charges of the $Z = 3, 4, 5, 6$ fragments.

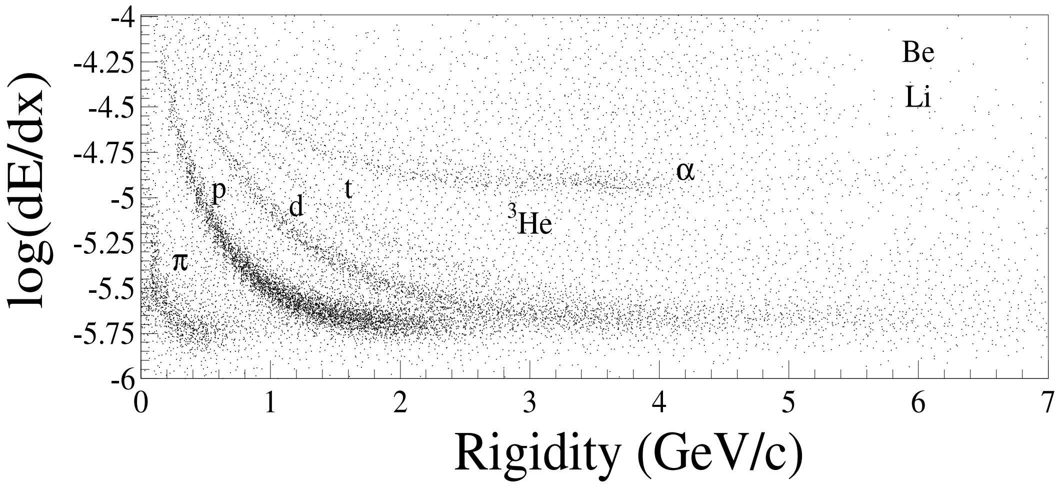

Figure 3.2: Energy loss as a function of rigidity. The bands indicate particle identification as labeled.

3.5 Momentum Resolution

The total momentum resolution depends on the momentum, velocity, and spatial resolution of the detector. The momentum resolution in the horizontal plane perpendicular to the magnetic field for a particle of momentum (p) and charge (Z) is given by [Part90]

$$\frac{\sigma(p_p)}{p_p} = \left[\left(\frac{\sigma_x p_p}{0.3BZ(Lcos\lambda)^2}\sqrt{\frac{720}{N+5}}\right)^2 + \left(\frac{0.016Z}{\beta p_p Lcos\lambda}\sqrt{\frac{L}{X_0}}\right)^2\right]^{\frac{1}{2}} \tag{3.2}$$

where p_p is the momentum of the fragment perpendicular to the magnetic field:

$$p_p = \sqrt{p_x^2 + p_z^2} \tag{3.3}$$

B is in Tesla, lengths are in meters, and momenta in GeV/c. L is track length, λ is dip angle, β is velocity, N is the number of measured points along the track, and X_0 is the radiation length in the TPC gas. The first term in Equation 3.2 is the measurement error and the second term is the error due to multiple scattering. The momentum resolution for the EOS TPC is better than 1% for $p_p < 2\,GeV/c$ and better than 2% for $2\,GeV/c < p_p < 3\,GeV/c$.

3.6 Calibration of the Target Position

The position of the target must be known in order to determine the rigidity at the target, as well as to throw away events which did not originate in the target. The target position is approximately known from physical measurements of the target relative to the TPC. However, the target position can be calibrated from the data by reconstructing the event vertex. The z coordinate of the vertex obtained by this method is shown in Figure 3.3. The contribution from the target is seen at about $-91cm$, the target scintillator (ST) at $-87.5cm$, and if one were to expand the picture, the beam pipe window would be visible as a peak at $-135cm$. Reconstruction of the event vertex allows elimination of non-target events and determination of the target position with a resolution of $\sigma_{vertex} \approx 2mm$.

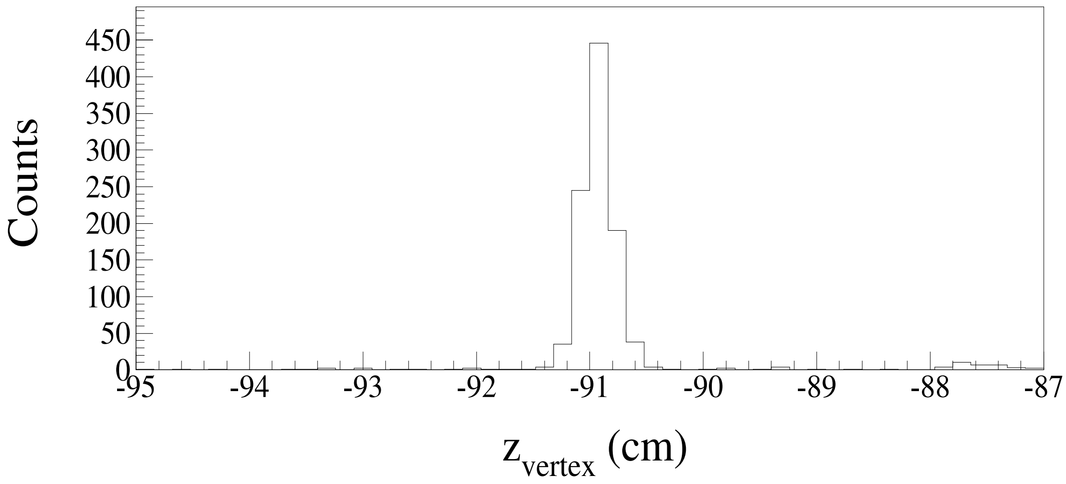

Figure 3.3: z coordinate of the vertex position in cm as reconstructed by the tracking program.

3.7 Calibration of the Orientation of the TPC

As mentioned briefly, the reference frame of the TPC was not the same as the lab or beam frame. The beam entered the TPC at an angle. With the magnetic field turned off, this angle was approximately 7.5° horizontally and 0.5° vertically. Due to bending in the magnetic field and depending on beam energy, the horizontal angle was less than 7.5°. For 1.15 GeV/n Au + Au, the horizontal angle has a mean of 5.32° and the vertical 0.36° as seen in Figure 3.4.

The angle of the beam incident on the target was determined by the upstream Pluto detectors. The two Pluto detectors gave two space points which determined the incident beam vector. This vector was then propagated through the magnetic field until it reached the target. Shown in Figure 3.4 are the angles returned by the Pluto Decode Algorithm. Low gain data was used to track the beam itself through the TPC. The angles obtained in this manner were compared with the Pluto angles. The agreement was quite good. Another check was performed as well. The Plutos track the beam to the target, and the position agreed with TPC tracking as discussed in the last section with a mean difference of the TPC-Pluto vertex position of $1mm$ with $\sigma = 3mm$.

The Pluto information is needed because it can be determined on an event-by-event basis. This is valuable information because even small changes in incident beam angle have a noticable effect on the reaction plane determination.

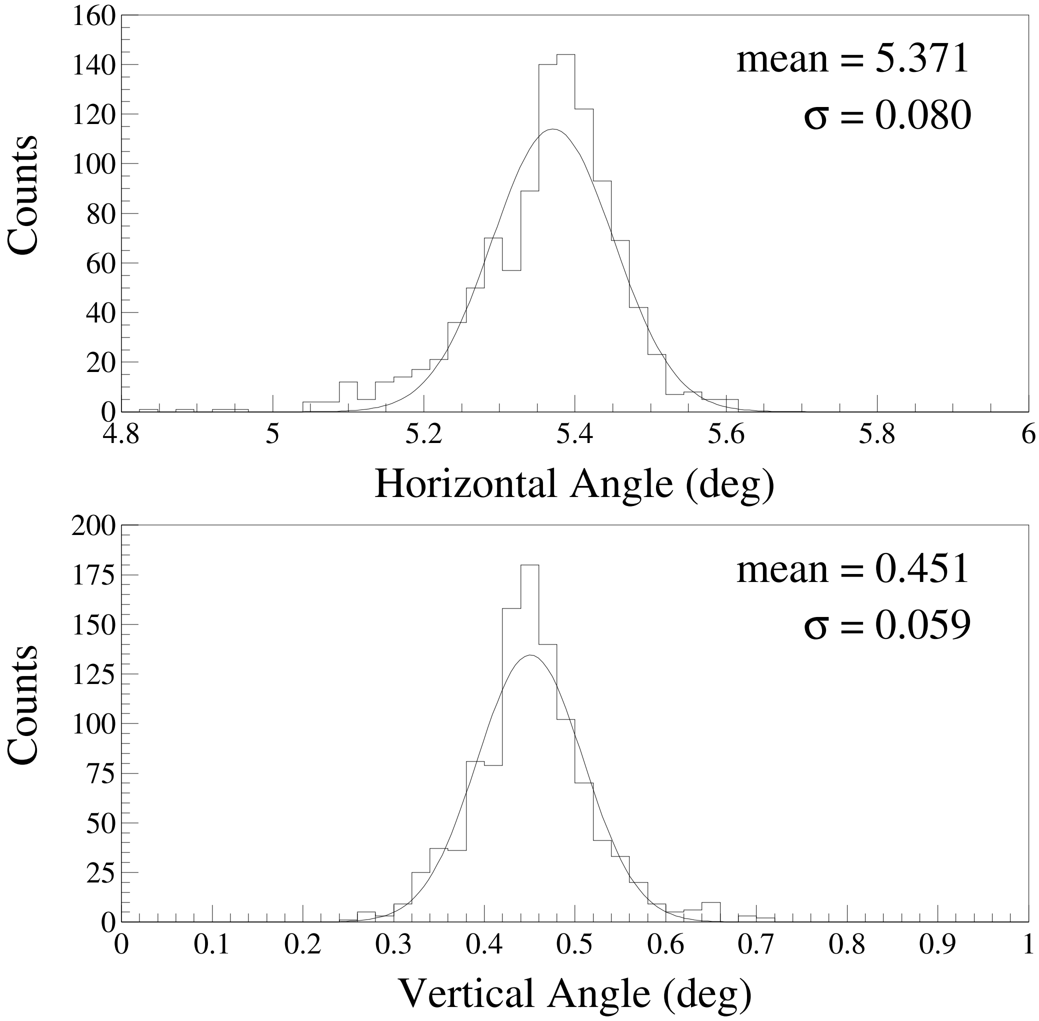

Figure 3.4: Horizontal and vertical angles of the beam incident on the target. These angles were calculated from the 2 positions in the Pluto detectors and then projected through the magnetic field to the target.

Chapter 4

The TPC Acceptance

4.1 Introduction

In order to interpret the results produced by the EOS TPC, one must have a good understanding of the biases introduced by the detector. The ideal detector would find, identify, and measure the momentum of every particle emitted from the reaction. However, the performance of a real detector is limited by geometric acceptance, neutral particle insensitivity, tracking inefficiencies, misidentifications, measurement inaccuracies, and errors.

In this chapter, it will be described in detail how one can use simulations and the data to understand acceptance effects. The simulations involve putting known theoretically generated events through a software model of the TPC and analyzing the results as if they were real data. This method has some limitations, and it will also be necessary to use knowledge of symmetries which must exist in the real data. For example, conservation of momentum tells one that in the center-of-momentum system, total forward going momentum must equal total backward going momentum. If this is not the case, some tracks were missed or momenta were calculated incorrectly.

4.2 Simulations

To understand the acceptance and efficiencies of the detector, it was necessary to simulate the detector response. The simulation used a generated event and produced a simulated detector response for that event. The simulation used the GEANT [Brun91] program to propagate the fragments through the TPC. The GEANT program generates space points along a track of a fragment and dE/dx information at each space point. The space points are then jittered within an estimated resolution and subsequently merged if two or more space points are within a specified distance.

We have used the simulation to study detector acceptance and efficiencies. Shown in the Figure 4.1 is the percentage of tracks in the generated event which would have been found by the TPC as a function of normalized rapidity. Rapidity is defined in Equation 4.1:

$$Y = \frac{1}{2} \log \left(\frac{E + p_z}{E - p_z} \right) \tag{4.1}$$

The choice to study efficiency as a function of rapidity was dictated by the data analysis methods and convenience. Rapidity is Lorentz invariant, which makes it simple to use: a straightforward addition is all that is needed to shift rapidity from the lab to center-of-mass frame. As will become clear in Chapters 5 and 6, flow and squeeze-out have been studied as functions of rapidity.

Normalized rapidity denotes scaling the rapidity values by the beam rapidity. Thus, in units of normalized rapidity, fragments with $Y_{cm}/Y_{beam} = 1$ are emitted with beam rapidity along the beam axis, $Y_{cm}/Y_{beam} = -1$ indicates target rapidity, and $Y_{cm}/Y_{beam} = 0$ indicates fragments that are emitted perpendicular to the beam axis with center-of-mass rapidity.

For protons with rapidities from -0.3 to 0.5, we have better than 90% acceptance. Figure 4.2 shows a similar plot for π^+ and Figure 4.3 shows the plot for π^-. The pions have a very different acceptance from the protons; occasionally one even finds more tracks for the pions than were present in the generated event.

To study flow and squeeze-out, it was necessary to understand acceptance effects in more detail. Shown in Figure 4.4 is p_y vs p_x for protons as reconstructed from a simulated event. The specific case shown here is for impact parameter 4 *Fm*. With the exception of the first panel, the response looks fairly uniform with maybe a slight shift off-center. This is due to beam angles—there is no Pluto information for the simulated events.

The significant result is the difference between the simulation and the experimental data. The data show more dramatic acceptance problems than do the simulations. Shown in Figure 4.5 is p_y vs p_x for protons from the data using the same impact

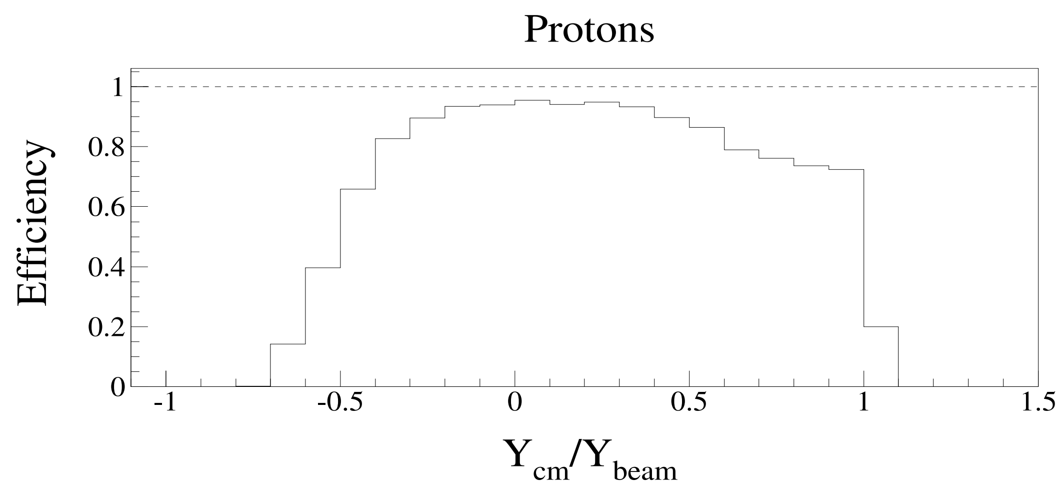

Figure 4.1: Tracking efficiency as a function of normalized center-of-mass rapidity for protons from 1.15 GeV/n Au + Au. The tracking efficiency is better than 95% for the region from -0.2 to 0.3 in rapidity.

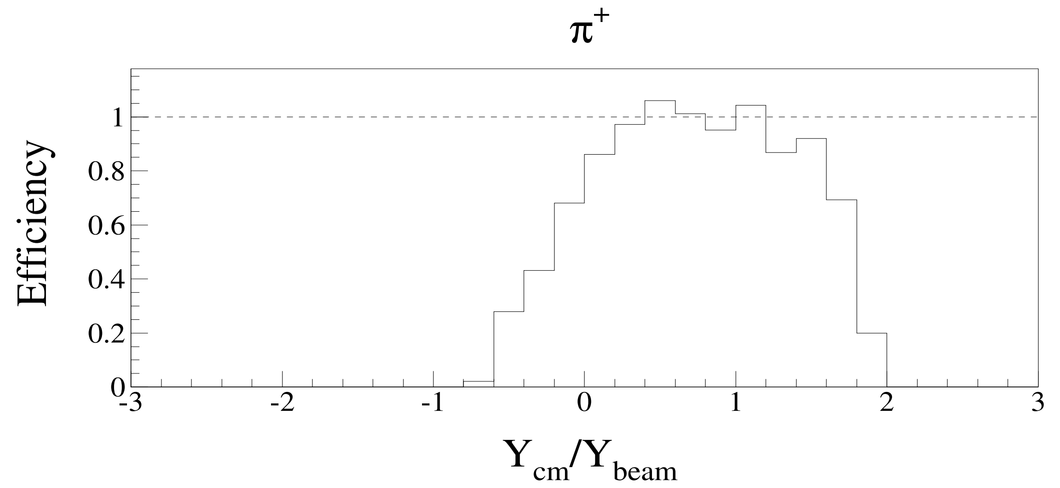

Figure 4.2: Tracking efficiency as a function of normalized center-of-mass rapidity for π^+ from 1.15 GeV/n Au + Au. The tracking efficiency is more difficult to understand than for the protons. The area of efficiency > 1 is probably due to broken tracks.

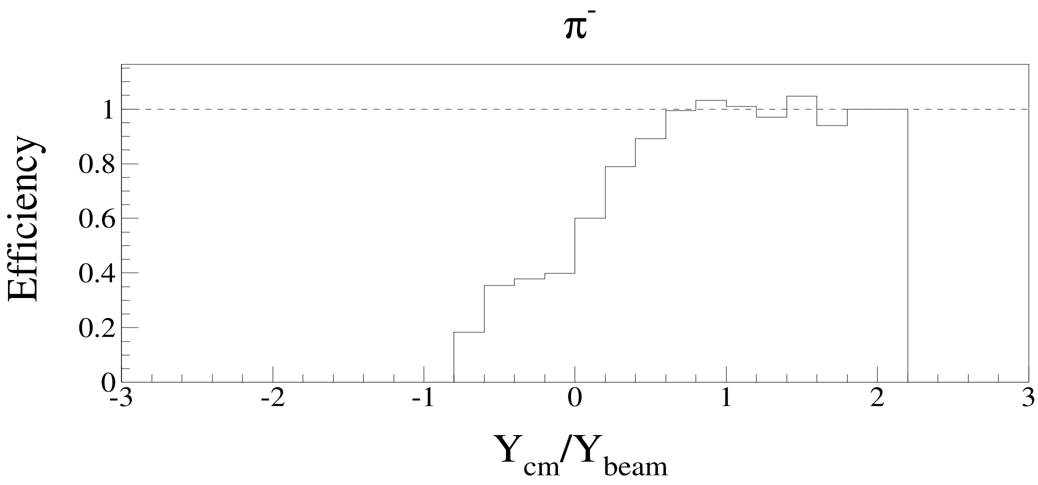

Figure 4.3: Tracking efficiency as a function of normalized center-of-mass rapidity for π^- from 1.15 GeV/n Au + Au.

parameter as shown in the Figure 4.4 for the simulations. There are holes, left-right asymmetry for several of the more forward going cases, and a lack of symmetry about $Y_{cm}/Y_{beam} = 0$. The acceptance holes are due to the beam going through the center of the TPC and saturating a large slice of the gas. When the protons go through this area, they cannot be seen by the TPC.

These asymmetries were studied to see what effect they had on the analysis. The method chosen involved symmetrizing the data and calculating efficiency tables. Comparing the forward going particles to the backward going in the center of mass reveals a problem. The bin of Y_{cm}/Y_{beam} from 0 to 0.25 should look exactly the same as the bin from -0.25 to 0. Also, each plot should be azimuthally symmetric. That is, each shade of gray should be a circle. This information can be used to determine

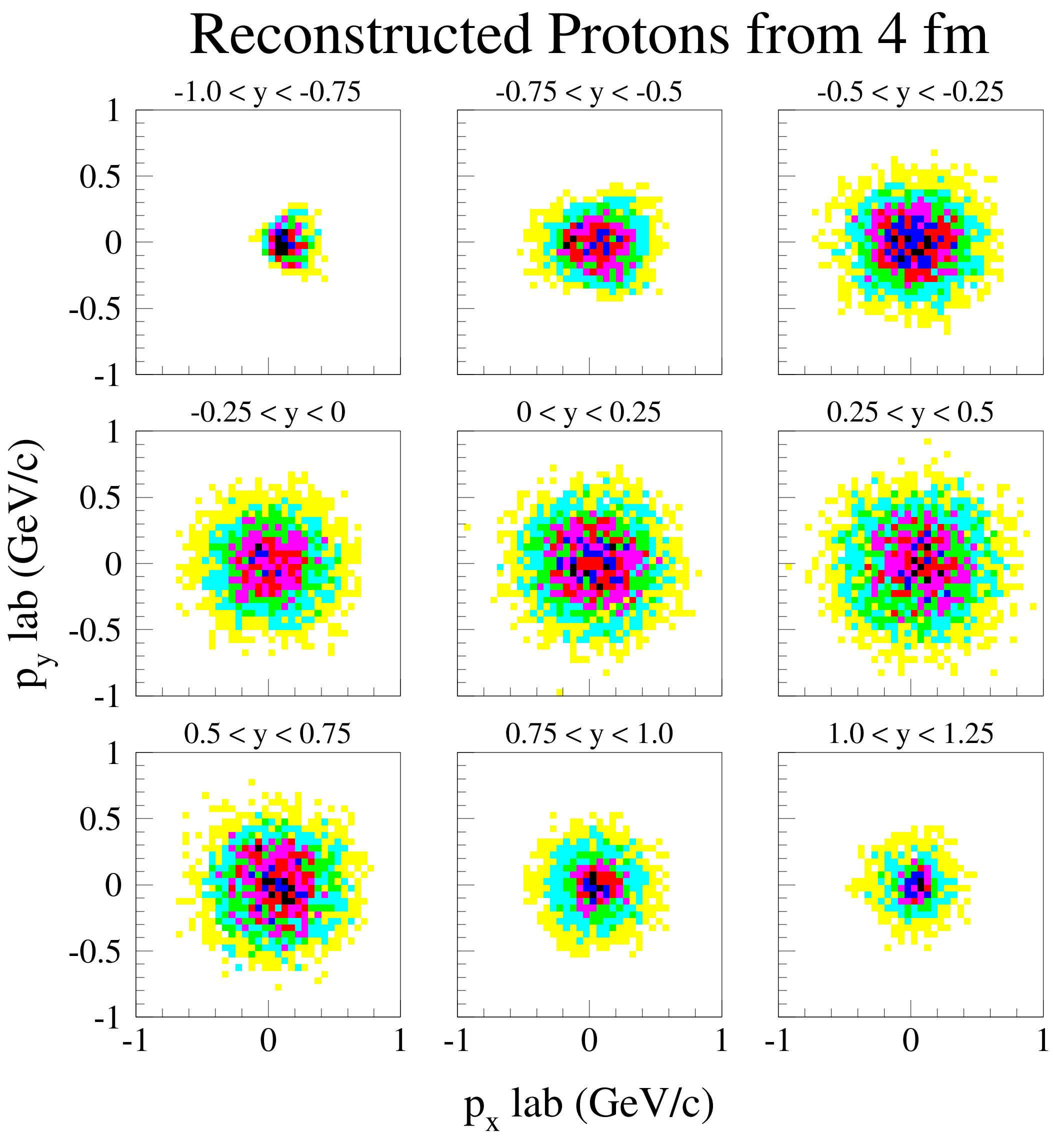

Figure 4.4: p_y vs p_x for reconstructed protons in increasing rapidity bin. Although not perfect, there are no large acceptance problems seen here.

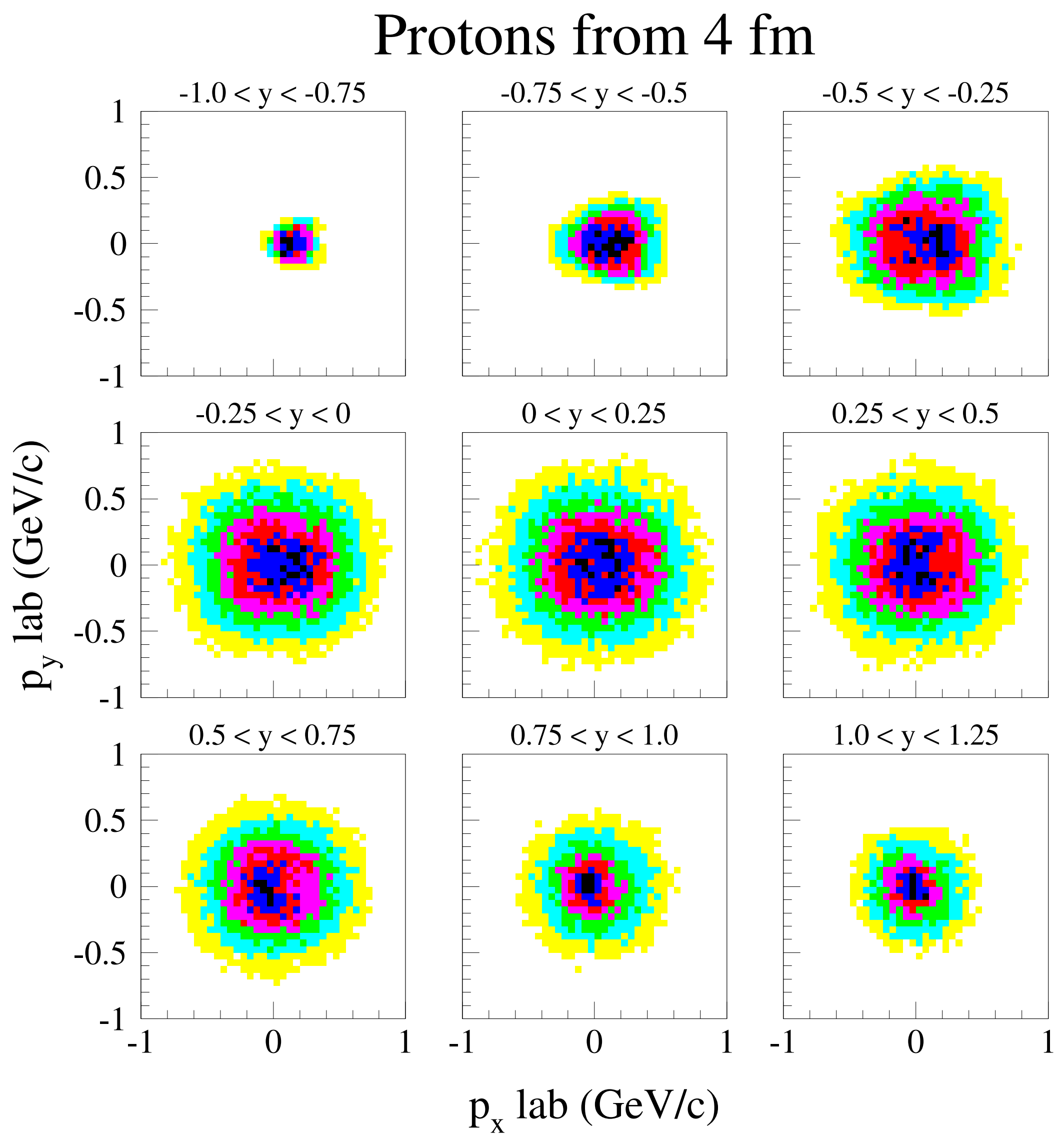

Figure 4.5: p_y vs p_x for protons from 1.15 GeV/n Au + Au in increasing rapidity bins. Here one can see the holes beginning to take shape. In the sixth panel, for $0.25 < y < 0.5$, a clear left right asymmetry is visible. It continues through the ninth panel.

the maximum for a given p_x, p_y, and efficiencies can be calculated. This allows the model calculations to use a look-up table to ascertain the probability that for a given p_x, p_y the TPC would not see the track. In this way, the acceptance holes were added to events generated by the theoretical model.

Chapter 5

Data Analysis

5.1 Overview

There were several analysis steps before the final results were obtained. First, the reaction plane is established for each event. There is a multiplicity dependence to the determination of the reaction plane which must be understood. Next, the flow tensor is calculated. Then, the momentum with respect to the reaction plane can be determined. Finally, S-curves and ϕ distributions are plotted and fit parameters are extracted.

All of the work presented here has been performed on approximately 100,000 good events from 1.15 GeV/n Au + Au unless specifically stated otherwise. The criteria for selecting good events is as discussed in previous chapters, including all cuts such as software pile-up elimination.

5.2 The Reaction Plane Determination

The reaction plane for this work is determined by a modified Danielewicz and Odyniec method [Dani85]. Their method involves summing the transverse momenta of all charged fragments, applying a weighting factor as a function of rapidity, and subtracting the backward going momenta from the forward going. A vector which is by definition in the reaction plane ($\boldsymbol{Q}$), is defined:

$$\boldsymbol{Q} = \sum_{i=1}^{n} w(y_i)\boldsymbol{p}_{i\perp} \tag{5.1}$$

where $\boldsymbol{p}_{i\perp}$ is the momentum transverse to the beam direction. In this method, the weighting factor ($w(y_i)$) is -1 for backward going particles and +1 for the most forward going particles and varies linearly between as shown by the dashed line in Figure 5.1. This removes the fragments near the midrapidity region from being counted heavily in the reaction plane determination. For the analysis discussed here, only forward going baryons were used to determine the Q-vector. The weighting factor actually used is shown by the heavy solid line in Figure 5.1.

In this way, the direction of the weighted transverse momentum is found for each event. The Q-vector is one vector which defines the reaction plane. The other vector which by definition must be in the reaction plane is the incident beam vector. The beam direction is known from the Plutos as discussed in Chapter 3.

There is a simple test of this method. For a large number of events, one plots the distribution of azimuthal angles of the reaction plane (ϕ_{RP}). For many events, the

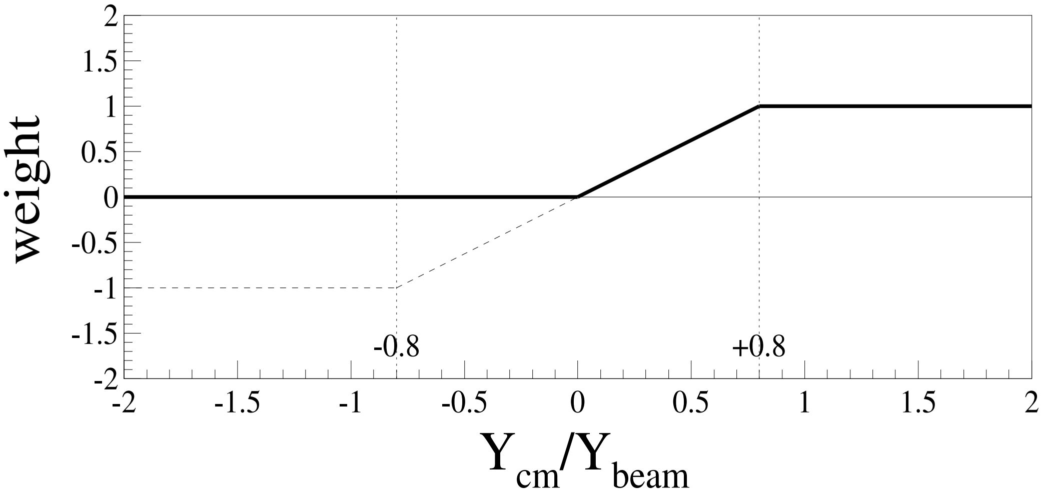

Figure 5.1: Weighting factor as a function of normalized center-of-mass rapidity.

distribution should be flat. This is shown in Figure 5.2, and the agreement with a horizontal line fit is quite good: $\chi^2 = 0.98$.

Another check for how well the Danielewicz and Odyniec method works, the sub-event method, is described by Danielewicz [Dani85]. In this method, the outgoing fragments are randomly assigned to one of two groups. The azimuthal angle of the reaction plane is calculated for both subgroups, and they are compared. Shown in Figure 5.3 is the difference between the ϕ angle of the two Q-vectors. The dispersion has $\sigma = 30°$. This is the uncertainty in the reaction plane measurement.

Each event can be rotated to a new frame such that the Q-vector lies along the x-axis, and the squeeze-out and flow analyses can be performed. There is an additional

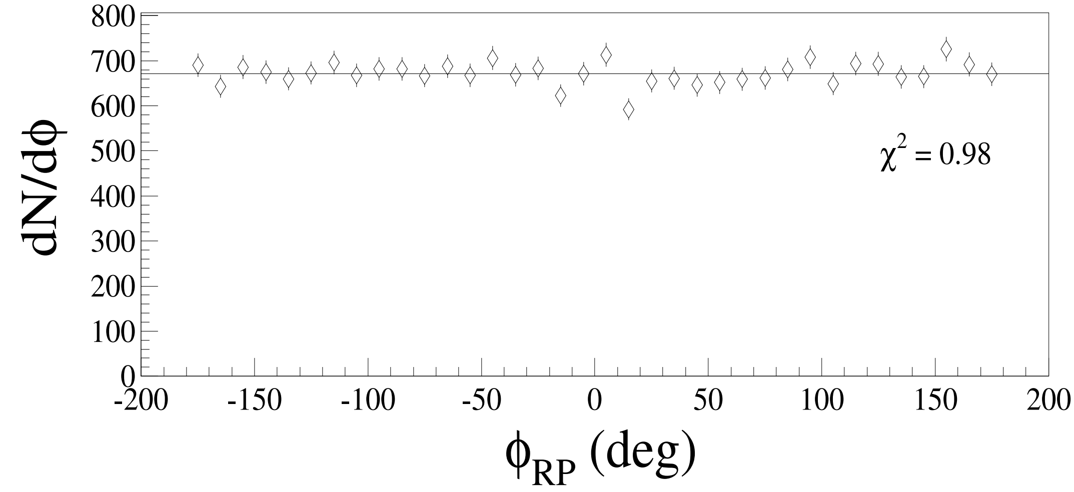

Figure 5.2: Azimuthal angle of reaction plane, ϕ_{RP}. The distribution is quite flat, the $\chi^2 = 0.98$ shows a good agreement with the straight line fit.

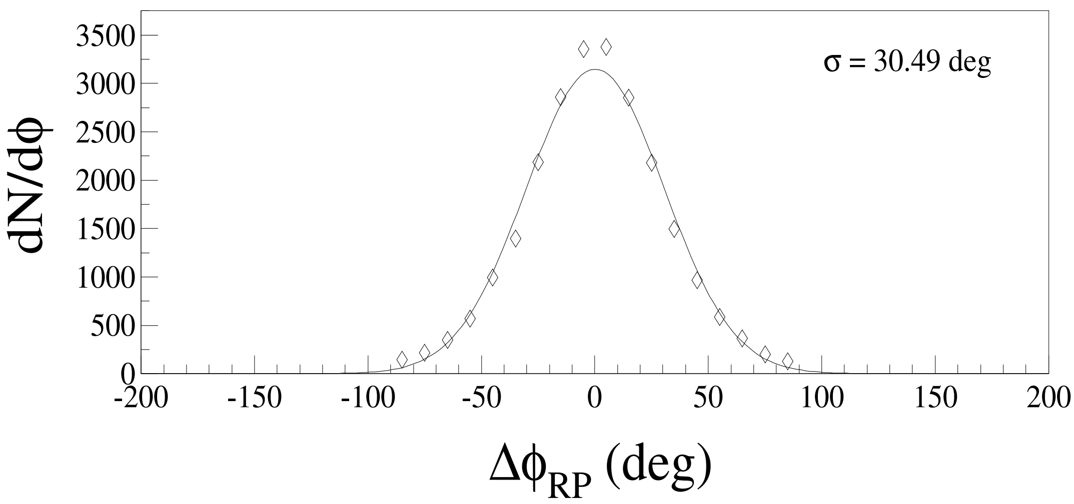

Figure 5.3: Difference inϕ_{RP} for two randomly created subgroups: $\sigma \sim 30°$.

Multiplicity	$0-30$	$30-60$	$60-90$	$90-120$	>120
$\langle\cos\Delta\phi_{RP}\rangle$	0.895	0.935	0.911	0.797	0.703

Table 5.1: Correction factors applied on average to the transverse momentum in the rotated frame. The average p_x in the rotated frame is divided by one of these factors as a function of multiplicity.

correction which can be applied on average after this rotation. The dispersion in the reaction plane measurement was shown by the sub-event method in Figure 5.3. The author [Dani85] goes on to say that the momentum components can be corrected on average:

$$\langle p_x\rangle = \frac{\langle p'_x\rangle}{\langle\cos\Delta\phi_{RP}\rangle} \tag{5.2}$$

where $\langle p'_x\rangle$ is the average x-component of the momentum in the newly rotated frame, and $\langle p_x\rangle$ is the corrected momentum in the same frame. This correction is important for the flow analysis. For the data shown in this thesis, the correction was done as a function of multiplicity, for reasons which will become obvious. Shown in Table 5.1 are the exact values of $\langle\cos\Delta\phi_{RP}\rangle$ which were used to correct the data for the flow analysis.

It was observed that there is a strong impact parameter dependence on the flatness of the ϕ_{RP} distribution. This uncorrected dependence is shown in Figure 5.4. The lowest multiplicity region is shown in the top left. It is clearly not flat, although the statistics are poor. The most central, or highest multiplicity bin was the big surprise. The large hole was probably cancelled out by the peak in the second panel. The mid-multiplicity region is approximately flat. Thus, adding everything together showed

Multiplicity	$0-30$	$30-60$	$60-90$	$90-120$	> 120
Horizontal Angle (deg)	4.96	5.04	4.90	4.63	3.97
Vertical Angle (deg)	0.01	0.23	-0.05	-0.32	-0.32

Table 5.2: Angles used to correct the beam direction used in the reaction plane determination. Recall the measured Pluto angles from Figure 3.4 of 5.32° and 0.36°.

the flat distribution as seen in Figure 5.2.

There is no physical reason why the reaction plane should not be uniformly distributed over ϕ. Therefore, additive corrections were applied to the incident beam angle as a function of multiplicity. The corrected angles are given in Table 5.2. This correction compensates for variations in the detector acceptances as a function of multiplicity. In this fashion, the ϕ_{RP} distributions were flattened for 5 multiplicity bins. The results of this correction are shown in Figure 5.5.

Once the reaction plane was known for each event, that event was rotated so that $\phi_{RP} = 0$ described the x-z plane. The choice is arbitrary; it is convenient to choose the lab frame. Once this is done, all the events have the same reaction plane, and many events can be averaged and global event characteristics studied. In this way, out-of-plane emission can be studied, and the momenta can be projected to the reaction plane to measure flow.

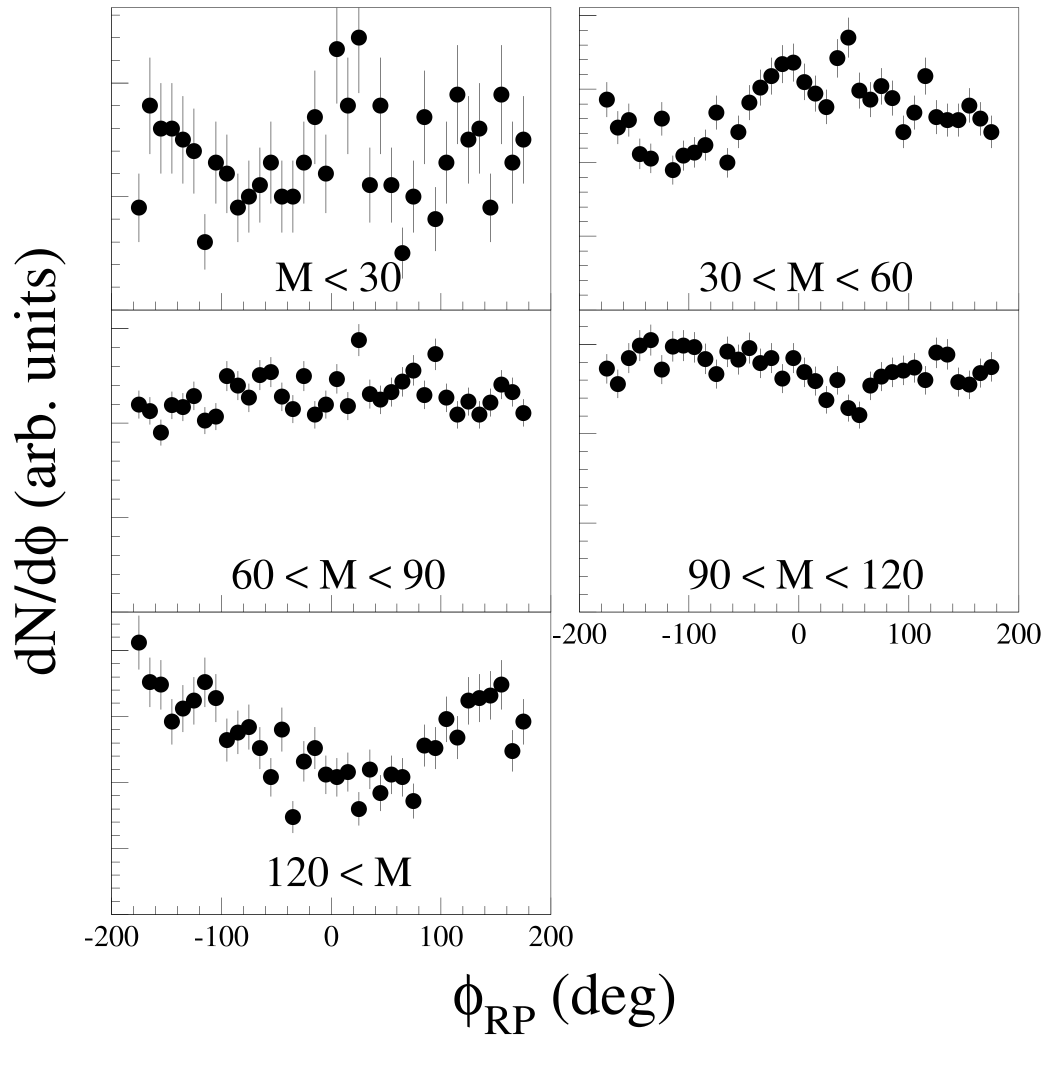

Figure 5.4: Each panel shows different multiplicity cuts on the azimuthal angle spectra. The vertical scale is linear and starts at zero. The top left panel shows the most peripheral region, and the bottom panel shows the most central region. Only the midrapidity region is flat. This indicates that the low and high multiplicity events combined to look flat. In reality there is a dramatic dependence on multiplicity.

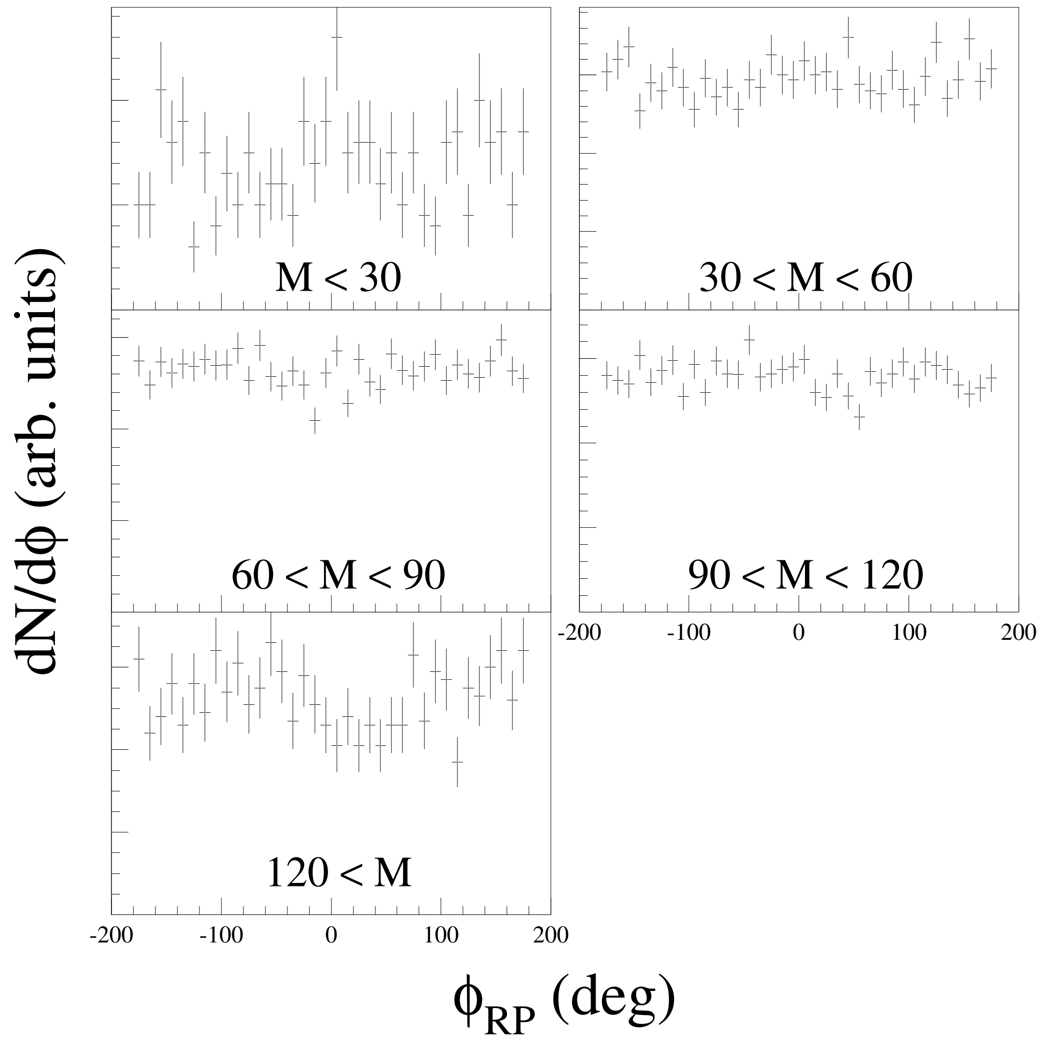

Figure 5.5: The top left panel shows the most peripheral region and the bottom panel shows the most central region. The vertical scale is linear and starts at zero. After correcting the angles, there is a clear improvement for the first 4 panels, and although the fifth, most central bin is improved, it is still not quite flat.

5.3 The Flow Tensor

The event shape analysis used here is based on the sphericity tensor commonly used in high energy physics [Bran79, Wu79]:

$$F_{ij} = \sum_{n=1}^{M} \frac{P_i^n P_j^n}{2m_n} \tag{5.3}$$

where P_i^n denotes the i^{th} momentum component of the n^{th} fragment, m_n is the rest mass of the n^{th} fragment, and M corresponds to the multiplicity of the event. The weighting function of $1/2m_n$ is applied to the kinetic flow tensor to treat composite particles in a coalescence invariant way [Gyul82], such that the large fragments are not weighted too heavily.

The flow tensor approximates the event as an ellipsoid in momentum space. The orientation angles and aspect ratios of the event ellipsoid are obtained by diagonalizing the kinetic flow tensor. The distribution of flow angles ($dN/d\theta$) is biased by a Jacobian factor [Dani83] which may be approximately removed by dividing the distribution by that Jacobian, $\sin\theta$. Historically, the measurement of the flow angles [Gust84, Stoc86] was a first indication of directed collective flow. In Figure 5.6, the distributions of the flow angles are shown for each multiplicity bin used in this study of 1.15 GeV/n Au + Au. To see the form as a function of multiplicity, the flow angles were studied in more detail and the mean value of θ_f was extracted and plotted as a function of multiplicity. This is shown in Figure 5.7.

Danielewicz and Gyulassy [Dani83] have shown that measures such as θ_f and the

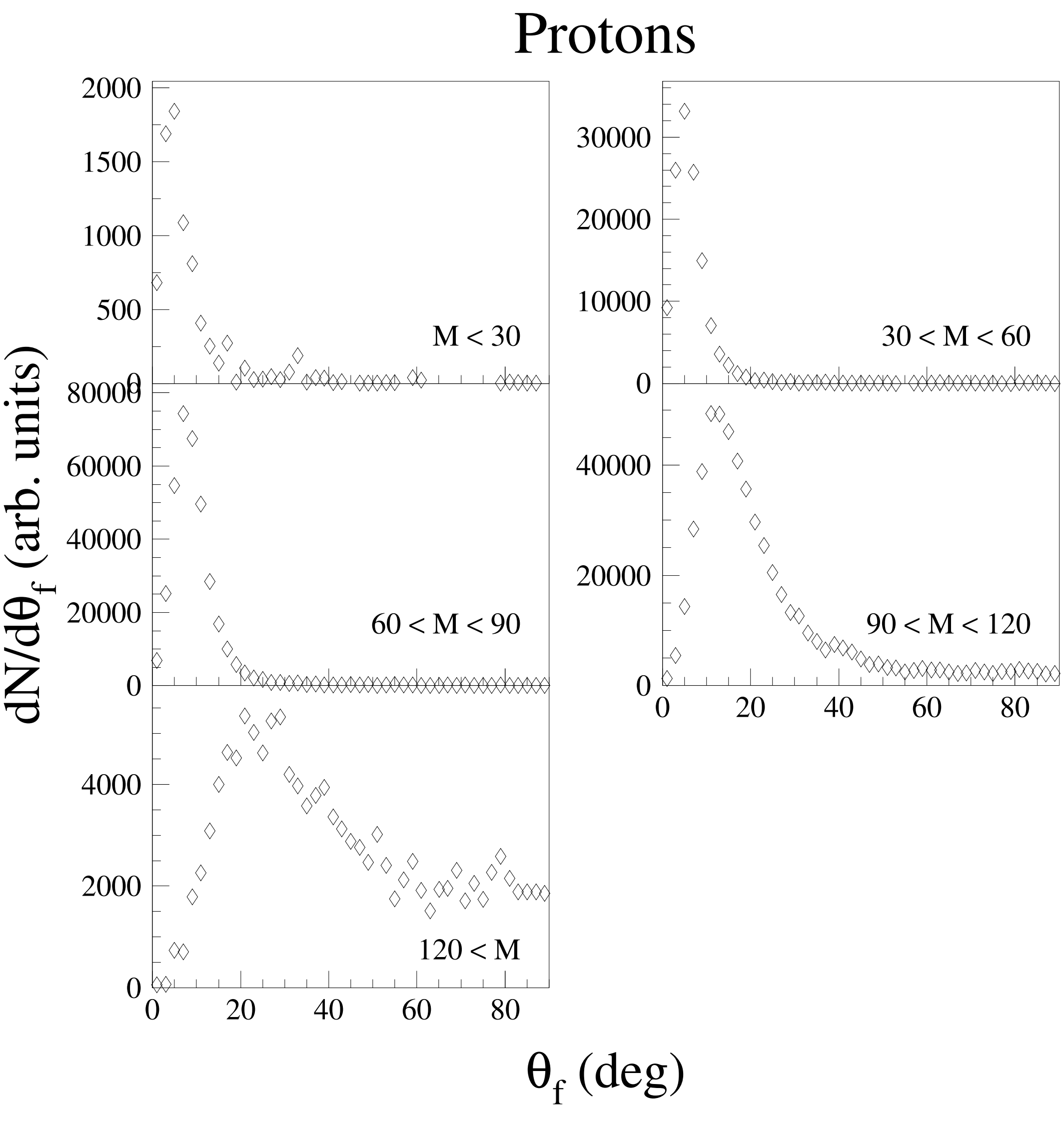

Figure 5.6: An early method of measuring flow involved measuring the angle of the flow axis by diagonalizing the flow tensor. The results shown here are for protons from 1.15 GeV/n Au + Au. A clear increase is seen as a function of multiplicity with the more central events showing higher flow angles.

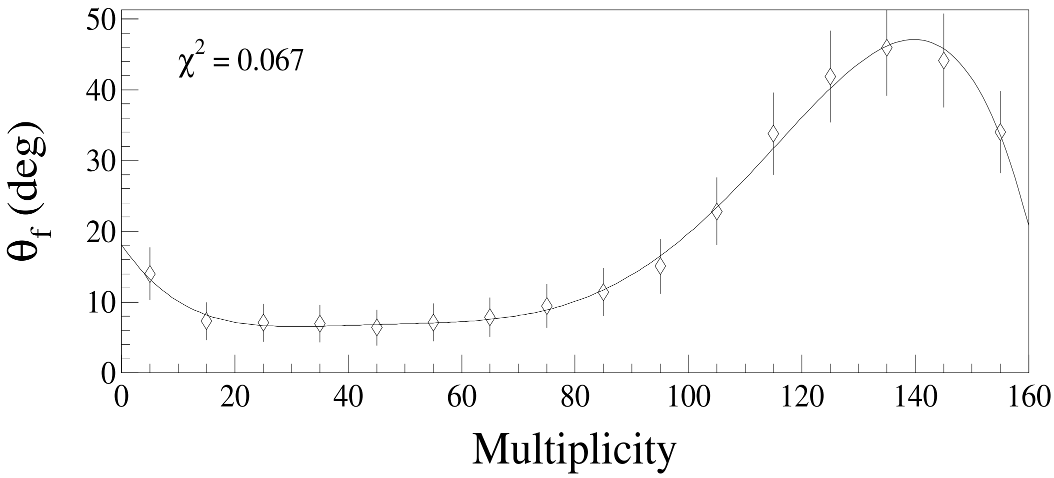

Figure 5.7: The mean flow angle as a function of multiplicity.

aspect ratios are heavily influenced by finite number distortions. They have suggested the only true signature of flow is a clear peak in the $dN/d\theta_f$ distribution away from $\theta_f = 0$.

Danielewicz and Odyniec [Dani85] developed the global transverse momentum method to demonstrate collective motion in events where the sphericity method was inconclusive because of statistical fluctuations and the contributions from the spectators. Their transverse momentum method uses a weighting factor which de-emphasizes midrapidity fragments and therefore reduces fluctuations around the reaction plane.

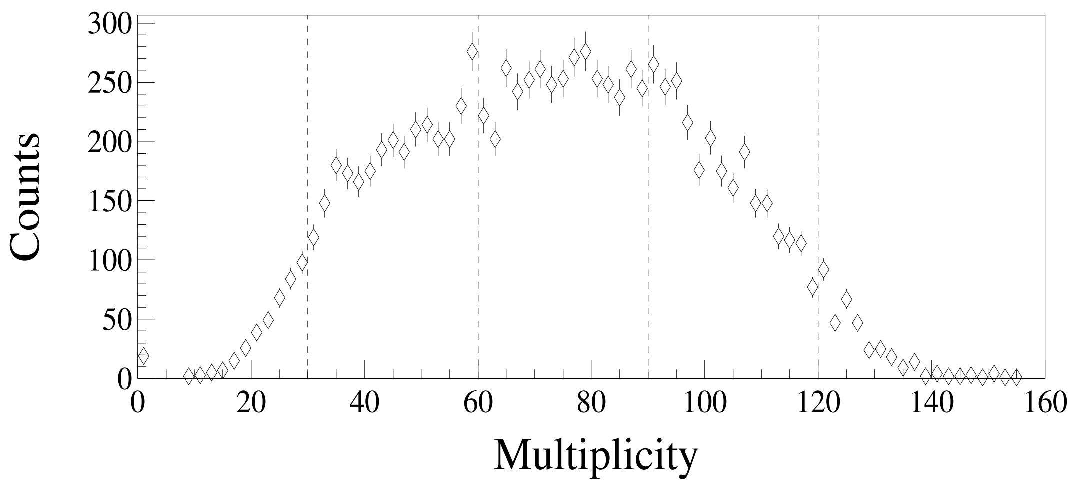

Figure 5.8: The experimental multiplicity distribution for $1.15\, GeV/n$ Au + Au. The dotted lines show the multiplicity bins which are then used to compare to impact parameter.

5.4 Impact Parameter Determination

Since it is of interest to study flow and squeeze-out as a function of impact parameter, the relationship between multiplicity and impact parameter must be discussed. The experimental multiplicity distribution is shown in Figure 5.8 with the divisions between multiplicity bins shown by dotted lines. These bins are used for future impact parameter comparisons. There are five multiplicity bins, and data will be shown for five impact parameters.

A very simple overlap method was used to compare multiplicity to impact parameter. The nuclei were assumed to be spheres with a uniform density of nucleons. The

Multiplicity	$0-30$	$30-60$	$60-90$	$90-120$	>120
b range Fm	11 - 9	9 - 7	7 - 5	5 - 3	3 - 0

Table 5.3: Multiplicity and corresponding value of the impact parameter. This simple calculation is justified since the bins of 2 Fm are quite large.

geometric overlap region was calculated numerically for different impact parameters, and the number of nucleons in the overlap region was calculated. This number of nucleons was scaled by Z/A as an estimate of the charge multiplicity of an event. The results of this calculation are shown in Figure 5.9. The lines are drawn at the impact parameters to be quoted in the rest of this thesis. They show the multiplicity on the y-axis corresponding to the impact parameter on the x-axis. Each multiplicity marked by one of those lines is nearly in the center of a multiplicity bin as shown in Figure 5.8.

Shown in Table 5.3 is the exact relation used between the multiplicity and the impact parameter for the 1.15 GeV/n Au + Au system. There is an obvious linear relationship, which is not exactly correct. The oversimplification of this method is justified because in this work only five impact parameter bins are presented, each of width 2 Fm. Given this wide bin size, the linear approximation is acceptable in the region from 2 – 10 Fm.

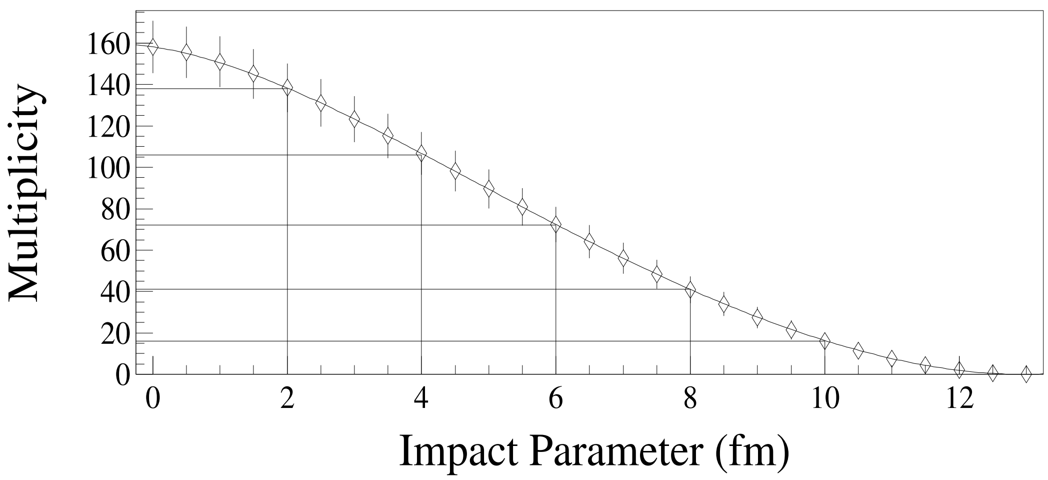

Figure 5.9: The relationship between impact parameter and the multiplicity. The fit shown is to a fifth order polynomial.

Chapter 6

Results

6.1 Introduction

Up to this point, the methods and motivations have been presented. The detectors, the data reduction methods, the detector response, and the analysis methods, have all been discussed. In this chapter, the results for squeeze-out and flow of protons and both species of pions are shown.

6.2 Squeeze-out

Squeeze-out is an enhanced emission of particles perpendicular to the reaction plane. Shown in Figures 6.1 and 6.2 are two representations of the distribution of protons as a function of normalized center-of-mass rapidity (Y_{cm}/Y_{beam}) and azimuthal angle with respect to the reaction plane (ϕ_{rp}). $\phi_{rp} = 0$ is in the reaction plane, and in the same direction as the Q-vector (recall Equation 5.1). $\phi_{rp} = 180$ and $\phi_{rp} = -180$ are also in the reaction plane, but in the opposite direction from the Q-vector. Peaks at $\phi_{rp} = 90°$ and $-90°$ indicate squeeze-out.

The nine panels of Figures 6.1 and 6.2 show this distribution for different transverse momentum cuts. (Transverse momentum is perpendicular to the beam axis.) Here, all multiplicity bins have been used. Later, these plots will be shown as a function of impact parameter. The protons in Figure 6.1 have a sort of squashed, inverted "V" shape. In Figures 6.3 through 6.6 these same plots are shown for π^+ and π^-. The transverse momentum for protons can be much greater than that of the pions, so there are fewer transverse momentum bins for the pions.

All of the previously mentioned figures are shown in two ways since the gray-scale plots are a bit misleading in this manner: each panel is scaled to itself. So, the blackest region indicating the most counts in the lowest p_t panel actually has many more counts than the blackest bin in one of the higher p_t panels. For example, the sixth panel of Figure 6.1 has a peak value of only about 20% of the peak in the first panel. It is possible to scale them so they all have the same maximum. If one does this, however, the peaks in the higher p_t bins are so low compared to those of the low p_t bins, that one cannot even see the shape of the higher p_t bins. One can get an idea of the difference from the lego-style plots shown in Figures 6.2, 6.4, and 6.6. In the lego-style plots, however, it is almost impossible to see the overall features, such as the inverted "V" shape visible in the gray-scale plots such as Figure 6.1.

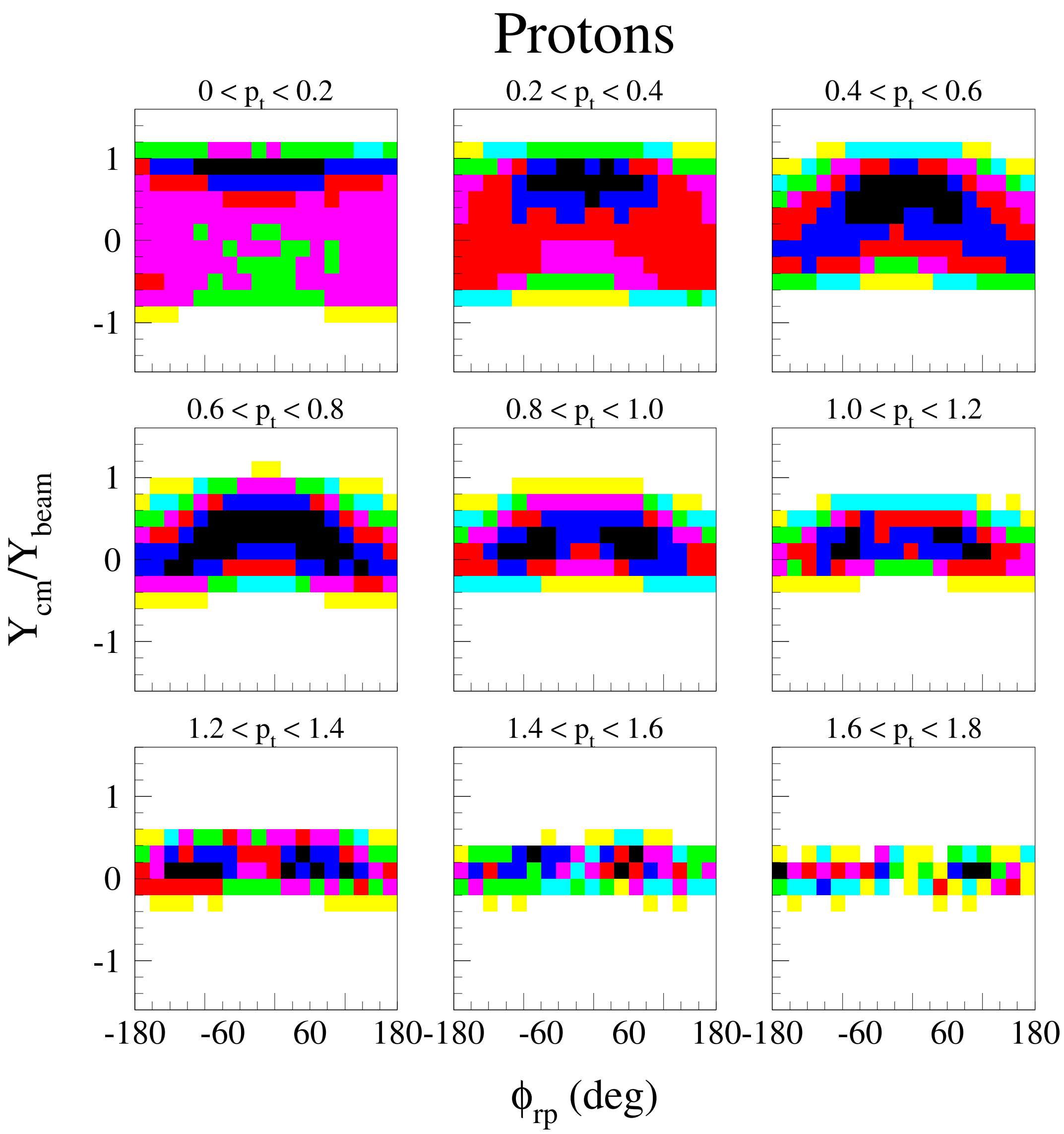

Figure 6.1: Yield of protons as a function of normalized center-of-mass rapidity and azimuthal angle with respect to the reaction plane.

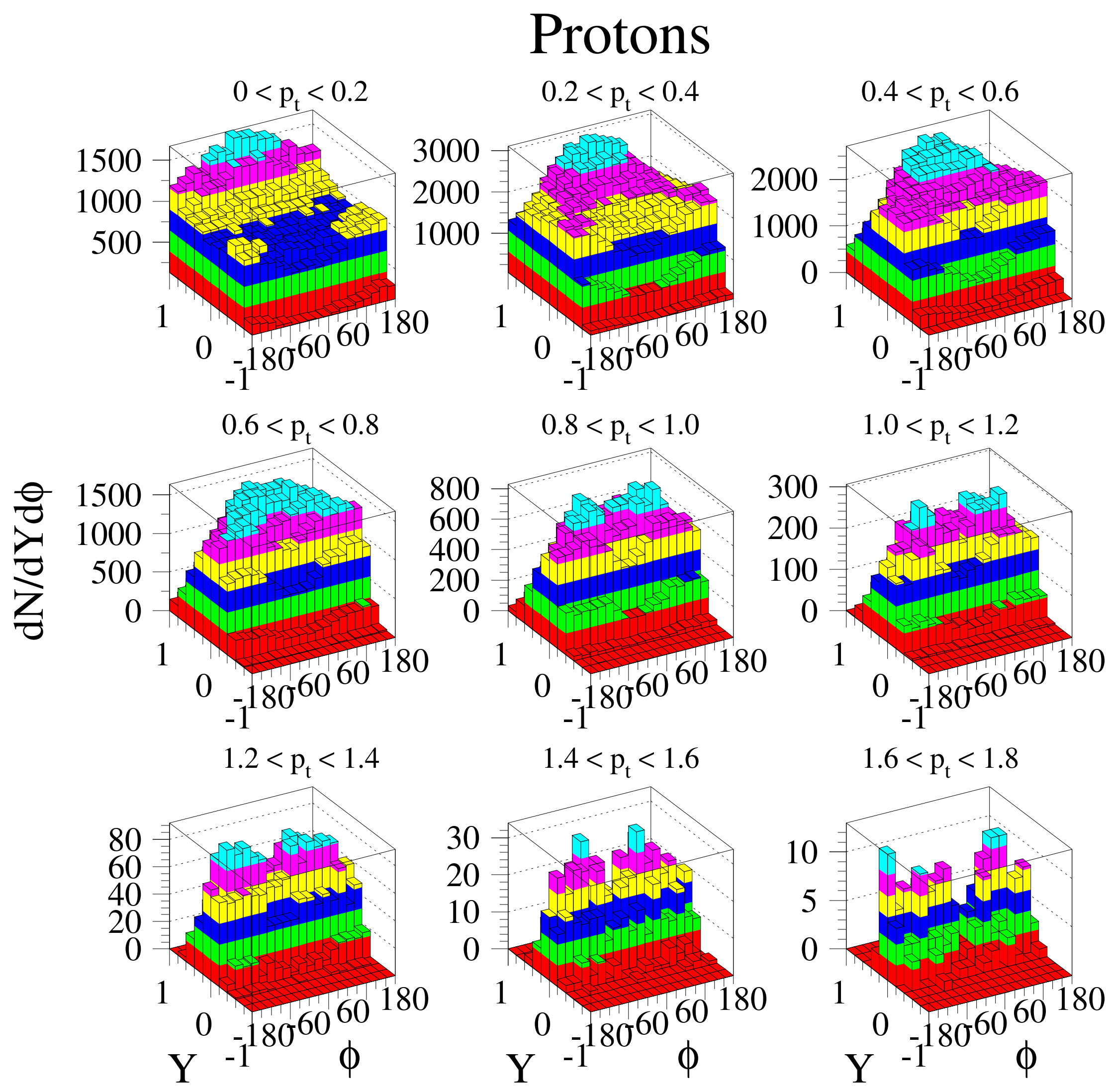

Figure 6.2: Yield of protons as a function of normalized center-of-mass rapidity and azimuthal angle with respect to the reaction plane. This is the same data as shown in the previous figure, but it is now possible to see the height of the peaks.

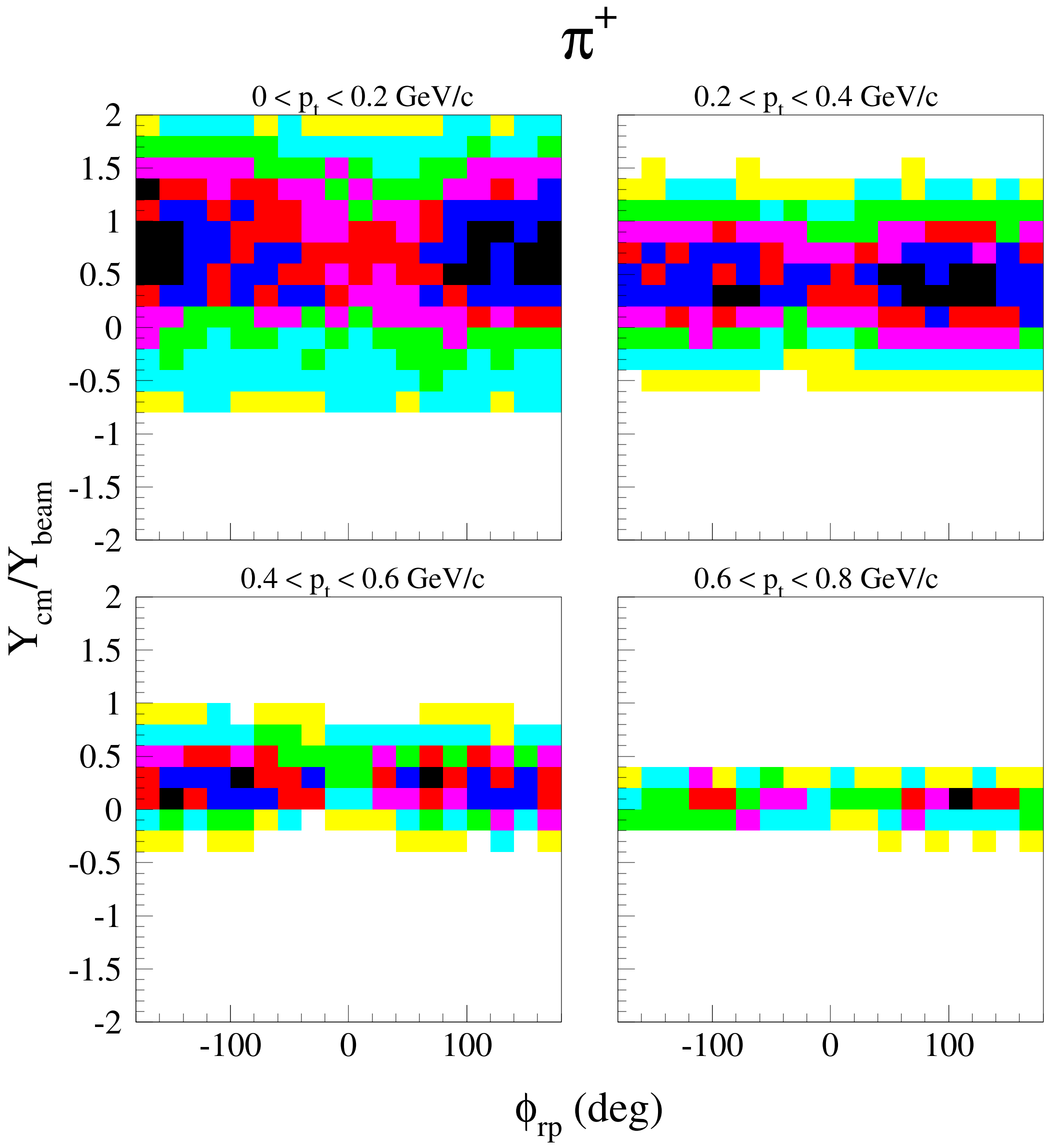

Figure 6.3: Yield of π^+ as a function of normalized center-of-mass rapidity and azimuthal angle with respect to the reaction plane.

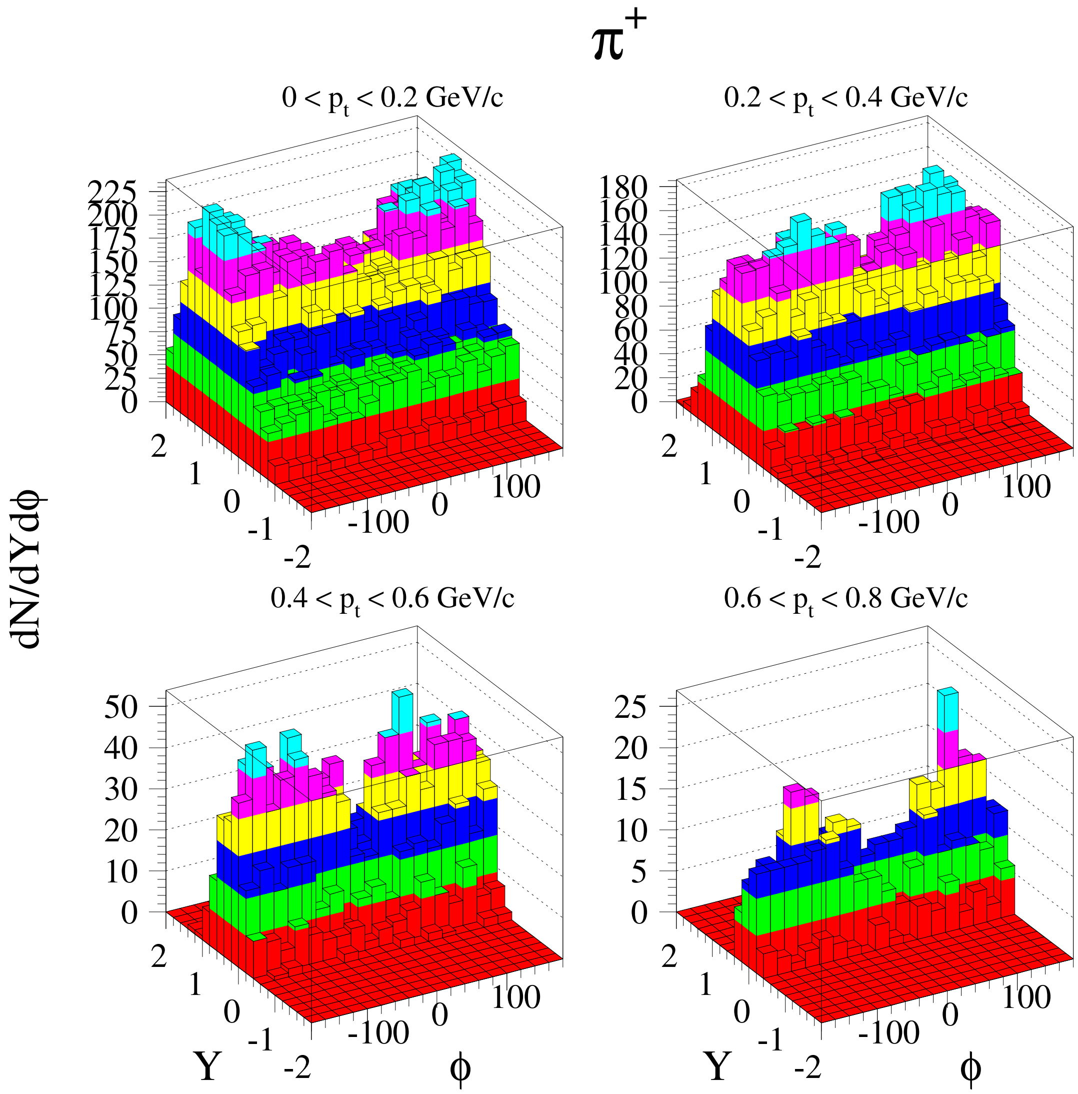

Figure 6.4: Yield of π^+ as a function of normalized center-of-mass rapidity and azimuthal angle with respect to the reaction plane. This is the same data as shown in the previous figure, but it is now possible to see the height of the peaks.

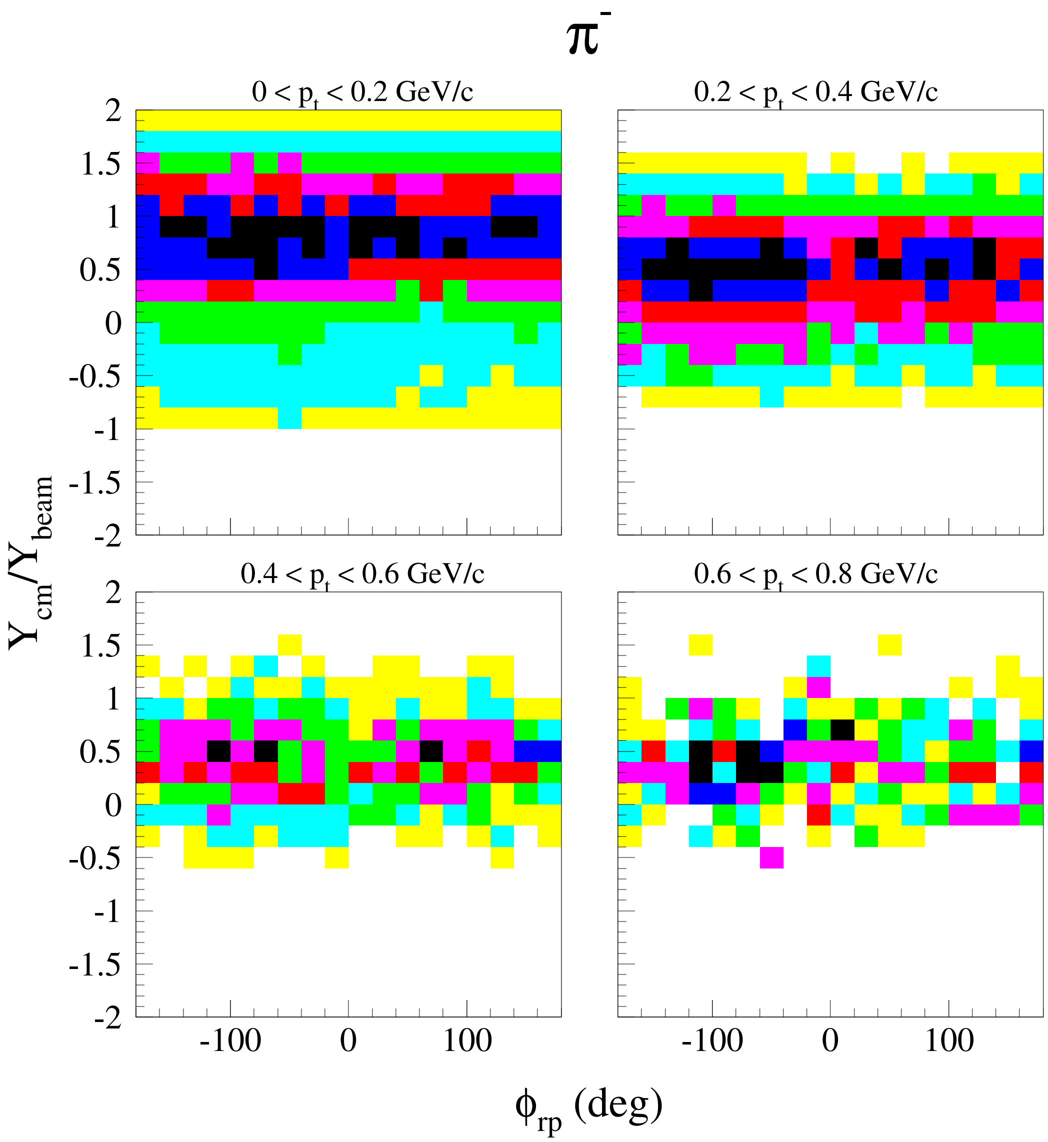

Figure 6.5: Yield of π^- as a function of normalized center-of-mass rapidity and azimuthal angle with respect to the reaction plane.

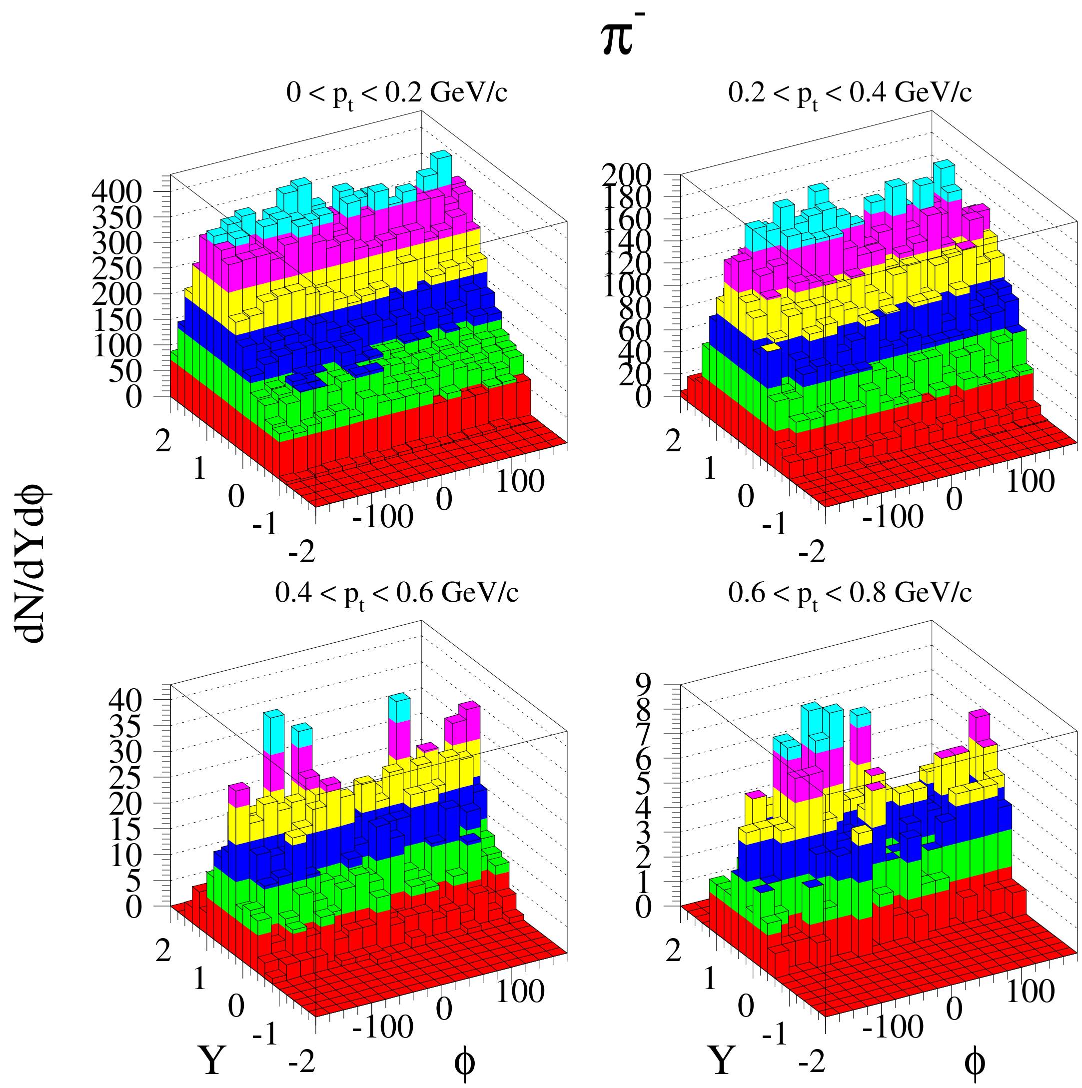

Figure 6.6: Yield of π^- as a function of normalized center-of-mass rapidity and azimuthal angle with respect to the reaction plane. This is the same data as shown in the previous figure, but it is now possible to see the height of the peaks.

The fact that the particles are not emitted uniformly from ϕ of $-180°$ to $180°$ for a given rapidity is significant. There are several very important features of the inverted "V" shape of the proton plots. First, the low p_t panels reveal strong peaking at $\phi = 0°$ for forward going particles. This is the signature of directed collective flow in the reaction plane. The projectile fragments, at $Y_{cm}/Y_{beam} = 1$ are strongly peaked at $0°$, although a significant fraction of particles in the lowest p_t bin are emitted with $Y_{cm}/Y_{beam} = 1$ at all angles from $-180°$ to $180°$.

As the p_t increases, the particles move away from the beam axis. What Figures 6.1, 6.3, and 6.5 show is that when particles are emitted away from the beam axis (denoted by larger p_t), they are emitted preferentially out of the reaction plane. For higher p_t, there are peaks at $90°$ and $-90°$. This will be seen more clearly when these 2 dimensional plots are projected to 1 dimensional plots in slices of rapidity.

Figure 6.1 and 6.2 show that for all cases except the lowest three p_t bins, there are peaks for midrapidity ($Y_{cm}/Y_{beam} = 0$) at $\phi = 90°$ and $-90°$. This says that if a proton or pion is emitted perpendicular to the beam axis, it is preferentially emitted perpendicular to the reaction plane as well. This is the squeeze-out signal.

These midrapidity values are then plotted to see the squeeze-out signal more clearly. Shown in Figure 6.7 is the result for protons. Shown in Appendix A are the results of projections of the 2D plots into 1d plots corresponding to the rapidity bins of interest. The motivation for looking at all these is to see the maximum peaks more clearly. Looking at the data in this manner, it becomes obvious that the maximum proton squeeze-out (for all impact parameters) is for $0 < Y_{cm}/Y_{beam} < 0.2$. This can also be seen qualitatively in the 2d plot, but it is not quantified.

The pions do not quite form such inverted "V" shapes. They seem to come out in two bunches centered on the line $Y_{cm}/Y_{beam} = 0.5$. If one views the corresponding projections for the pions (see Appendix A), there is a squeeze-out signal for panels corresponding to $0.2 < Y_{cm}/Y_{beam} < 0.8$. Therefore, Figures 6.8 and 6.9 are not projections at midrapidity as were the protons, but rather at forward rapidity ($0.2 < Y_{cm}/Y_{beam} < 0.8$). The KaoS Collaboration [Bril93] also looked at forward rapidities to see π^+ squeeze-out in 1.0 GeV/n Au + Au.

The fits shown are to:

$$\frac{dN}{d\phi} = N(1 + S_1 \cos\phi + S_2 \cos 2\phi) \tag{6.1}$$

The $\cos\phi$ term has a period of 360° and is an indicator of the flow signal. The $\cos 2\phi$ term has a period of 180° and is a measure of the squeeze-out signal. Thus, to measure squeeze-out quantitatively with this method, one would like the S_1 term to be very nearly zero in the rapidity region used.

The squeeze-out ratio ($R_{out/in}$) is defined as the ratio of the number of particles emitted out of the reaction plane to the number of particles emitted in the reaction plane.

$$R_{out/in} = \frac{\frac{dN}{d\phi}(90^\circ) + \frac{dN}{d\phi}(-90^\circ)}{\frac{dN}{d\phi}(0^\circ) + \frac{dN}{d\phi}(180^\circ)} \tag{6.2}$$

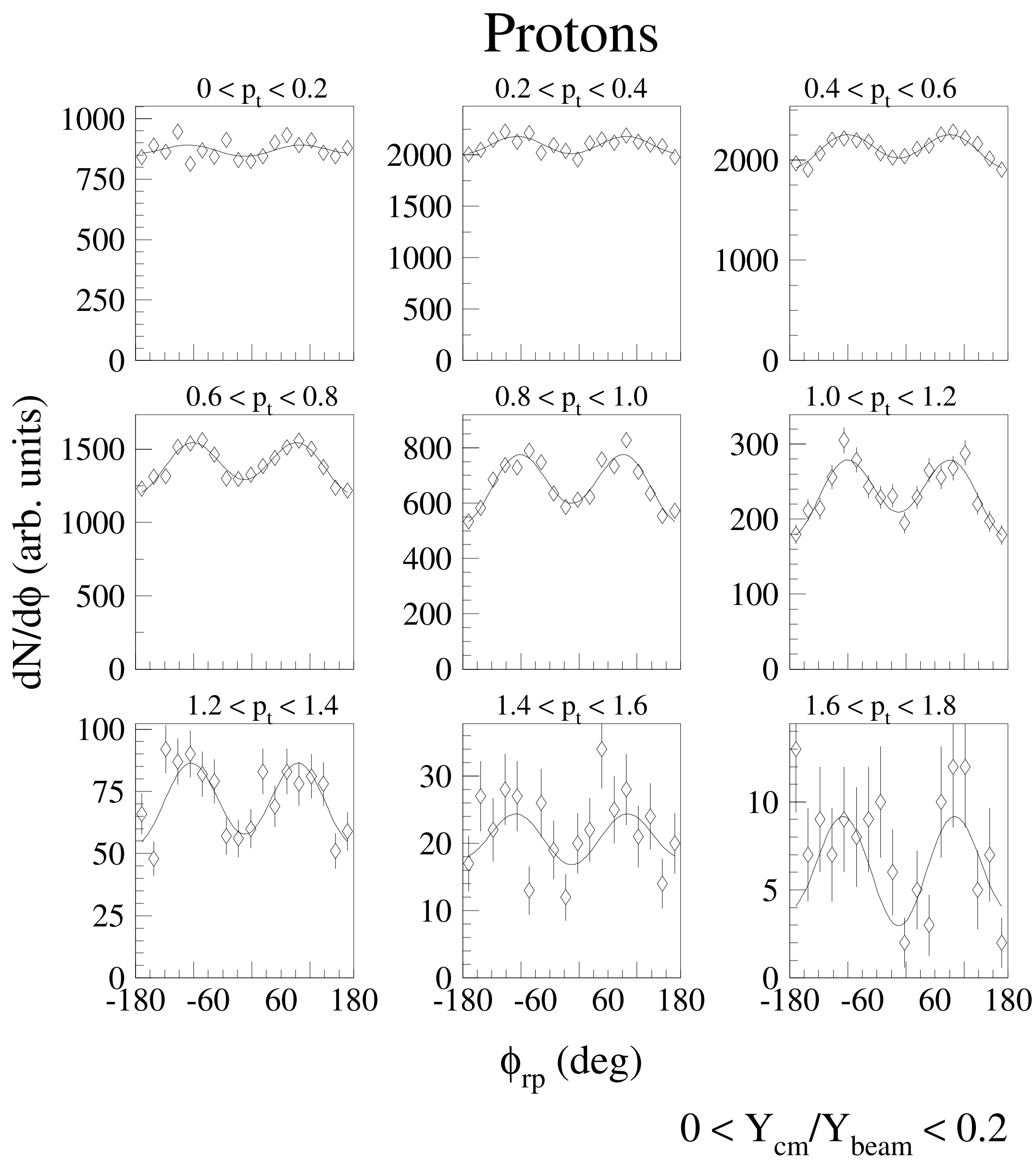

Figure 6.7: Yield of protons as a function of azimuthal angle with respect to the reaction plane with a cut to select midrapidity. The visible peaks at 90° and −90° in all but the lowest p_t bin indicate squeeze-out.

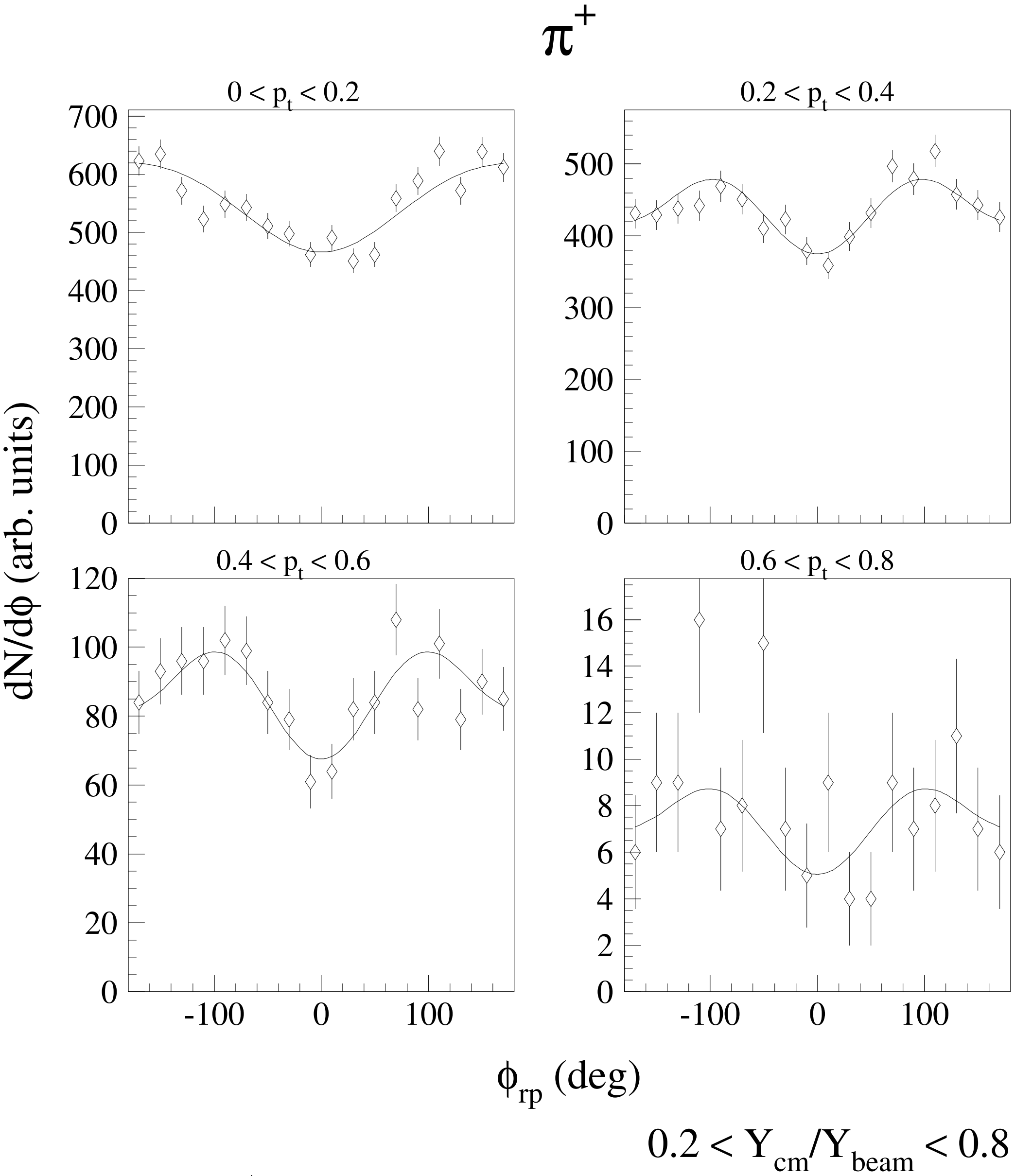

Figure 6.8: Yield of π^+ as a function of azimuthal angle with respect to the reaction plane with a cut on rapidity to maximize the squeeze-out. The visible peaks at 90° and −90° indicate squeeze-out.

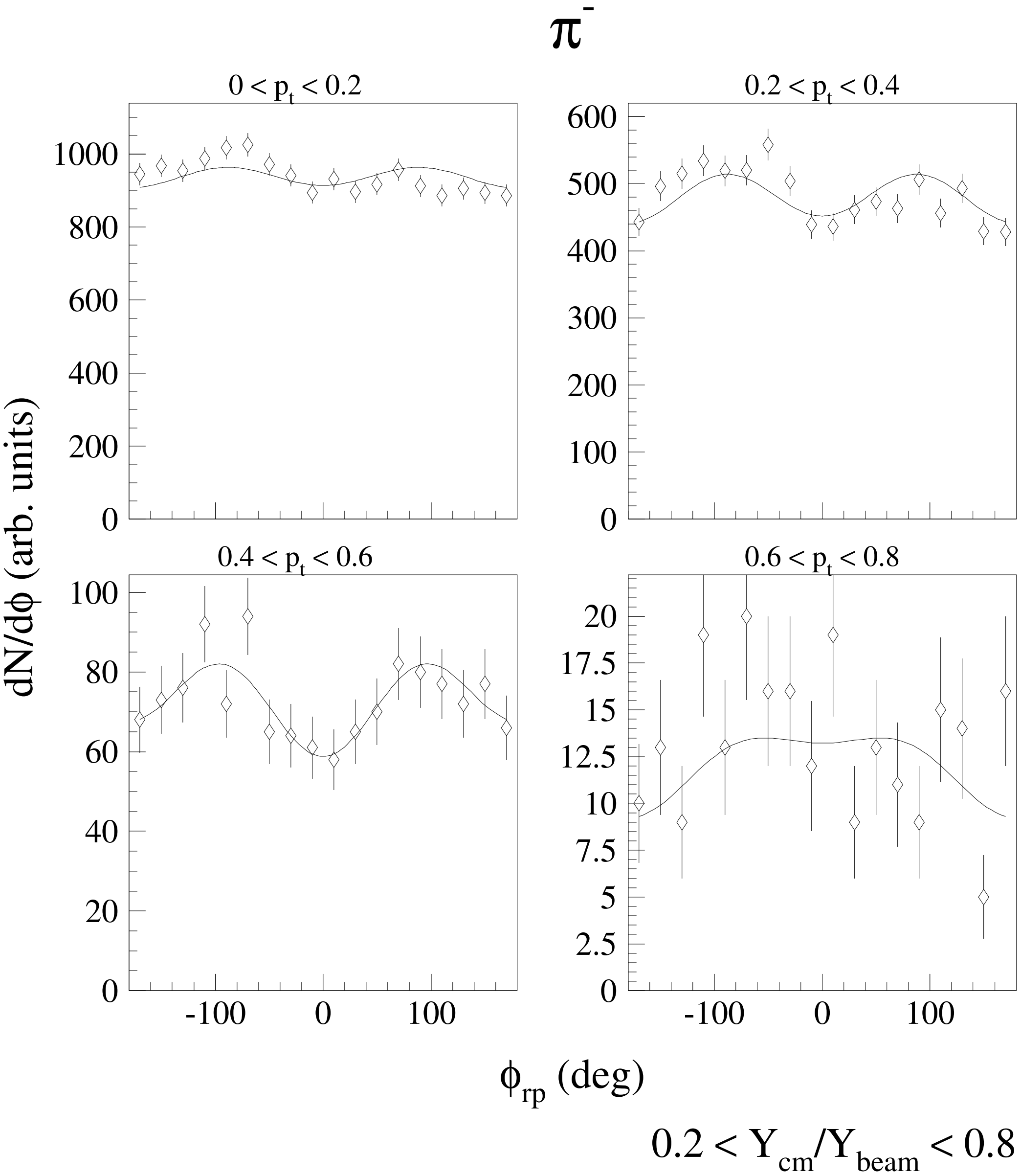

Figure 6.9: Yield of π^- as a function of azimuthal angle with respect to the reaction plane with a cut on rapidity to maximize the squeeze-out. The visible peaks at 90° and −90° indicate squeeze-out.

p_t (GeV/c)	S_1	S_2	χ^2	$R_{out/in}$
0 - 0.2	-0.0064 $\pm$ 0.0110	-0.023 $\pm$ 0.0110	1.53	1.05 $\pm$ 0.017
0.2 - 0.4	0.0005 $\pm$ 0.0072	-0.040 $\pm$ 0.0073	1.15	1.08 $\pm$ 0.011
0.4 - 0.6	0.0256 $\pm$ 0.0071	-0.068 $\pm$ 0.0073	0.72	1.14 $\pm$ 0.012
0.6 - 0.8	0.0350 $\pm$ 0.0087	-0.107 $\pm$ 0.0089	0.81	1.24 $\pm$ 0.016
0.8 - 1.0	0.0547 $\pm$ 0.0120	-0.158 $\pm$ 0.0130	1.49	1.38 $\pm$ 0.026
1.0 - 1.2	0.0714 $\pm$ 0.0210	-0.182 $\pm$ 0.0220	0.90	1.45 $\pm$ 0.046
1.2 - 1.4	0.0279 $\pm$ 0.0370	-0.215 $\pm$ 0.0390	1.35	1.55 $\pm$ 0.092
1.4 - 1.6	-0.0258 $\pm$ 0.0690	-0.168 $\pm$ 0.0710	1.58	1.40 $\pm$ 0.150
1.6 - 1.8	-0.0756 $\pm$ 0.1100	-0.454 $\pm$ 0.1200	1.51	2.67 $\pm$ 0.630

Table 6.1: Fit parameters and extracted values of $R_{out/in}$ for protons as a function of transverse momentum.

p_t (GeV/c)	S_1	S_2	χ^2	$R_{out/in}$
0 - 0.2	-0.139 $\pm$ 0.014	-0.013 $\pm$ 0.014	1.85	1.03 $\pm$ 0.021
0.2 - 0.4	-0.051 $\pm$ 0.016	-0.092 $\pm$ 0.016	0.93	1.20 $\pm$ 0.027
0.4 - 0.6	-0.086 $\pm$ 0.034	-0.134 $\pm$ 0.035	0.75	1.31 $\pm$ 0.067
0.6 - 0.8	-0.136 $\pm$ 0.120	-0.177 $\pm$ 0.120	0.99	1.43 $\pm$ 0.260

Table 6.2: Fit parameters and extracted values of $R_{out/in}$ for π^+ as a function of transverse momentum.

This can be written as:

$$R_{out/in} = \frac{1 - S_2}{1 + S_2} \tag{6.3}$$

where S_2 is the fit parameter from Equation 6.1 as mentioned above.

The squeeze-out ratio ($R_{out/in}$) and the fit parameters are shown in Tables 6.1, 6.2, and 6.3. Value for $R_{out/in} > 1$, or $S_2 < 0$, indicate squeeze-out. The values of $R_{out/in}$ for protons and both species of pions are also plotted in Figure 6.10.

A clear squeeze-out signal is seen for pions and protons as a function of transverse

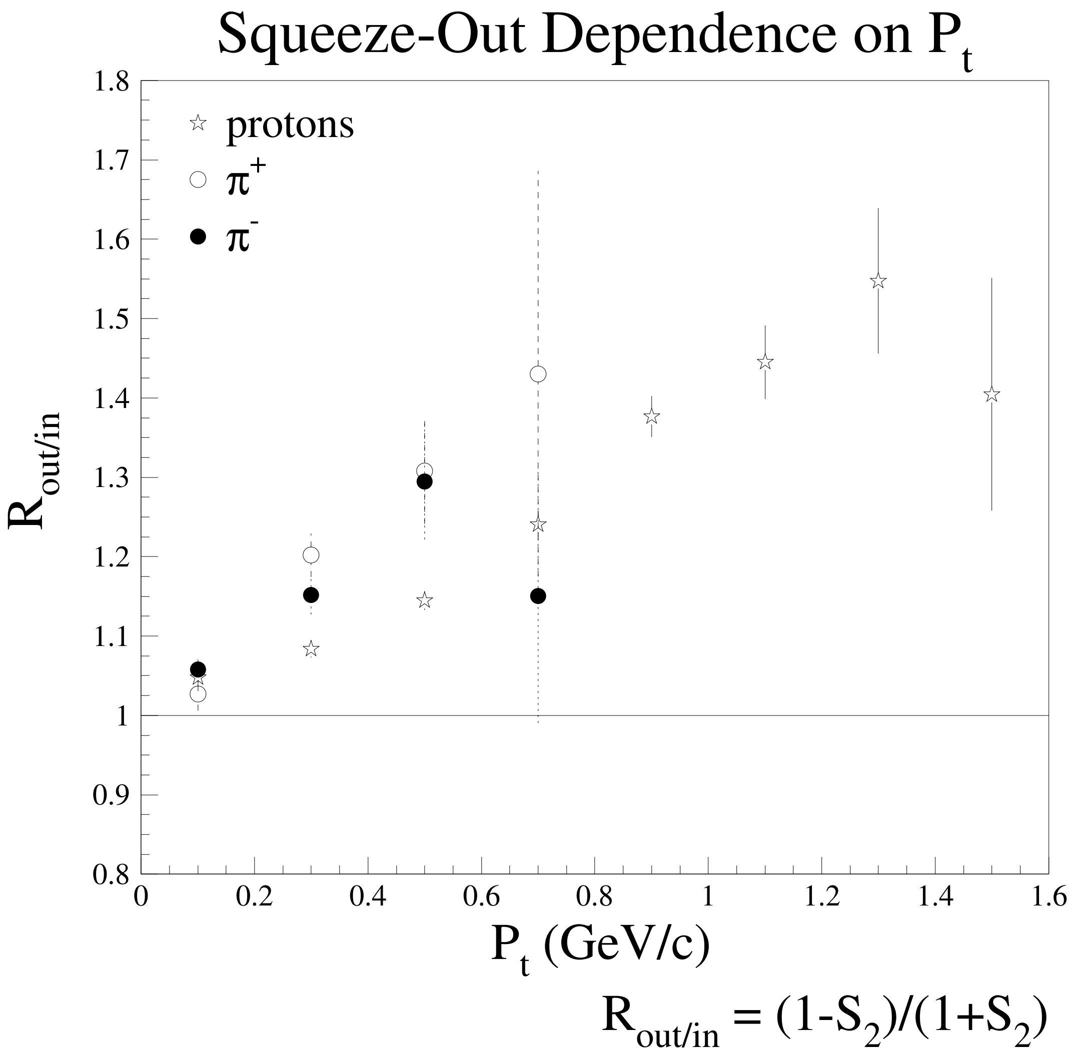

Figure 6.10: Extracted values of $R_{out/in}$ as a function of transverse momentum. Any value > 1 indicates squeeze-out. A clear increase as a function of p_t is observed.

p_t (GeV/c)	S_1	S_2	χ^2	$R_{out/in}$
0 - 0.2	0.004 ± 0.011	-0.028 ± 0.011	1.78	1.06 ± 0.016
0.2 - 0.4	0.011 ± 0.015	-0.070 ± 0.015	2.14	1.15 ± 0.025
0.4 - 0.6	-0.061 ± 0.038	-0.128 ± 0.039	0.48	1.29 ± 0.073
0.6 - 0.8	0.166 ± 0.094	-0.070 ± 0.098	1.46	1.15 ± 0.160

Table 6.3: Fit parameters and extracted values of $R_{out/in}$ for π^- as a function of transverse momentum.

momentum. The signal seems to increase linearly. The pion squeeze-out signal is larger than the proton signal for a given p_t bin. There does not seem to be any difference within the error bars between the two species of pions.

The increase as a function of p_t can be understood as follows: if a particle has a higher transverse momentum, it probably interacted less, and therefore was emitted out-of-plane, or away from target or projectile matter. The pions and protons experience squeeze-out for different causes. The protons exhibit compression effects, but the pions demonstrate the results of scattering. The pions emitted in the reaction plane are being absorbed by the heavy projectile and target spectators.

This analysis was repeated to study the dependence of squeeze-out on impact parameter. Shown in Figures 6.11, 6.12, and 6.13 are the same 2D style plots for protons, π^+, and π^- as shown in the last section, but here the panels correspond to different impact parameters. There is a cut of $p_t > 0.3\,GeV/c$ on all data shown in these figures. This cut is necessary to see the squeeze-out signal because the low p_t bins, which do not show much squeeze-out, dominate the statistics. Again similar shapes such as the inverted "V" are apparent for the protons. The pions appear to be emitted in two bunches at $90°$ and $-90°$ and forward rapidity.

Again the squeeze-out is seen at midrapidity for protons. If one makes projections in rapidity slice (see Appendix B), one finds for $0 < Y_{cm}/Y_{beam} < 0.2$ the characteristic squeeze-out signal as seen in Figure 6.14.

Although the pions do show a squeeze-out signal varying with impact parameter, it is for more forward going pions, exactly as in the case for increasing transverse momentum. Shown in Appendix B are all the relevant projections in slices of Y_{cm}/Y_{beam}. Figures 6.15 and 6.16 are the squeeze-out results for $0.2 < Y_{cm}/Y_{beam} < 0.8$ and $p_t > 0.3\,GeV/c$.

The fit parameters and the extracted values of $R_{out/in}$ are shown in Tables 6.4, 6.5, and 6.6, and $R_{out/in}$ is plotted vs. impact parameter in Figure 6.17. Here there are several interesting features. There appears to be a roughly linear increase to a peak at about $6\,Fm$, and then the squeeze-out ratio falls off. The protons clearly show this trend; it is significant to note their peak at $6\,Fm$, which as we will see in the next section is slightly less central than the flow peak. The pions seem to exhibit the same behavior with a slightly larger magnitude, lying just above the protons for most bins. This is similar to their relative behavior in the transverse momentum analysis.

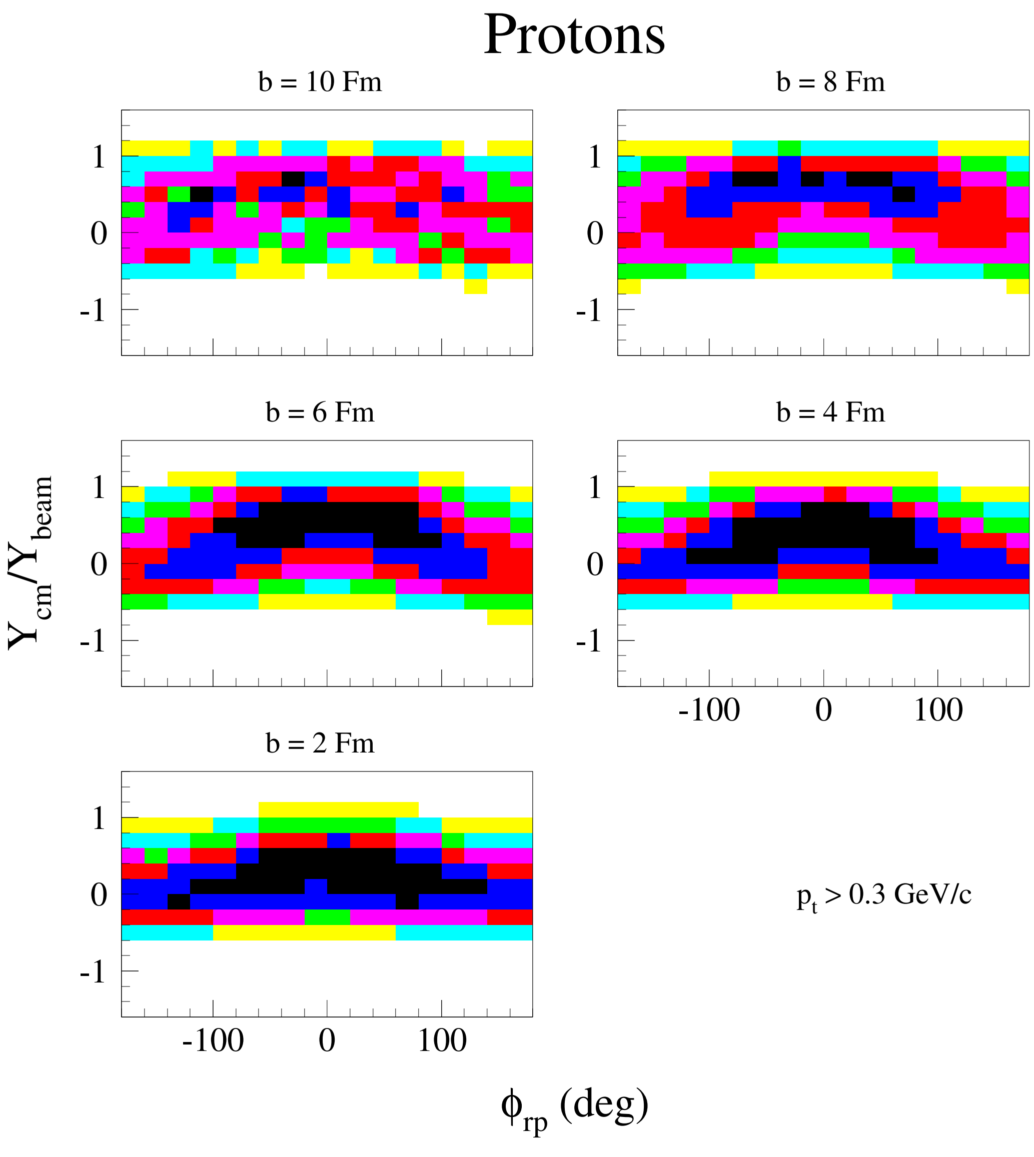

Figure 6.11: Yield of protons as a function of azimuthal angle with respect to the reaction plane for different impact parameters.

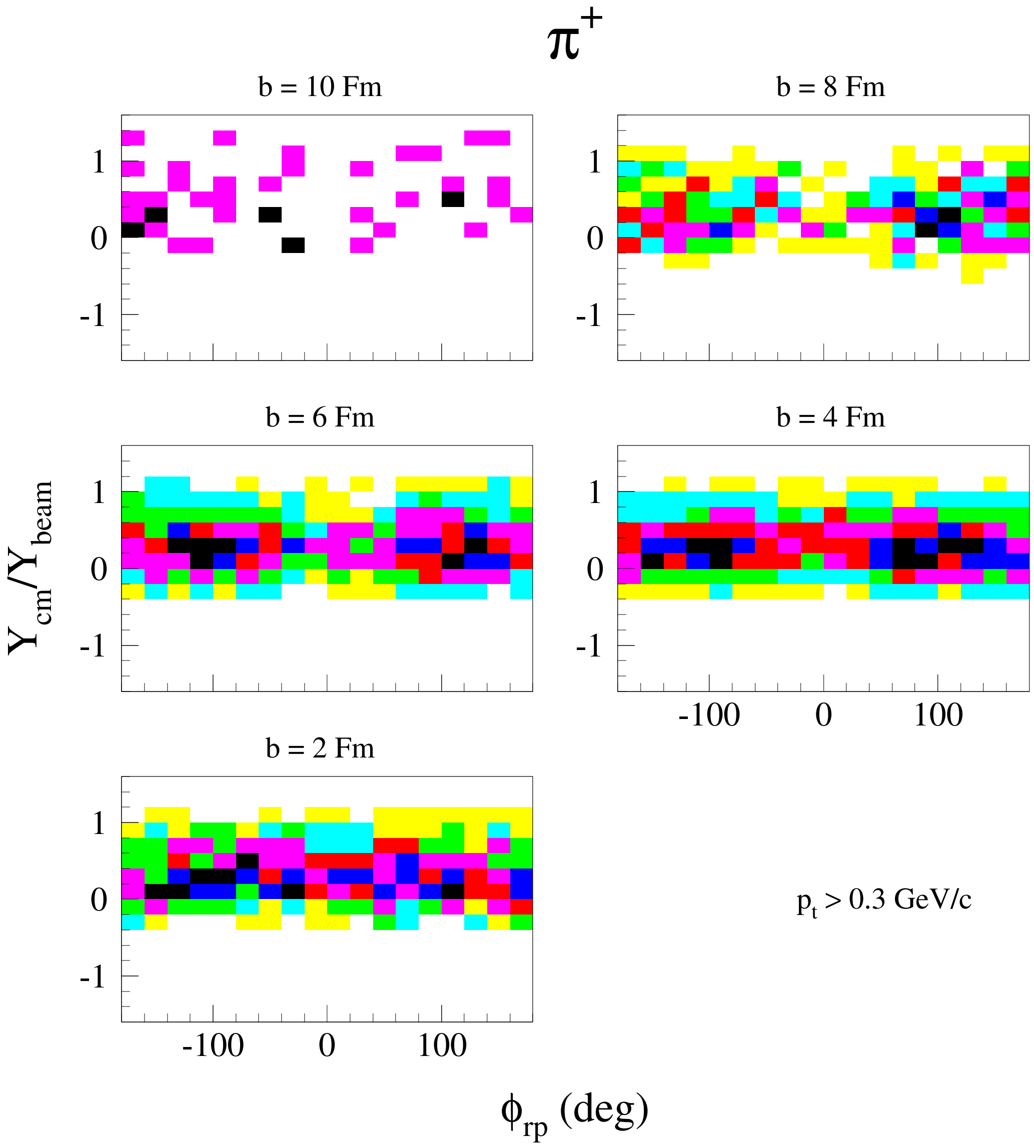

Figure 6.12: Yield of π^+ as a function of azimuthal angle with respect to the reaction plane for different impact parameters.

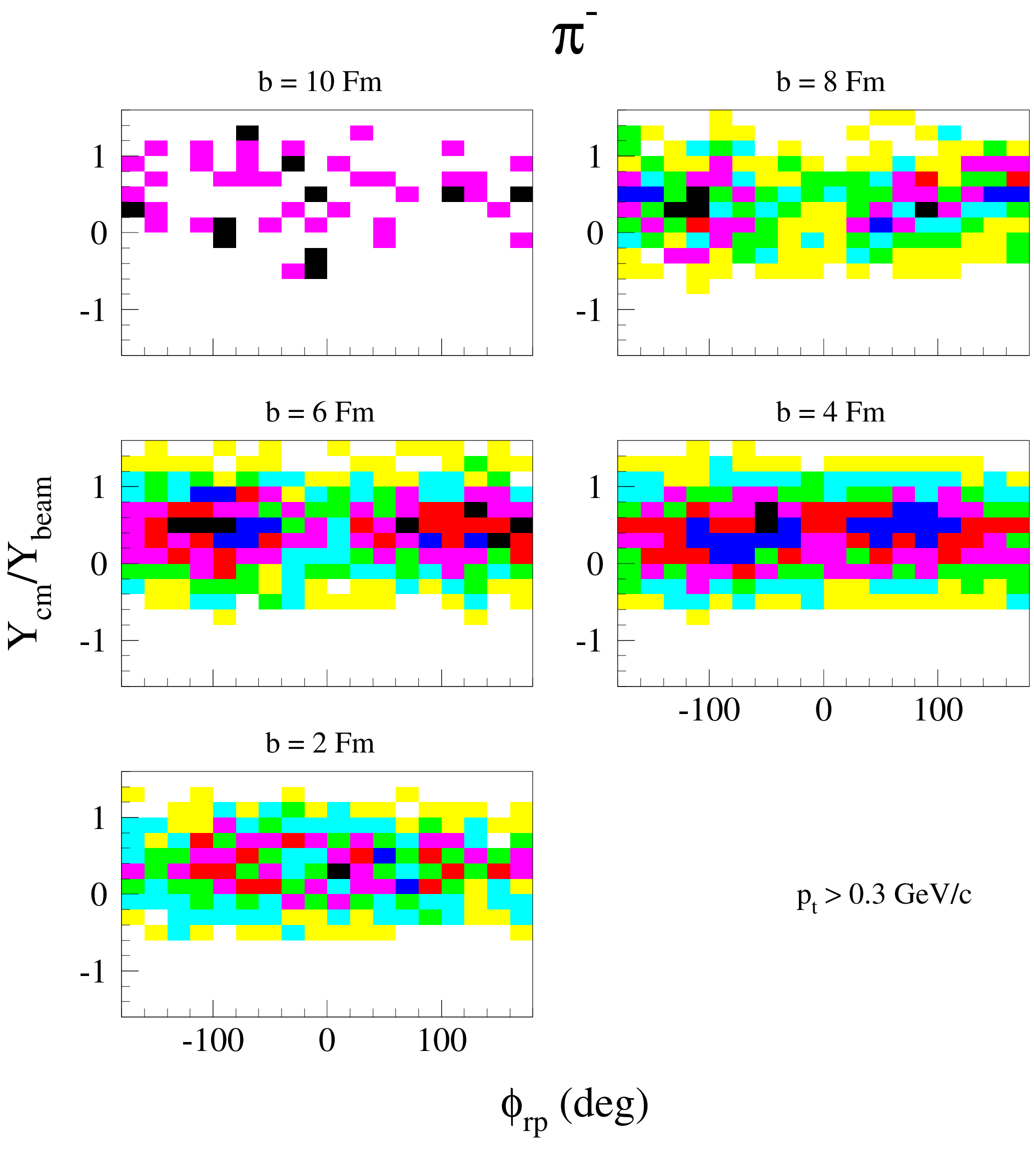

Figure 6.13: Yield of π^- as a function of azimuthal angle with respect to the reaction plane for different impact parameters.

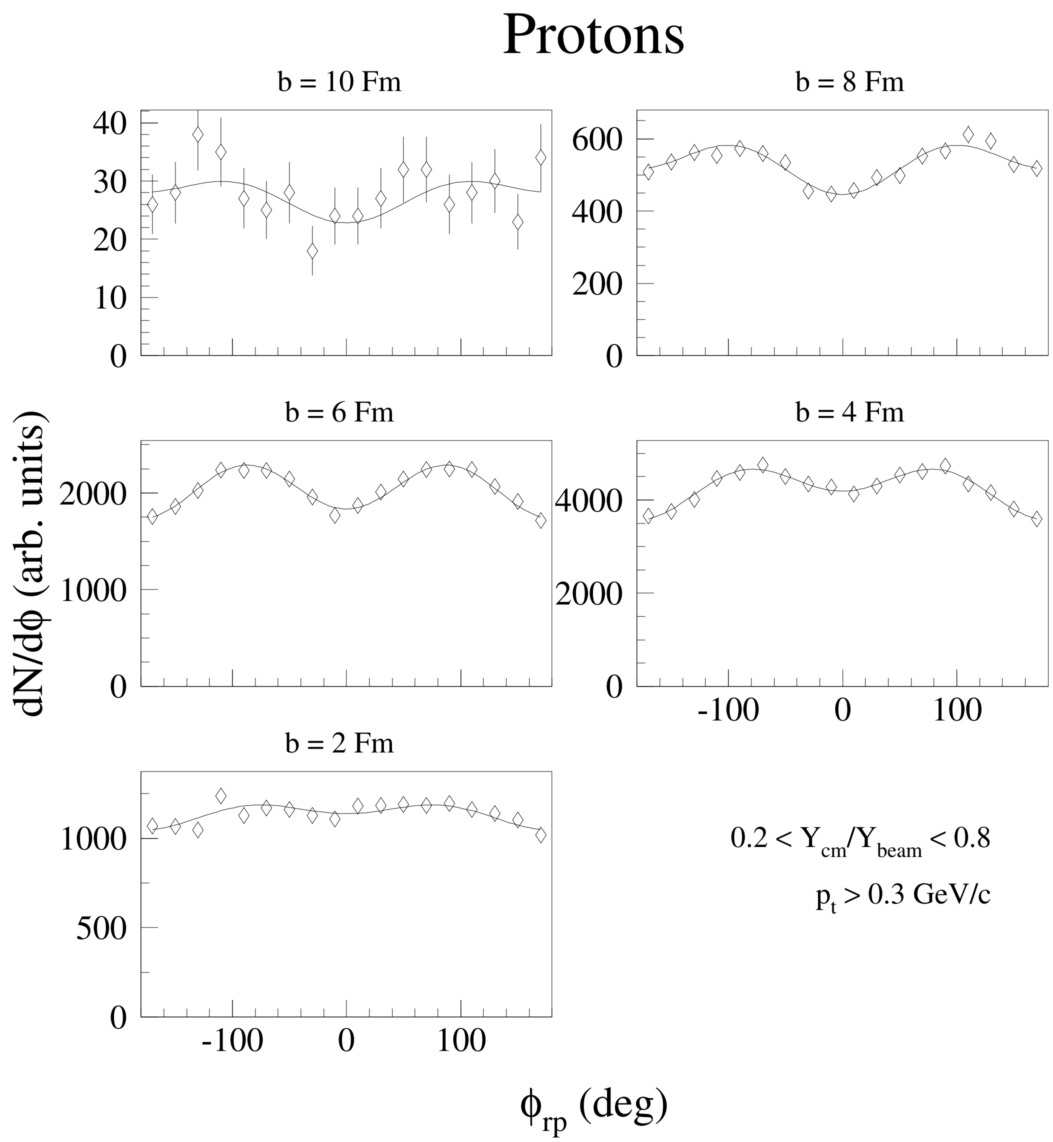

Figure 6.14: Yield of protons as a function of azimuthal angle with respect to the reaction plane for different impact parameters.

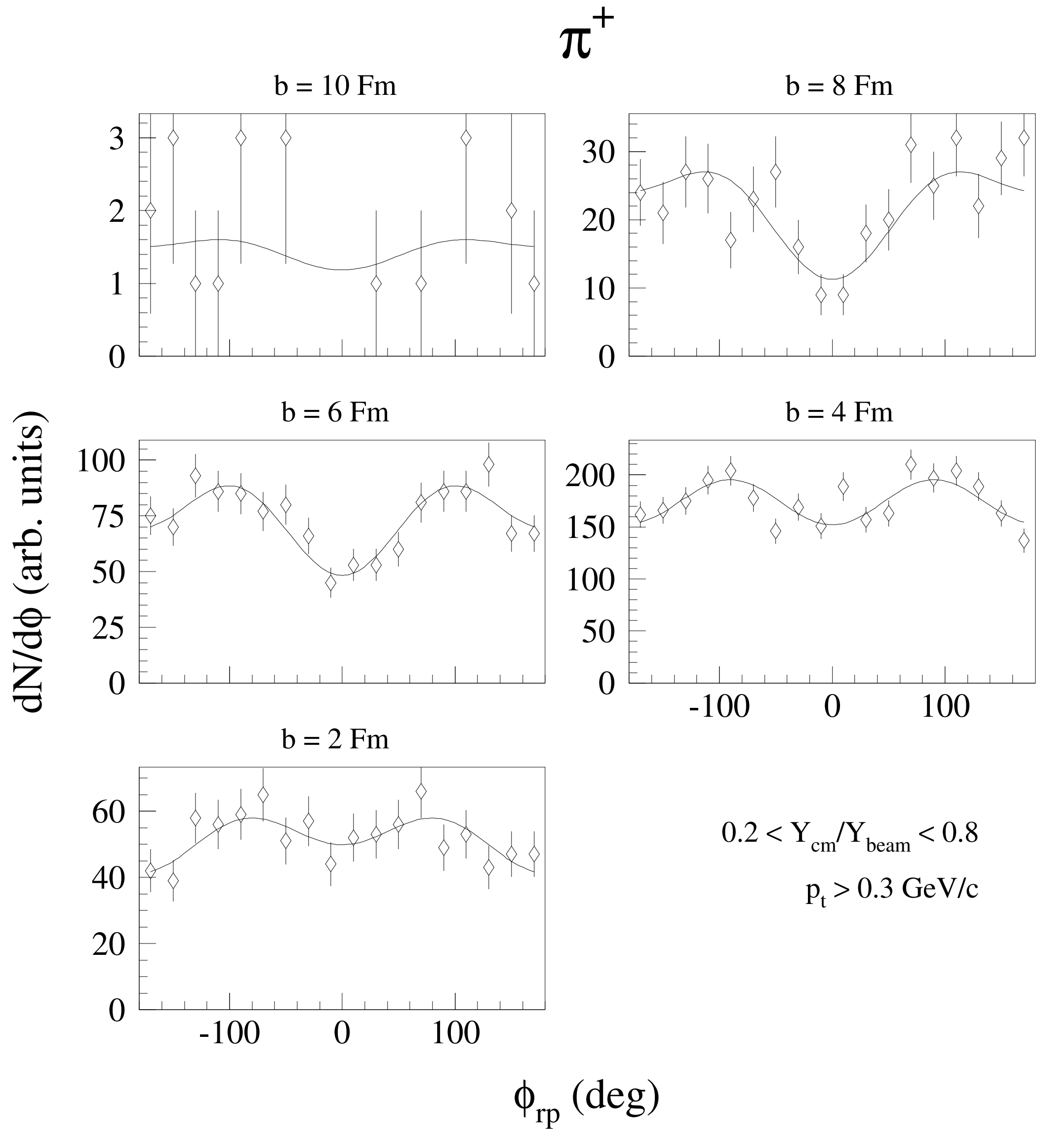

Figure 6.15: Yield of π^+ as a function of azimuthal angle with respect to the reaction plane for different impact parameters.

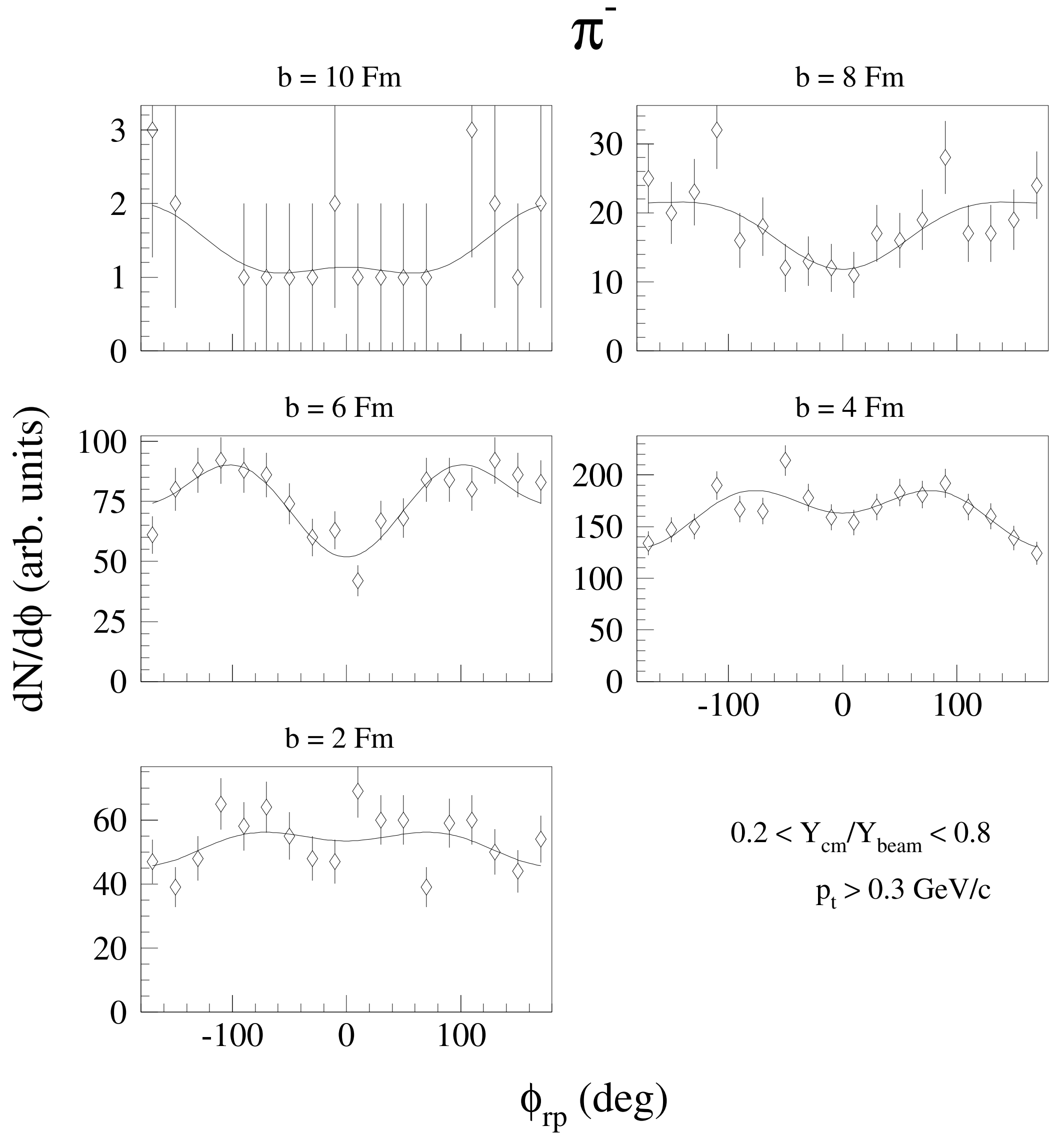

Figure 6.16: Yield of π^- as a function of azimuthal angle with respect to the reaction plane for different impact parameters.

$b(\ Fm)$	S_1	S_2	χ^2	$R_{out/in}$
10	-0.0949 $\pm$ 0.0620	-0.075 $\pm$ 0.0630	0.71	1.16 $\pm$ 0.100
8	-0.0663 $\pm$ 0.0140	-0.092 $\pm$ 0.0140	0.56	1.20 $\pm$ 0.025
6	0.0248 $\pm$ 0.0071	-0.124 $\pm$ 0.0073	0.78	1.28 $\pm$ 0.014
4	0.0732 $\pm$ 0.0050	-0.088 $\pm$ 0.0051	1.02	1.19 $\pm$ 0.009
2	0.0408 $\pm$ 0.0098	-0.039 $\pm$ 0.0099	1.30	1.08 $\pm$ 0.015

Table 6.4: Fit parameters and extracted values of $R_{out/in}$ for protons as a function of impact parameter.

$b(\ Fm)$	S_1	S_2	χ^2	$R_{out/in}$
10	-0.095 $\pm$ 0.062	-0.075 $\pm$ 0.063	0.71	1.16 $\pm$ 0.100
8	-0.066 $\pm$ 0.014	-0.092 $\pm$ 0.014	0.56	1.20 $\pm$ 0.025
6	0.025 $\pm$ 0.007	-0.124 $\pm$ 0.007	0.78	1.28 $\pm$ 0.014
4	0.073 $\pm$ 0.005	-0.088 $\pm$ 0.005	1.02	1.19 $\pm$ 0.009
2	0.041 $\pm$ 0.010	-0.039 $\pm$ 0.010	1.30	1.08 $\pm$ 0.015

Table 6.5: Fit parameters and extracted values of $R_{out/in}$ for π^+ as a function of impact parameter.

$b(\ Fm)$	S_1	S_2	χ^2	$R_{out/in}$
10	-0.313 $\pm$ 0.290	0.142 $\pm$ 0.320	0.21	0.75 $\pm$ 0.350
8	-0.265 $\pm$ 0.075	-0.084 $\pm$ 0.079	0.84	1.18 $\pm$ 0.130
6	-0.143 $\pm$ 0.036	-0.175 $\pm$ 0.037	0.81	1.42 $\pm$ 0.079
4	0.104 $\pm$ 0.025	-0.113 $\pm$ 0.026	0.94	1.25 $\pm$ 0.046
2	0.076 $\pm$ 0.045	-0.058 $\pm$ 0.047	1.42	1.12 $\pm$ 0.074

Table 6.6: Fit parameters and extracted values of $R_{out/in}$ for π^- as a function of impact parameter.

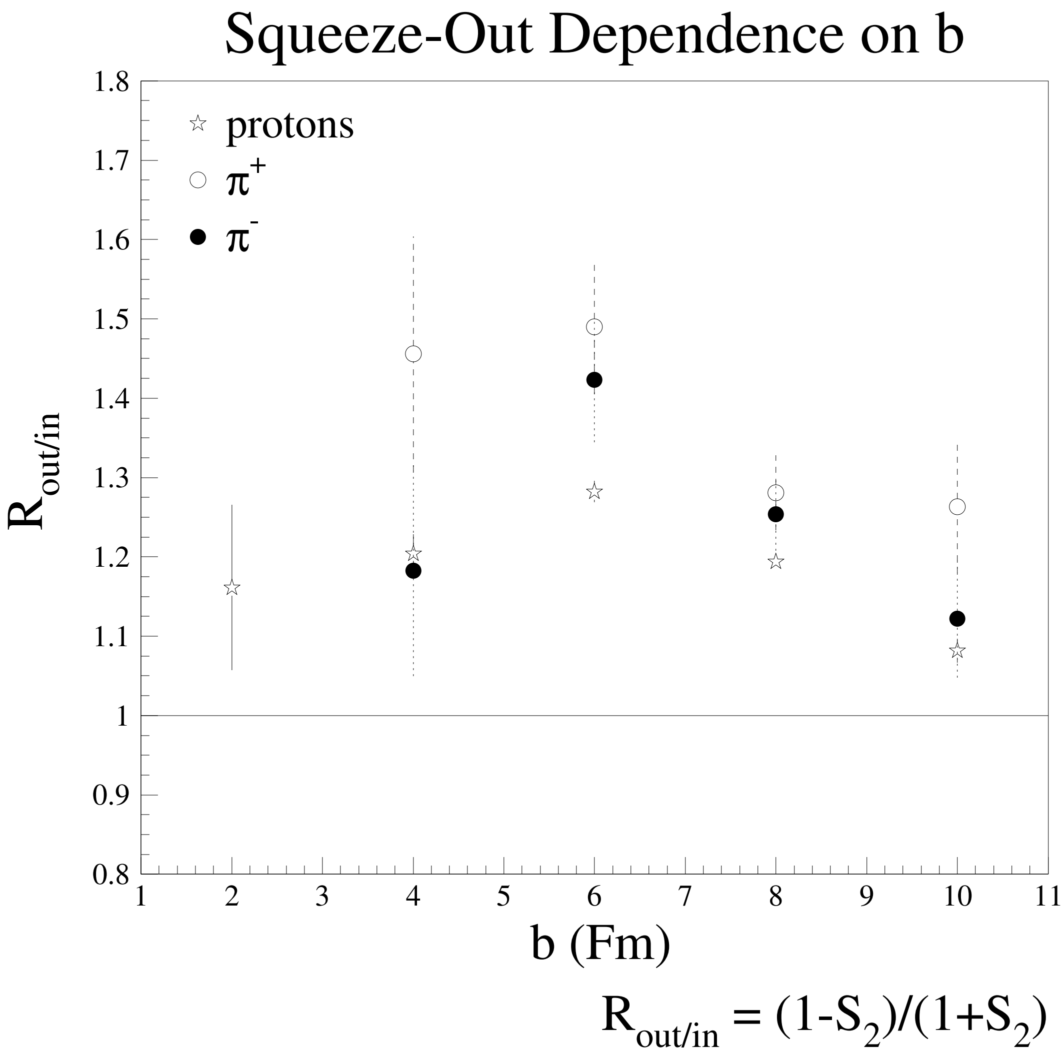

Figure 6.17: Extracted values of $R_{out/in}$ as a function of impact parameter. Any value > 1 indicates squeeze-out. There is a clear peak near $b = 6$ Fm for the protons, and the pions exhibit similar behavior within error bars.

6.3 Directed Collective Flow

Directed Collective Flow is defined as a preferential emission of forward going particles in one direction (backward going particles in the opposite direction) with respect to the reaction plane. The analysis methods were discussed in the last chapter. In this section flow results for protons and both species of pions are shown. Figures 6.18, 6.19, and 6.20 show plots of p_x/m vs. normalized center-of-mass rapidity. Several things are obvious from these plots. There is a clear detector bias, in that the plots should be symmetric around zero for forward and backward going particles. And there is a definite shape to the figures.

By taking the average p_x/m for each rapidity slice, one observes the "S-curve." The plots are called S-curves because of the characteristic shape as seen for the protons. Figure 6.21 shows the S-curves for protons for the impact parameters measured. The use of p_x/m, as opposed to the more tradition p_x/A provides a natural scaling between protons and pions. Actual mass in GeV/c^2 is used; so the units of p_x/m are simply $\frac{GeV/c}{GeV/c^2} = c$.

Presented in this section are the first S-curves for pions as a function of impact parameter. The next several figures show protons and pions with the fits used to describe flow. Figures 6.22, 6.23, and 6.24 show the flow results for protons, π^+, and π^- respectively. The fits shown here are all linear in the midrapidity range. The slope of the fit at midrapidity is the variable, "Flow," as described here. The fit parameters are extracted and corrected for the reaction plane dispersion (see Table 5.1); the

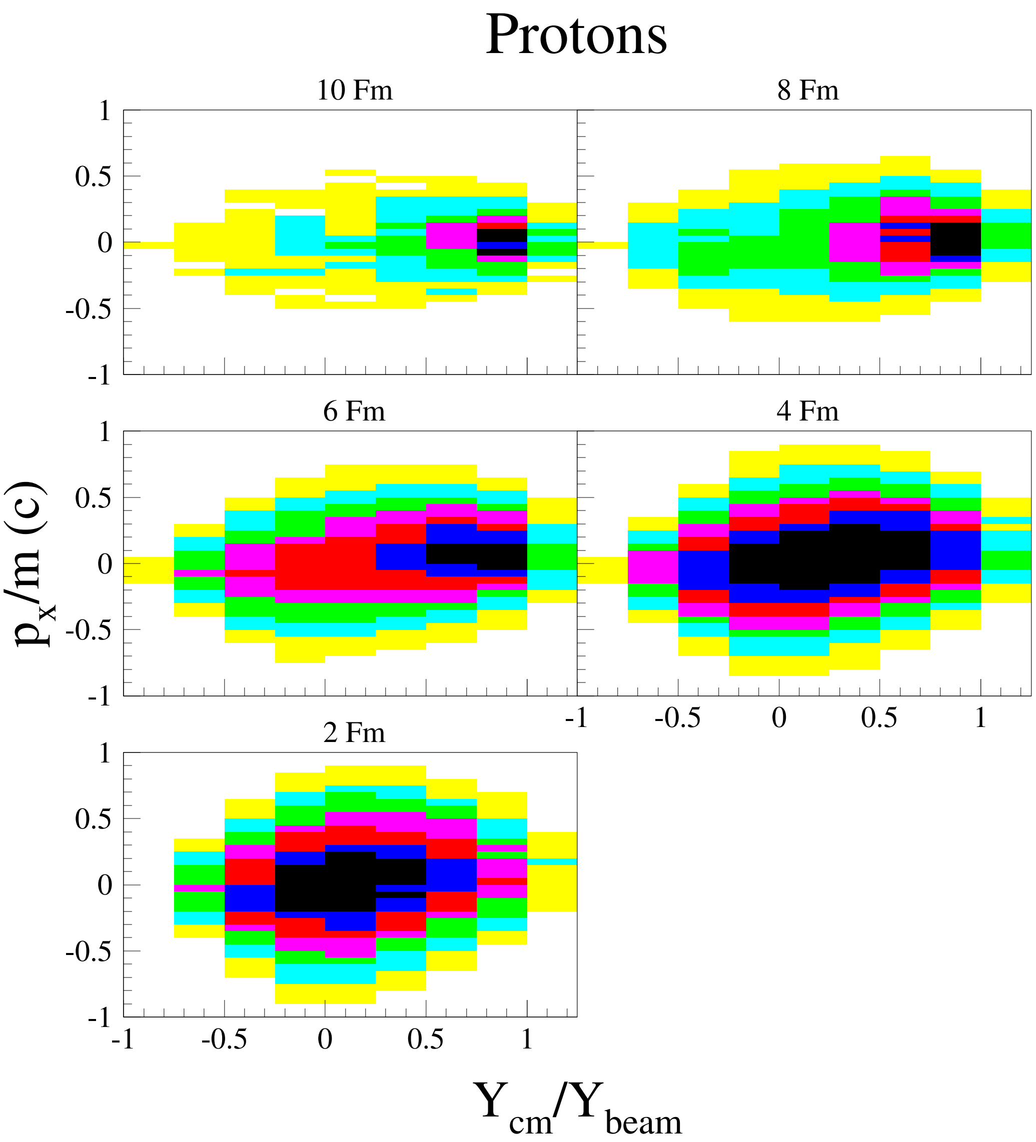

Figure 6.18: Plots of p_x/m vs normalized center of mass rapidity for protons for each of the different impact parameters measured.

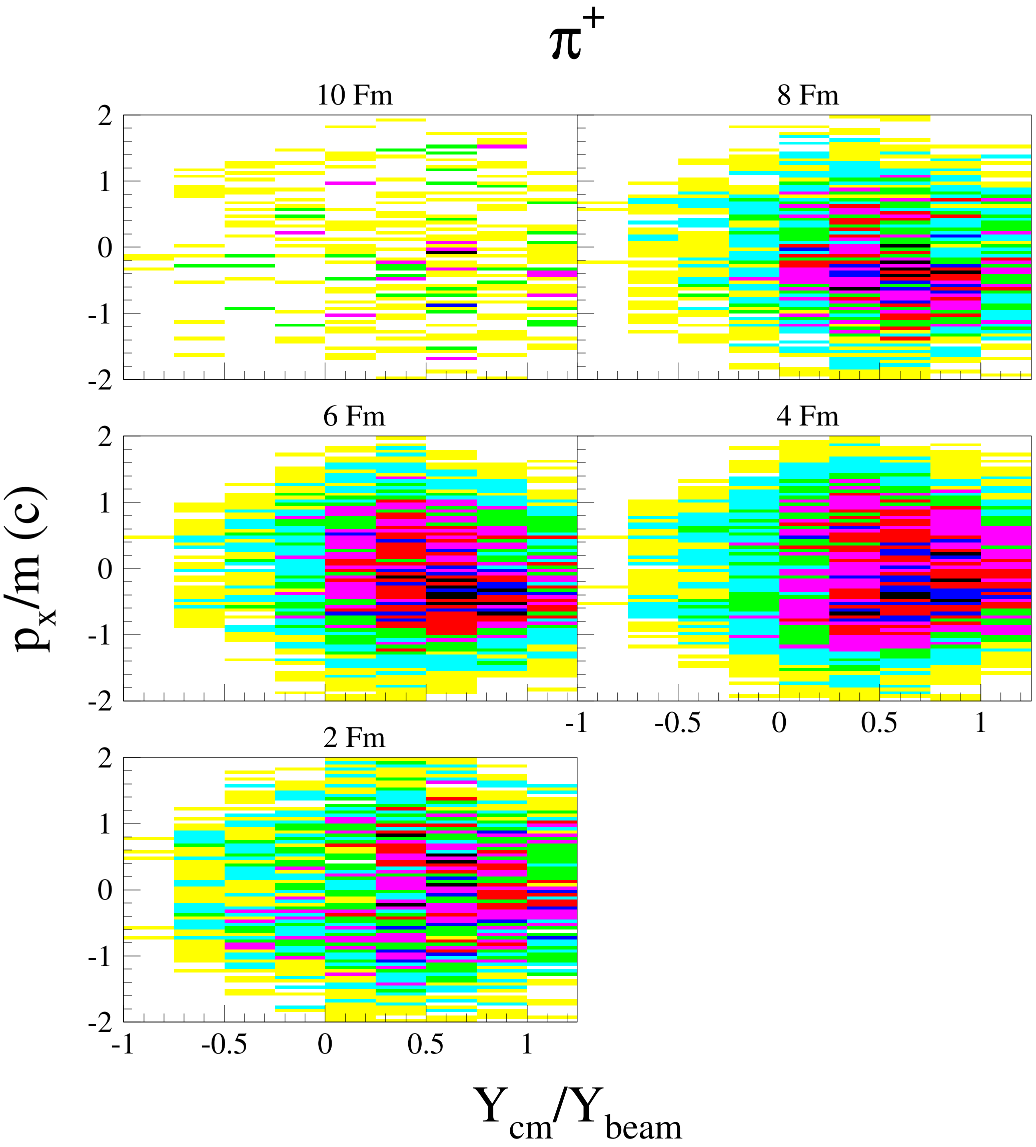

Figure 6.19: Plots of p_x/m vs normalized center of mass rapidity for π^+ for each of the different impact parameters measured.

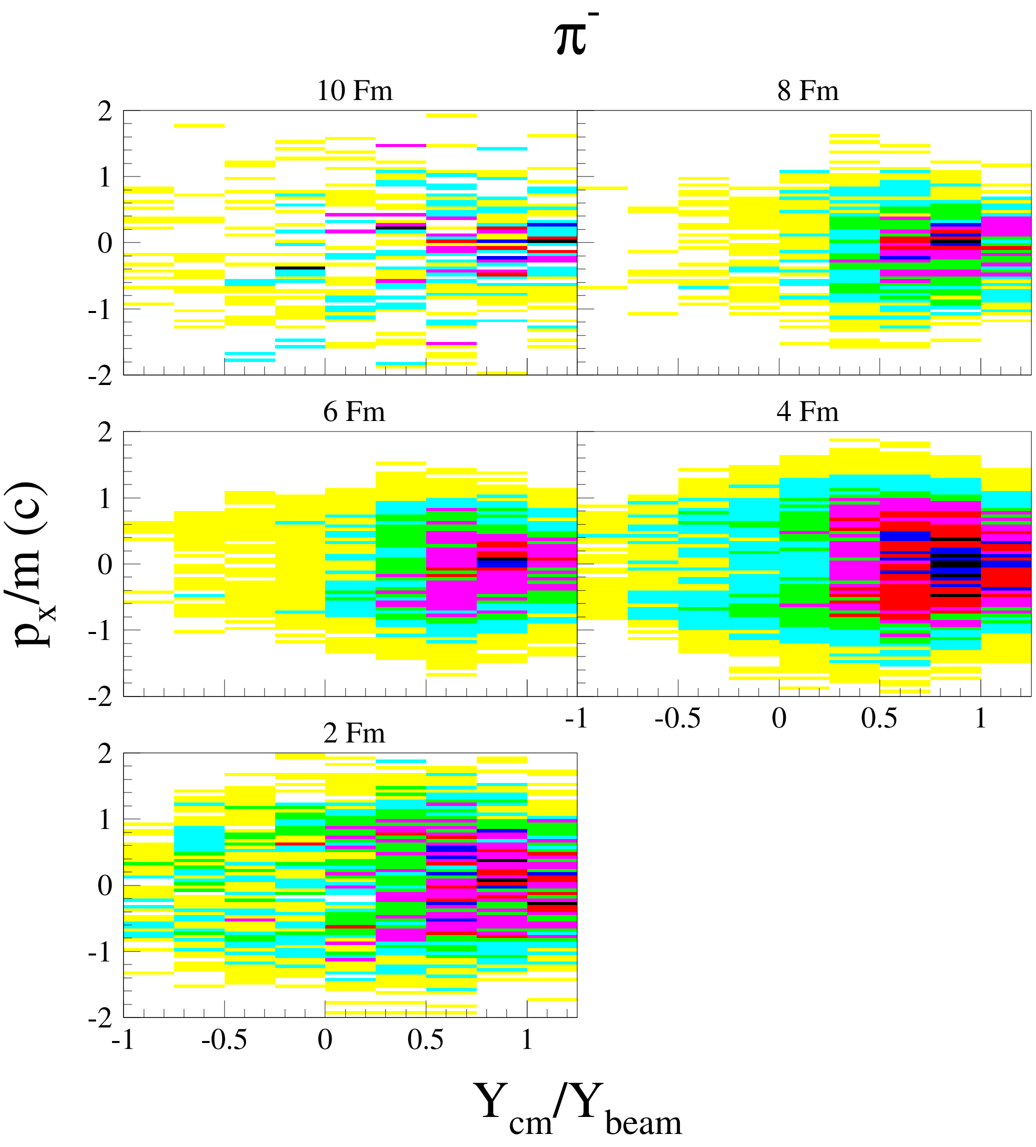

Figure 6.20: Plots of p_x/m vs normalized center of mass rapidity for π^- for each of the different impact parameters measured. The pions show much more forward peaking than the protons.

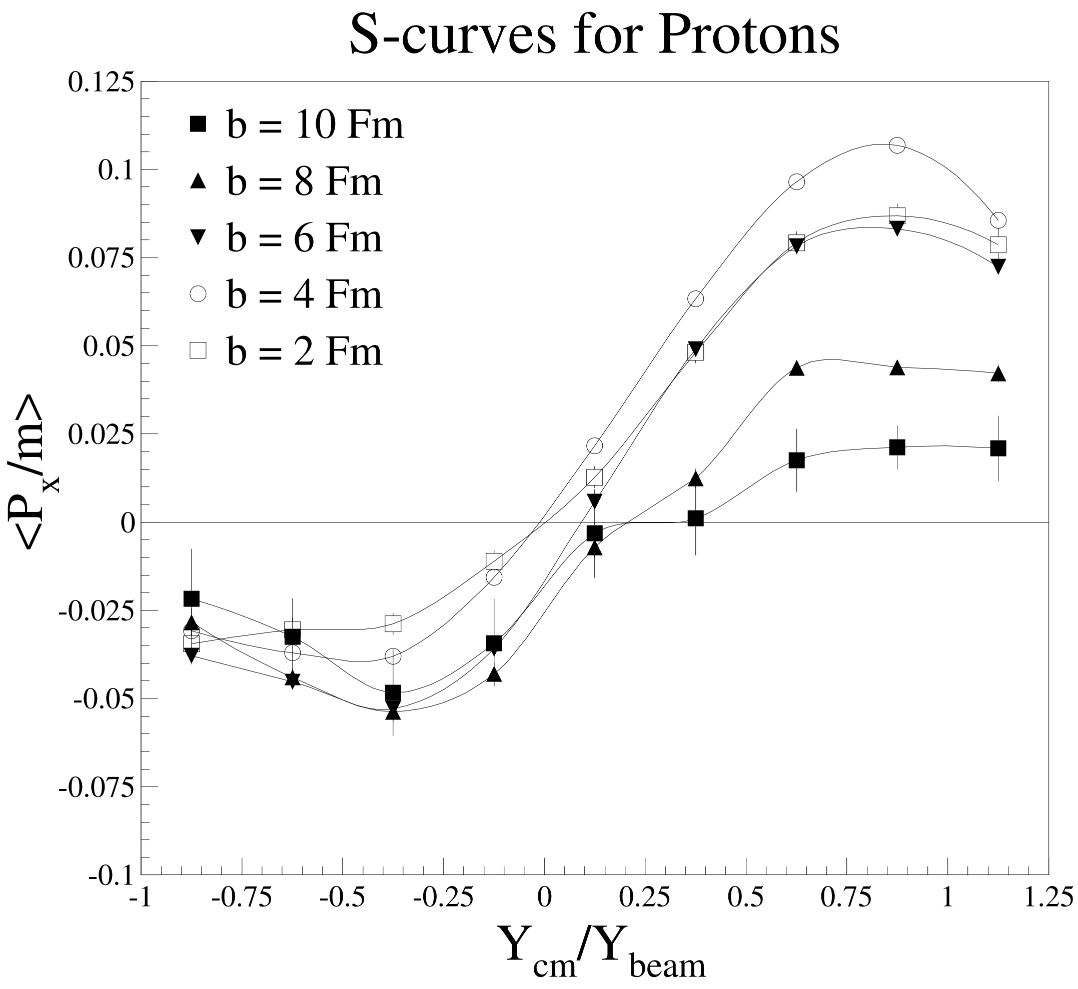

Figure 6.21: The S-curves for protons from 1.15 GeV/n Au + Au. The various symbols represent the different impact parameters measured. A clear impact parameter dependence with a maximum for the 4 Fm curve is observed. The lines are to guide the eye.

	Flow (c)		
b (Fm)	Protons	π^+	π^-
2	0.133 $\pm$ 0.008	0.046 $\pm$ 0.048	0.019 $\pm$ 0.063
4	0.149 $\pm$ 0.003	-0.035 $\pm$ 0.022	0.036 $\pm$ 0.031
6	0.143 $\pm$ 0.004	-0.134 $\pm$ 0.027	0.016 $\pm$ 0.039
8	0.104 $\pm$ 0.007	-0.148 $\pm$ 0.049	-0.038 $\pm$ 0.071
10	0.0443 $\pm$ 0.03019	0.0558 $\pm$ 0.23	0.24 $\pm$ 0.32

Table 6.7: Extracted flow values, or the slope at midrapidity of the S-curve, for protons, π^+, and π^-.

corrected values are shown in Table 6.7 and plotted in Figure 6.25.

As seen in Figure 6.25, there is a clear flow signature for protons as reported by Martin Partlan [Part94b]. The π^+ exhibit what is called "anti-flow," or, flow in a direction opposite to that of the baryons. The π^-, on the other hand, do not appear to show much flow at all. This difference between the π^+ and π^- was not evident in the Bass predictions [Bass95], although it is supported by the BUU model (without detector biases added) as will be seen in the next Chapter. This almost certainly means it is not an artifact of the detector acceptance.

An obvious difference between π^+ and π^- is charge. One can imagine the spectators giving the pions a Coulomb 'kick.' The π^+ would be pushed away from the positively charged spectators. A forward going π^+ would be repelled from the flow axis by the projectile spectator. This kick is in the anti-flow direction. The π^-, on the other hand, would be attracted to the spectators. Therefore, a forward going π^- would get kicked in, toward the proton flow direction.

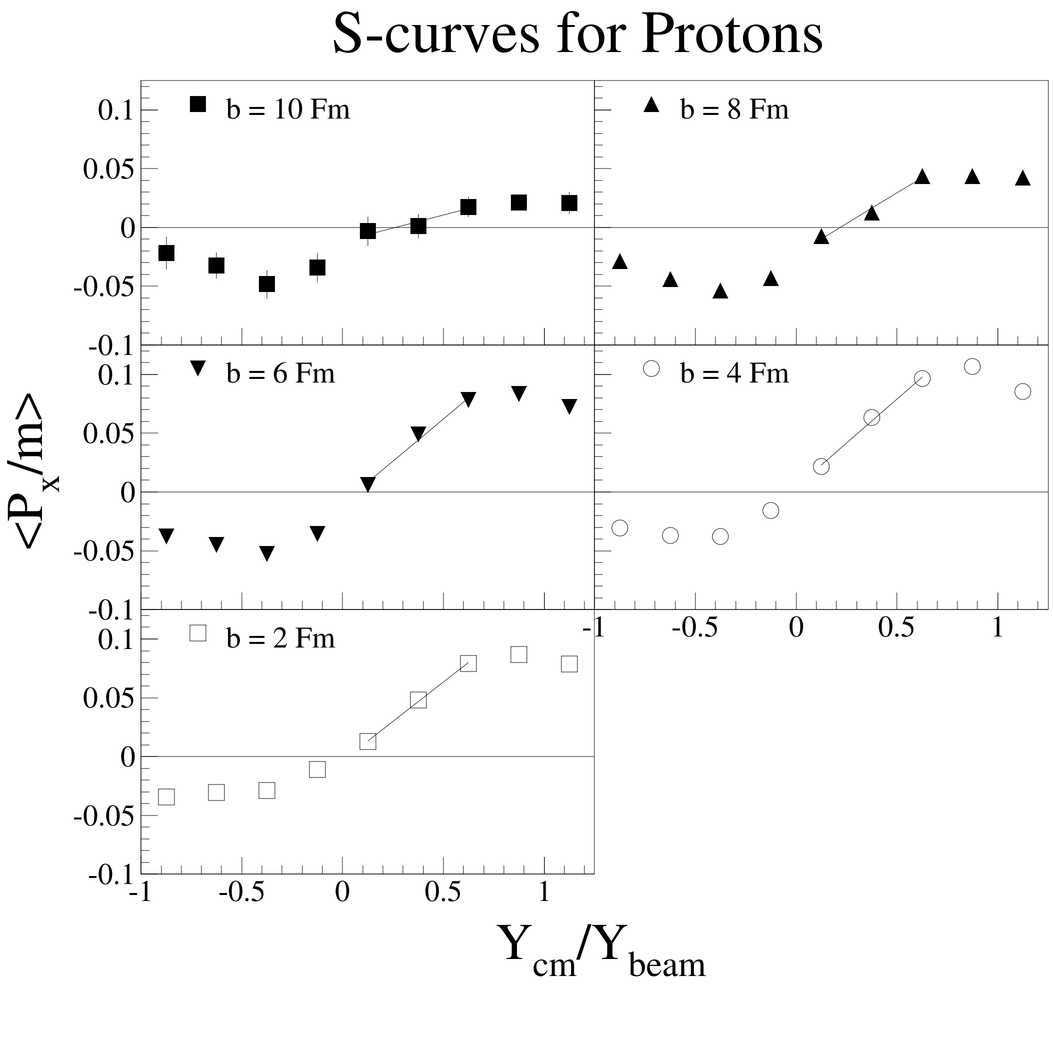

Figure 6.22: The S-curves for protons with the fits in the midrapidity region shown.

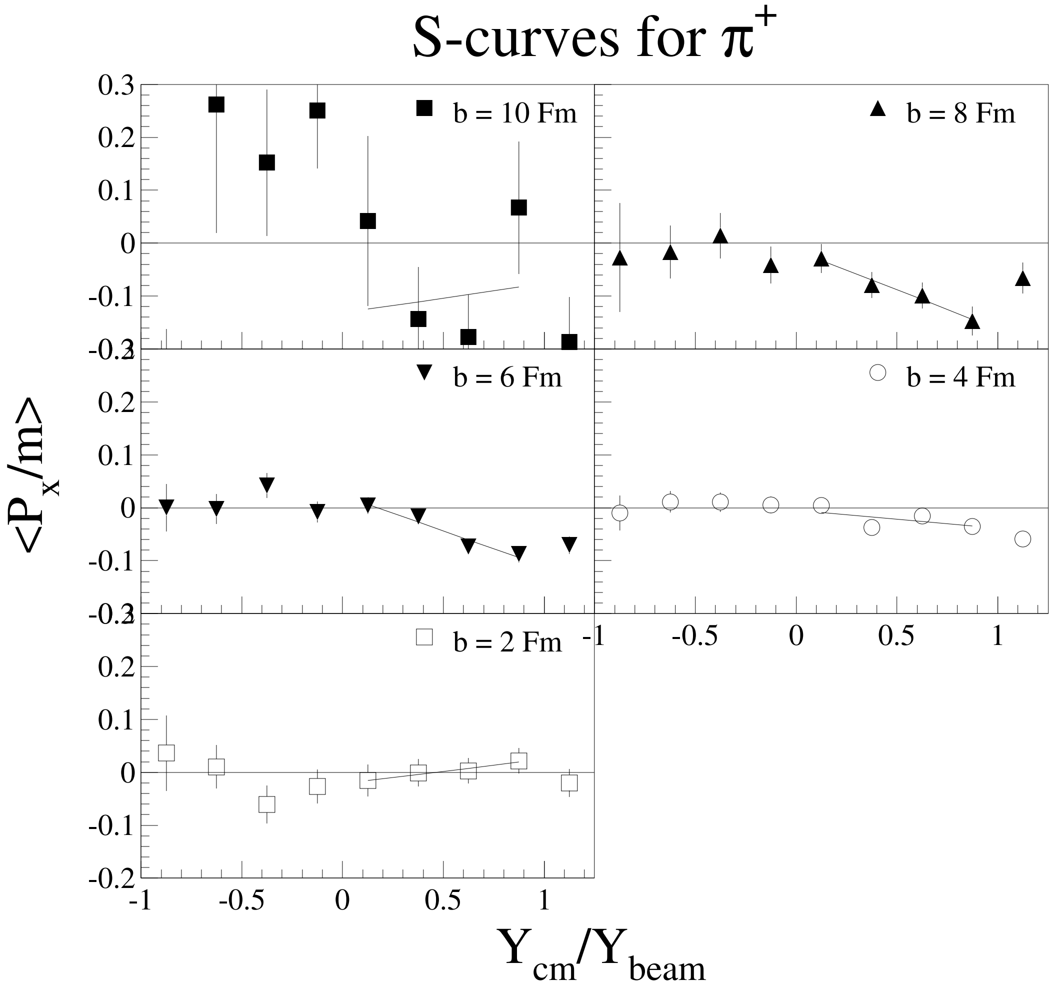

Figure 6.23: The S-curves for π^+ with the fits in the midrapidity region shown. Notice the pions have been fit in a slightly more forward region than the protons; this is to compensate for the acceptance as a function of rapidity.

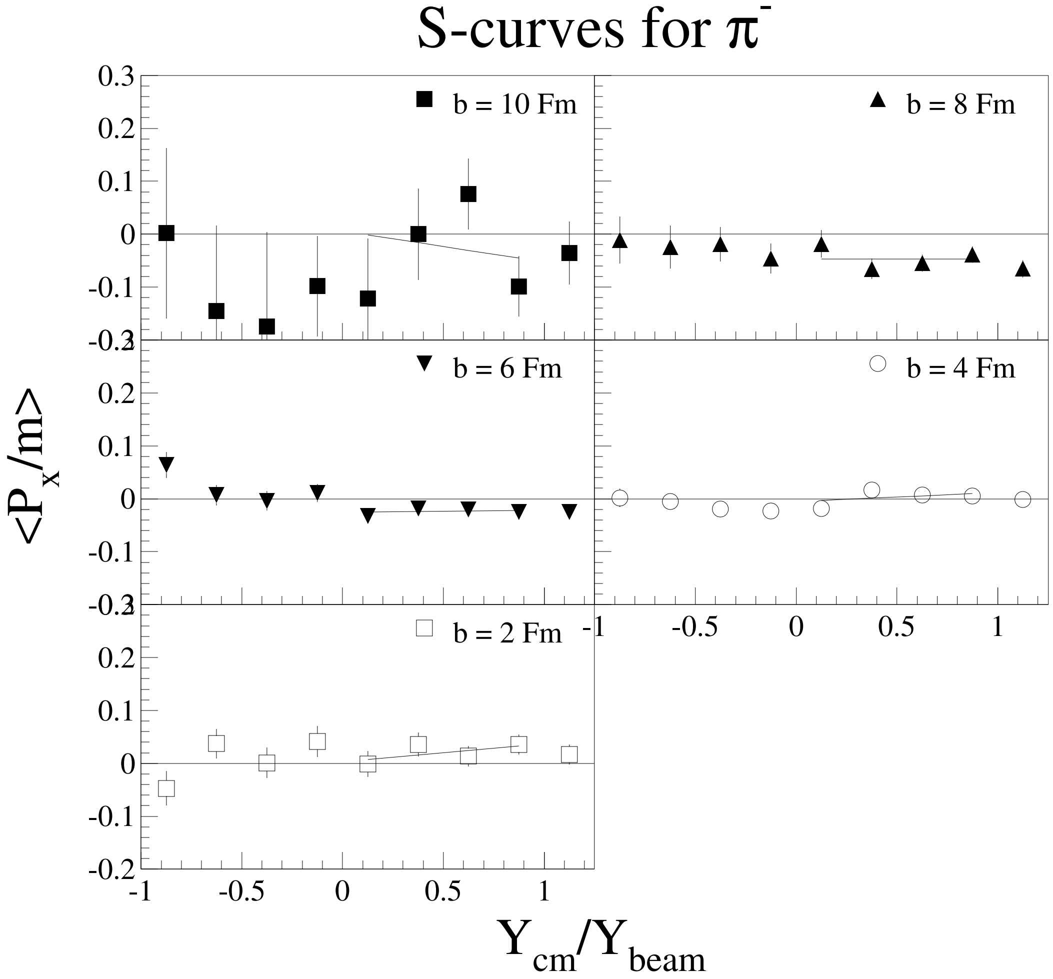

Figure 6.24: The S-curves for π^- with the fits in the midrapidity region shown.

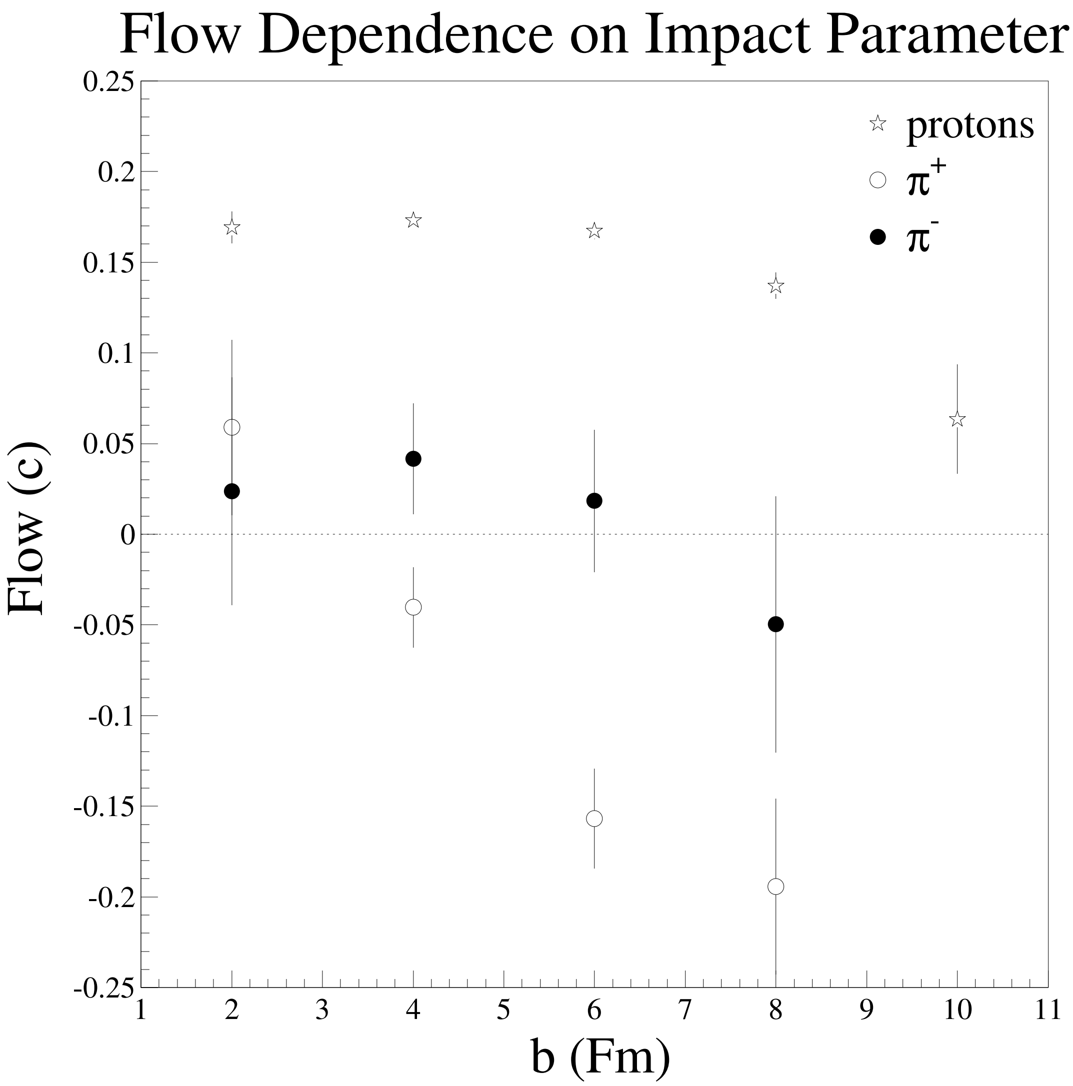

Figure 6.25: The extracted variable Flow as a function of impact parameter. A clear flow signature is observed for the protons, clear anti-flow is observed for the π^+, and there appears to be no flow for the π^-.

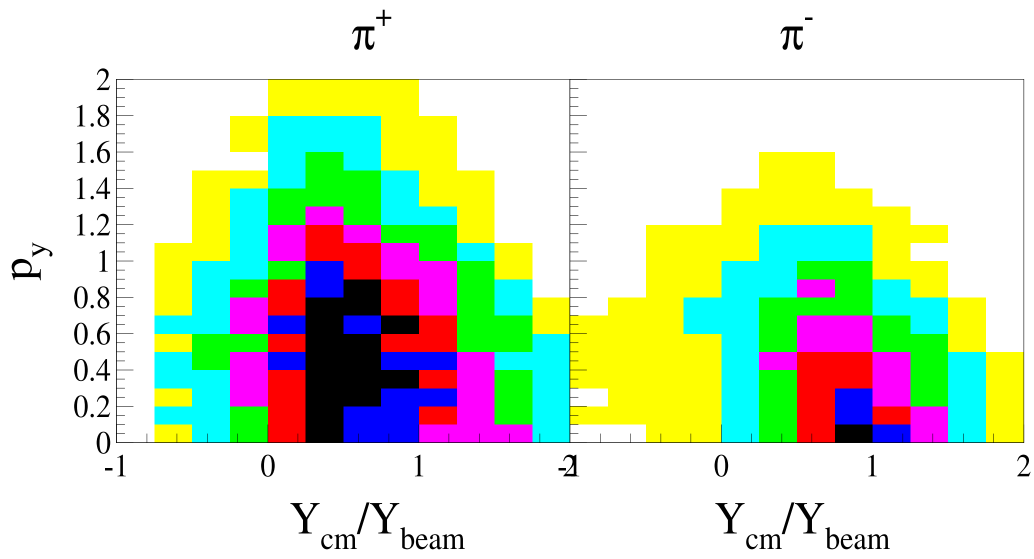

Figure 6.26: Yield of pions as a function of p_y and rapidity. There is a dramatic difference in location of the peak for π^+ and π^-.

It is possible that looking at p_y distributions will reveal something about the Coulomb interaction. If there is a noticeable Coulomb kick, it should also be felt by the pions in the y-direction. There should be no flow in the y-direction since everything is already rotated into the reaction plane, although that is the direction for squeeze-out. The p_y distribution of π^+ and π^- is shown in Figure 6.26. There is a cut on events with impact parameter around 4 Fm in this figure, and the absolute value of p_y is used since p_y is symmetric around zero (no flow). There is indeed a difference between the two species; however, it is not at all straightforward to interpret exactly what the difference means. The π^+ have a distribution that is peaked around $p_y = 0.4\, GeV/c$ and $Y_{cm}/Y_{beam} = 0.5$. The π^- show strong peaking around $p_y = 0\ GeV/c$ and $Y_{cm}/Y_{beam} = 0.75$. This is consistent with the Coulomb picture. The π^+ are kicked away from the spectators, which is indicated by the higher p_y, and the π^- are pulled in, which is indicated by p_y of nearly zero. However, it is necessary to use caution since these pictures have not been corrected for the detector acceptances. Figures 4.2 and 4.3 show that the pion acceptance is quite good for $Y_{cm}/Y_{beam} > 0.3$. In this region alone, there is still a difference in the p_y spectra for π^- and π^+.

In order to more qualitatively understand the Coulomb effect, a simple simulation was run. The pions were assumed to be isotropically distributed in a sphere of radius $b/2$. Only one quarter of the sphere was actually used, since one can understand the other pieces by symmetry arguments. The quarter corresponding to forward going pions on the positive side of the reaction plane was used. The positive and negative sides of the reaction plane should be exactly the same. And forward going pions should behave exactly as negative going pions with a change in sign. They were assumed to start at rest since the only thing of interest here is the change in pion momentum due to the Coulomb effect. The charge of each spectator was estimated as half the charge left over from the multiplicity corresponding to the number of protons in the overlap region of the simple model used in determining the impact parameter in Chapter 5. The simulation was started when the spectators were at their moment of closest approach and continued until each had traveled 25 Fm. The results of this simple method are shown in Tables 6.8 and 6.9.

$b(\ Fm)$	$p_x\ (MeV/c)$	$p_y\ (MeV/c)$	$p_z\ (MeV/c)$
2	-18.86	22.61	3.20
4	-25.34	30.73	6.24
6	-27.40	33.34	8.05
8	-26.30	35.92	7.31
10	-24.64	33.60	7.31

Table 6.8: Estimates of the average Coulomb kick for the x, y, z components of momentum for π^+.

$b(\ Fm)$	$p_x\ (MeV/c)$	$p_y\ (MeV/c)$	$p_z\ (MeV/c)$
2	10.59	-12.18	-1.50
4	13.27	-15.78	-1.67
6	14.57	-17.51	-1.74
8	15.39	-18.40	-1.92
10	15.55	-18.27	-2.36

Table 6.9: Estimates of the average Coulomb kick for the x, y, z components of momentum for π^-.

These results certainly show that the Coulomb force has an effect on the distribution of pions. The x component of the kick for π^+ is always negative, which is in the direction of anti-flow. The x component of the kick for π^- is always positive, which is in the direction of the flow. Similarly, the π^+ get a p_y kick out of plane, and the π^- get pulled in. This is all consistent with the results observed so far. However, the magnitude of the p_y kick is an order of magnitude smaller than the observed difference for the 4 *Fm* example as shown in Figure 6.26. And the Coulomb effect alone seems to indicate that the π^- ought to show positive flow because of their attraction toward the protons. However, the magnitude of the p_x kick is consistent with the anti-flow results for π^+. This simple model suggests that although the Coulomb effect is important, it does not explain the signal completely.

There is a large asymmetry in the number of neutrons and protons in the $^{197}_{79}$Au nucleus. In this energy range, the π^+ have a higher cross section than π^- for interactions with protons, and the π^- have a higher cross section than π^+ for interactions with neutrons. A simple calculation of relative kinetic energy of π^+ on proton yielded an average value of $80\,MeV$ for the pion. The calculation used a Boltzmann distribution of π^+ ($T = 55\,MeV$) and protons ($T = 90\,MeV$) in the interaction region. The temperatures for the pion and proton distributions were taken from data published by the FOPI Collaboration [Trza94]. Figure 1.8 shows that $80\,MeV$ is on the leading edge of the first Δ resonance, but that the cross section for π^+p is already about double the cross section for π^-p. Experiments by the LAND group at GSI [Leif93] have indicated that the neutrons exhibit the same flow characteristics as the protons; so in essence, because gold has a large asymmetry between neutron and proton number, the π^- 'see' a shadowing nuclear remnant about 1.5 times larger than the π^+.

But exactly what should one expect to observe due to this larger shadowing? Bass, et al. [Bass93, Bass93b] argue that the squeeze-out and flow are caused by pion absorption and scattering, respectively. This will be discussed in more detail in Chapter 7.

Chapter 7

Comparison to Theory

7.1 Overview of Available Models

It is hoped that the observations of collective effects can be explained in terms of a theory that starts with the fundamental interactions. Such a complete description of relativistic heavy ion collisions would take into account in a consistent way density and momentum dependent forces in addition to relativistic effects. Models which attempt such a detailed description have become very powerful and very complex. The available models of relativistic nucleus-nucleus collisions are of several types with varying levels of complexity:

1. Purely Statistical Models [Stoc86]

   Require no knowledge of the basic interactions. Examples are:

   (a) Fireball model [West76, Goss77]

(b) Multiple fireball models [DasG79]

(c) The firestreak model [Myer78]

(d) Row-on-Row model [Hufn77]

(e) Evaporation model [Lync83]

2. Microscopic Models [Bert88]

   (a) Intranuclear Cascade (INC)

   This model contains two body interactions but no mean field or Pauli blocking. It was the first microscopic model. Historically, Serber is given credit for the earliest version [Serb47].

   The Cascade model treats the N-N collisions in a fully microscopic way. It was the first microscopic model compared to experimental data [Cugn81].

   Each nucleus consists of a collection of point nucleons distributed within a sphere. No Fermi momenta are assigned. The nucleon position is assigned by Monte Carlo.

   Some Cascade models include potentials [Yari79, Uehl33].

   (b) Quantum Molecular Dynamics (QMD) [Aich86]

   This model includes two and three body Skyrme interactions as well as Yukawa and Coulomb terms. Momentum dependent interactions can be used. The IQMD model has added isospin [Bass95].

(c) Transport Models (VUU and BUU) [Bert84]

BUU uses a Boltzmann transport equation with scattering terms and mean field. Some versions include momentum dependent interactions. The BUU model can be viewed as an extension of the Cascade model to include the mean field and Pauli blocking. Bauer's version treats mesonic degrees of freedom explicitly [Li91].

All of the above mentioned models reproduce some pieces of the experimental data. But several discrepancies also exist which suggest which models to use. In this work, the pion squeeze-out will be compared to the IQMD model of Bass, et al. [Bass95], and the pion flow will be compared to Bauer and Li's BUU model [Li91].

A first test of the two models involves checking how well they reproduce the observed pion multiplicities as a function of impact parameter. The EOS TPC pion multiplicities are shown in Figure 7.1 along with the BUU and IQMD model predictions. The EOS data has been corrected in the following way: the rapidity distribution for each impact parameter quoted was symmetrized around $Y_{cm}/Y_{beam} = 0$. Then one can calculate how many particles were lost because of the backward going detector acceptance problem by dividing the number in the raw spectrum by the number in the symmetrized spectrum. As Figure 7.1 shows, the EOS data agree rather well with these theoretical predictions. Note the scale change between the top panel which shows π^+ and the bottom panel which shows π^-. There are more π^- because, as mentioned previously, there are more neutrons than protons in the Au nucleus, and

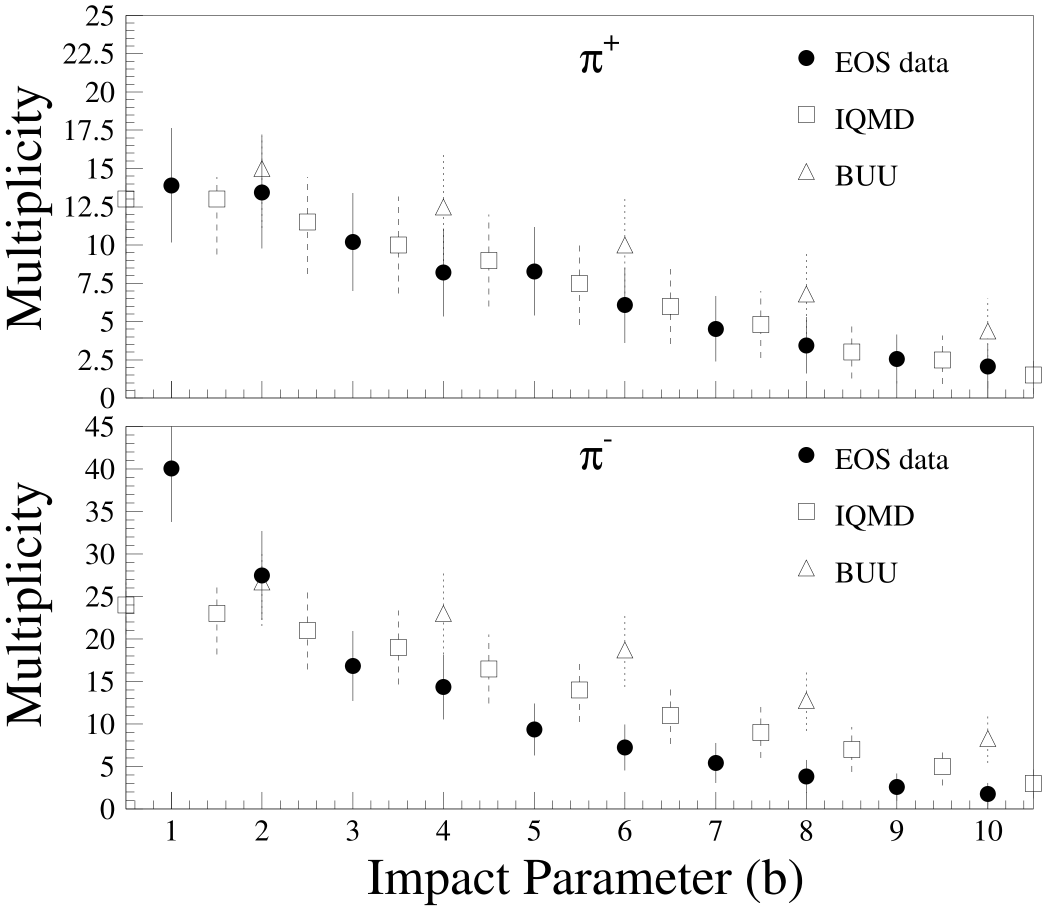

Figure 7.1: Pion multiplicities as a function of impact parameter for both species of pions compared to two models: BUU and IQMD. The top panel shows the π^+, and the bottom panel shows the π^-. Good agreement is seen between the models and the EOS TPC data.

π^- have a higher cross section for interaction with neutrons than protons.

Recall from the discussion in Section 1.6, a $\pi^-:\pi^+$ ratio of $1.87:1$ is expected from pion production cross sections alone. One can get an estimate of this ratio in the EOS data by summing over the impact parameter bins weighted by $b\,db$ in Figure 7.1. The $\sum$ counts $b\,db \approx 441$ for π^- and 301 for π^+. This results in a $\pi^-:\pi^+$ ratio of about $1.5:1$. This is slightly lower than the predicted ratio. That is not too surprising, however, since following similar arguments about the greater number of neutrons than protons, one expects the π^- to have a greater probability for absorption by neutrons. Making similar calculations for the models, the IQMD model predicts a ratio of $632.5:330.6$, or $1.9:1$, and the BUU model predicts a ratio $393.2:238.4$, or $1.6:1$.

7.2 The Boltzmann-Uehling-Uhlenbeck Model

Historically, the excitation function of pion multiplicity was thought to be a good probe of the nuclear equation of state [Stoc86]. There was a discrepancy between the data and the intranuclear cascade model, because this model does not include compression effects. More elaborate models, like BUU and QMD find the sensitivity of the nuclear equation of state to pion multiplicity not so obvious—especially when momentum dependent forces are taken into account. The predictions of these models suggest the need to look at other pion properties, such as pion spectra, flow, and squeeze-out.

DIOGENE shows non-zero pionic flow, but the cascade model to which the authors compare shows no flow [Goss89]. It is generally stated that cascade models do not produce flow, but recently Kahana, et al. [Kaha95] have shown that an intranuclear cascade model (ARC) without a mean field does produce flow. The authors compare to EOS data and come close to reproducing the nucleon flow at EOS energies. The QMD model does predict non-zero flow, but less than the experimental data [Hart88].

The pion energy spectra have been a subject of great interest because of the concave shape requiring two slopes, or two temperatures, to fit the experimental data. The cascade model predicts a purely thermal pion spectra [Broc84]. The total number of pions observed in the final stage is $\approx 30\%$ less than cascade predicts. Cugnon and Lemaire [Cugn88] have shown that it was necessary to multiply absorption reactions in the cascade model by 3 to fit the data. The authors explain this as an enhancement of pion reabsorption in the nuclear medium and an underestimation of pion reabsorption in their model. Using a BUU transport model calculation, this explanation is not necessary, and the total pion cross sections are in good agreement with data [Li91].

Thus, based on comparisons with various pion experimental data, the BUU seems to most closely reproduce the observed multiplicities as a function of beam energy, preliminary flow results, and energy spectra. Thus, our new pion flow results will be compared to this model. The code used for this work was provided by Wolfgang Bauer, but any mistakes in running it are this author's.

There are two main ways the BUU improves over the intranuclear Cascade model:

the introduction of a mean field and the inclusion of Pauli Blocking. A simple prescription for a mean field is to assign momenta up to the Fermi radius p_F. The mean field U, such as the Skyrme Parameterization (Equation 1.2) keeps the nucleus together. The radii R and p_F are not independent. They obey the relationship $4(4\pi/3)^2 R_3 p_F^3 = h^3 N$.

In order to test the Pauli blocking, consider two test particles. When two test particles collide they change from $(r_1, p_1), (r_2, p_2)$ to $(r_1, p_1'), (r_2, p_2')$. If the phase spaces around (r_1, p_1') and (r_2, p_2') are essentially empty then scattering is allowed. If on the other hand they are full, scattering is suppressed.

One can build a sphere of radius r around r_1 and radius p around p_1' such that n test particles in the phase space volume imply complete filling. A reasonable value for n is 8. Specifying n still does not fix r or p individually. The authors use $r/p = R/p_F$ where p_F is the Fermi momentum and R is the radius of the static nucleus.

One defines $f_1 = n_1/(n-1)$ where n_1 is the number of test particles in the phase space volume not including the test particle at (r_1, p_1'). Similarly $f_2 = n_2/(n-1)$. The probability of scattering is taken to be $(1-f_1)(1-f_2)$ and this is Monte Carlo'ed in the usual way.

The preceeding method was described by Bertsch and Das Gupta [Bert88] to solve the BUU equation:

$$\frac{\partial f}{\partial t} + \boldsymbol{v} \cdot \boldsymbol{\nabla}_r f - \boldsymbol{\nabla}_r U \cdot \boldsymbol{\nabla}_p f =$$

$$
\begin{aligned}
&-\frac{1}{(2\pi)^6}\int d^3p_2 d^3p_2 d\Omega \frac{d\sigma}{d\Omega} v_{12} \\
&\times\{[ff_2(1-f_{1'})(1-f_{2'}) - f_{1'}f_{2'}(1-f)(1-f_{2'})] \\
&\times(2\pi)^3\delta^3(\boldsymbol{p}+\boldsymbol{p}_2-\boldsymbol{p}_{1'}-\boldsymbol{p}_{2'})\}
\end{aligned} \tag{7.1}
$$

The right-hand side of the BUU equation is the collision integral including the Pauli blocking. If the right-hand side of the BUU equation is set equal to zero, one obtains the Vlasov equation.

7.3 The IQMD Model

Although the BUU model has had success with single particle spectra and collective effects such as bounce-off, flow, stopping, and squeeze-out, certain fluctuations and correlations, such as fragment formation cannot be studied with a transport model based on a single particle distribution function. This was one of the main motivations for the development of the Quantum Molecular Dynamics Model (QMD) [Bass95].

In the QMD model, the baryons are represented by Gaussian shaped density distributions:

$$
f_i(\boldsymbol{r},\boldsymbol{p},t) = \frac{1}{\pi^2\hbar^2} e^{-(\boldsymbol{r}-\boldsymbol{r}_{i0}(t))^2\frac{1}{2L}} e^{-(\boldsymbol{p}-\boldsymbol{p}_{i0}(t))^2\frac{2L}{\hbar^2}} \tag{7.2}
$$

They are initialized in a sphere of a radius $R = 1.14A^{\frac{1}{3}}\ Fm$ in accord with the liquid drop model. Each nucleon occupies a volume of h^3, so that phase space is uniformly filled. The initial momenta are randomly chosen between 0 and the local Thomas-

Fermi momentum. The nucleons interact via two and three body Skyrme forces, a Yukawa potential, and momentum dependent interactions. In the IQMD model, isospin is treated explicitly. Pion production is treated via the Δ resonance. No direct pions ($NN \Rightarrow NN\pi$) were included.

The equation of state is a Skyrme type parameterization as in Equation 1.2:

$$U = \alpha(\rho/\rho_0) + \beta(\rho/\rho_0)^\sigma + \delta \cdot \ln^2(\epsilon \cdot (\Delta \boldsymbol{p})^2 + 1) \cdot (\rho/\rho_0) \tag{7.3}$$

As in the BUU calculation, the soft equation of state has a value for σ of 1.17, and the hard eos has a value of 2.0.

Pions are formed in the IQMD model via the decay of the Δ resonance. The following inelastic reactions are explicitly taken into account and constitute the imaginary part of the pion optical potential, which is dominant in the $1\,GeV/n$ range [Enge94]:

1. $NN \Rightarrow \Delta N$ (hard-delta-production)
2. $\Delta \Rightarrow N\pi$ (Δ-Decay)
3. $\Delta N \Rightarrow NN$ (Δ-Absorption)
4. $N\pi \Rightarrow \Delta$ (soft-delta-production)

Elastic $\pi - \pi$, $\pi - \Delta$, $\pi - N$, $\Delta - \Delta$, and $\Delta - N$ scattering are not taken into account. Experimental cross sections are used for the hard and soft delta production processes [VerW82]. For Δ absorption, a modified detailed balance formula was used [Dani91]. The conventional detailed balance formula is only correct for particles with infinite lifetimes (zero width). The conventional detailed balance relation for delta absorption is:

$$\sigma_{N\Delta \Rightarrow NN} = \frac{p^{*2}}{8p'^{*2}} \sigma_{NN \Rightarrow N\Delta} \tag{7.4}$$

Here p^* and p'^* are the center of mass momenta in the $N\Delta$ channel and in the NN channel respectively. Cross sections are averaged over the spin and isospin values in the initial state and summed over the final states. The variable resonance masses are selected from a Breit-Wigner distribution. However, the IQMD model uses the modified detailed balance formula was used [Dani91]:

$$\sigma_{N\Delta \Rightarrow NN} = \frac{\frac{1}{8}\frac{mp^{*2}}{p'^{*}}}{\int_{m_N+m_\pi}^{2e^*-m_N} \frac{dm''}{2\pi} m'' A_\Delta(m'') p''^{*}} \sigma_{NN \Rightarrow N\Delta} \tag{7.5}$$

Here p^* and p'^* are exactly as before and e^* is the nucleon center of mass energy. The cross sections for resonance absorption from Equation 7.5 are larger, on the average, than the cross sections in Equation 7.4. This is significant; if, for example, the Δ absorption cross section is underestimated by a factor of 2, the total number of Δ's and pions will be overestimated by approximately a factor of 2.

After a pion is produced (whether free or bound in a delta), it interacts with nucleons via two distinct processes:

1. Absorption — $\pi NN \Rightarrow \Delta N \Rightarrow NN$

2. Scattering — $\pi N \Rightarrow \Delta \Rightarrow \pi N$

In the IQMD model, pions propagate between collisions on curved trajectories with Coulomb forces acting upon them.

7.4 Comparison of Squeeze-Out Results

Although the BUU does not produce much squeeze-out of nucleons or pions (see Figure 7.2), the IQMD predictions of Bass, et al. [Bass95] show squeeze-out as a function of both transverse momentum and impact parameter.

Shown in Figure 7.3 are the results of the IQMD predictions and EOS TPC data for π^+ and π^-. This is really only a qualitative comparison. Bass, et al., point out in their paper that uncertainties in the experimental determination of the reaction plane make it difficult to compare the theory to the data. Also, the IQMD calculation shown here is actually for 1.0 GeV/n Au + Au. The rapidity region is different: the IQMD calculation was done for $-0.2 < Y_{cm}/Y_{beam} < 0.2$ and the EOS data for $0.2 < Y_{cm}/Y_{beam} < 0.8$

Shown in Figure 7.4 are the EOS TPC results compared to the KaoS spectrometer results [Bril93]. KaoS has only published results for π^+. The comparison here is much better, both EOS and KaoS have errors in the reaction plane determination of a similar order, and consistent forward rapidity cuts were used. The KaoS data is for 1.0 GeV/n Au + Au, but that should make a small difference. We agree quite well with the KaoS data. Although the EOS data slightly underlies the KaoS data, the shape and general trends are in good agreement.

Bass has also performed the IQMD calculations of the squeeze-out ratio as a function of impact parameter. Shown in Figure 7.5 is a comparison of the EOS TPC data for π^- (solid circles) to IQMD calculations for π^0 performed with a hard equation of

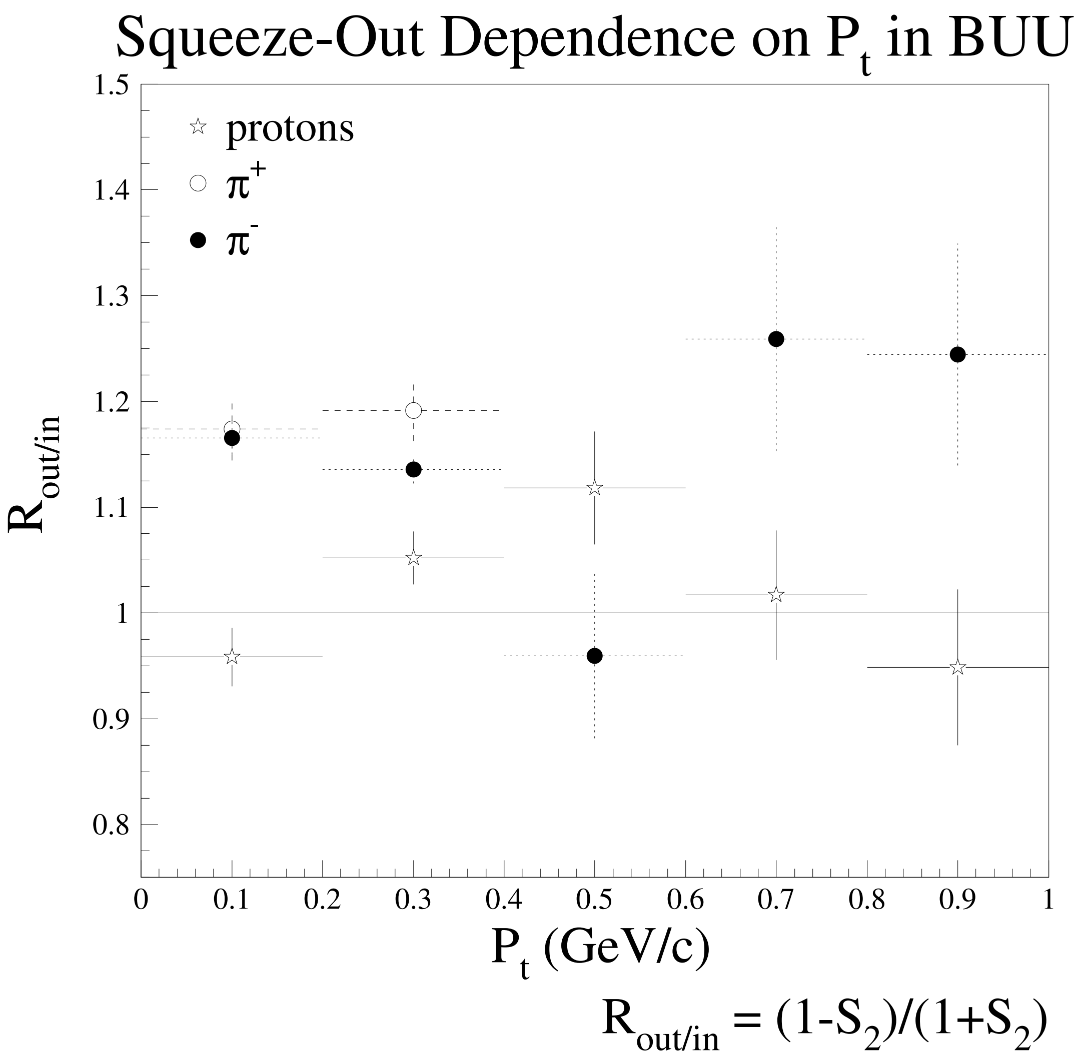

Figure 7.2: Squeeze-out ratio for particles produced in the BUU simulation. Although the protons and π^- show some squeeze-out, there are large errors and it is quite inconclusive.

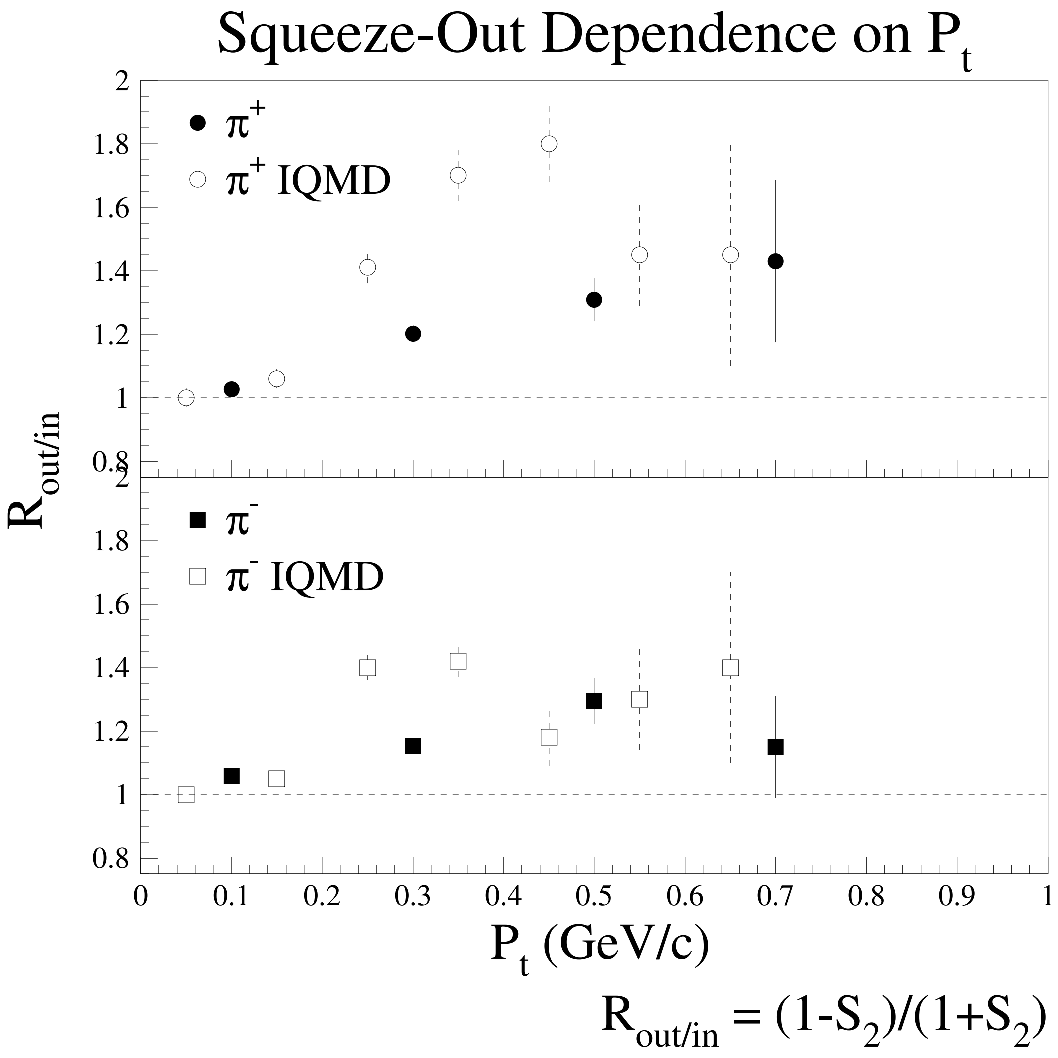

Figure 7.3: Comparison of extracted squeeze-out number ratios, $R_{out/in}$ with the IQMD calculations published by Bass, et al. Qualitative agreement is seen for pions.

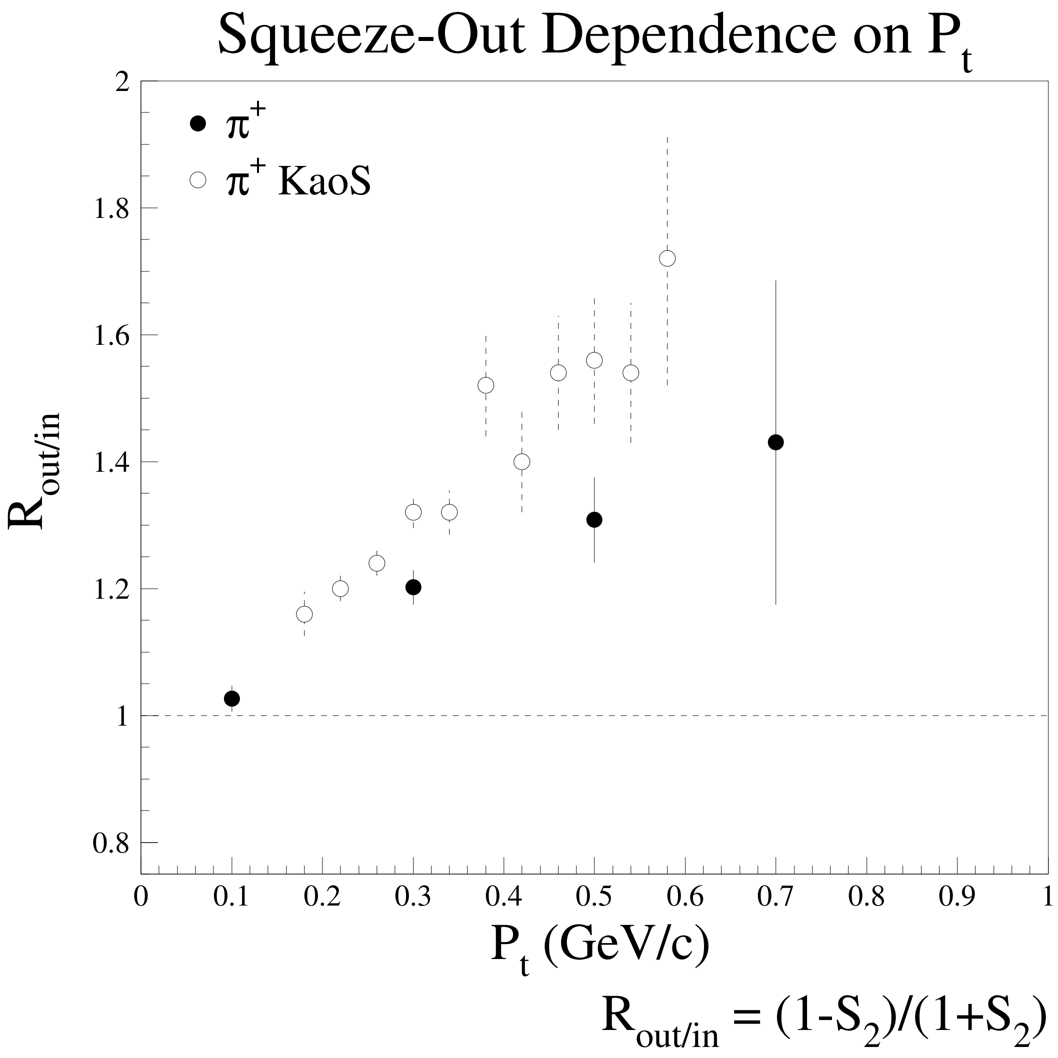

Figure 7.4: Comparison of extracted squeeze-out number ratios, $R_{out/in}$, of the EOS TPC data with KaoS data for forward going π^+ published by Brill, et al. Good agreement is seen in the shape and magnitude.

state with (open squares) and without (open circles) momentum dependent interactions (mdi). The comparison between π^- and π^0 is justified because we saw minimal difference in the π^+ π^- squeeze-out signal, so one might suspect the Coulomb force is not as important here. Although there are few EOS data points, the agreement in magnitude and shape is quite good for the IQMD calculation of a hard eos with no mdi. The EOS data falls off a bit more for the 10 Fm point, but for the other points the agreement is excellent—completely within the statistical error bars.

7.5 Comparison of the Flow Results to BUU

Here I will show the significant flow results compared to the BUU calculations. First, the switches used in running the code are described.

- The time evolution of the reaction was 50 Fm/c.
- The density cut off (density at which the particles are no longer assumed to interact) was 0.02 Fm^{-3}.
- There were no reductions for "in-medium" effects.
- Direct pions ($NN \Rightarrow NN\pi$) were not included.
- The Coulomb interaction was turned on.
- Cugnon cross sections were used.

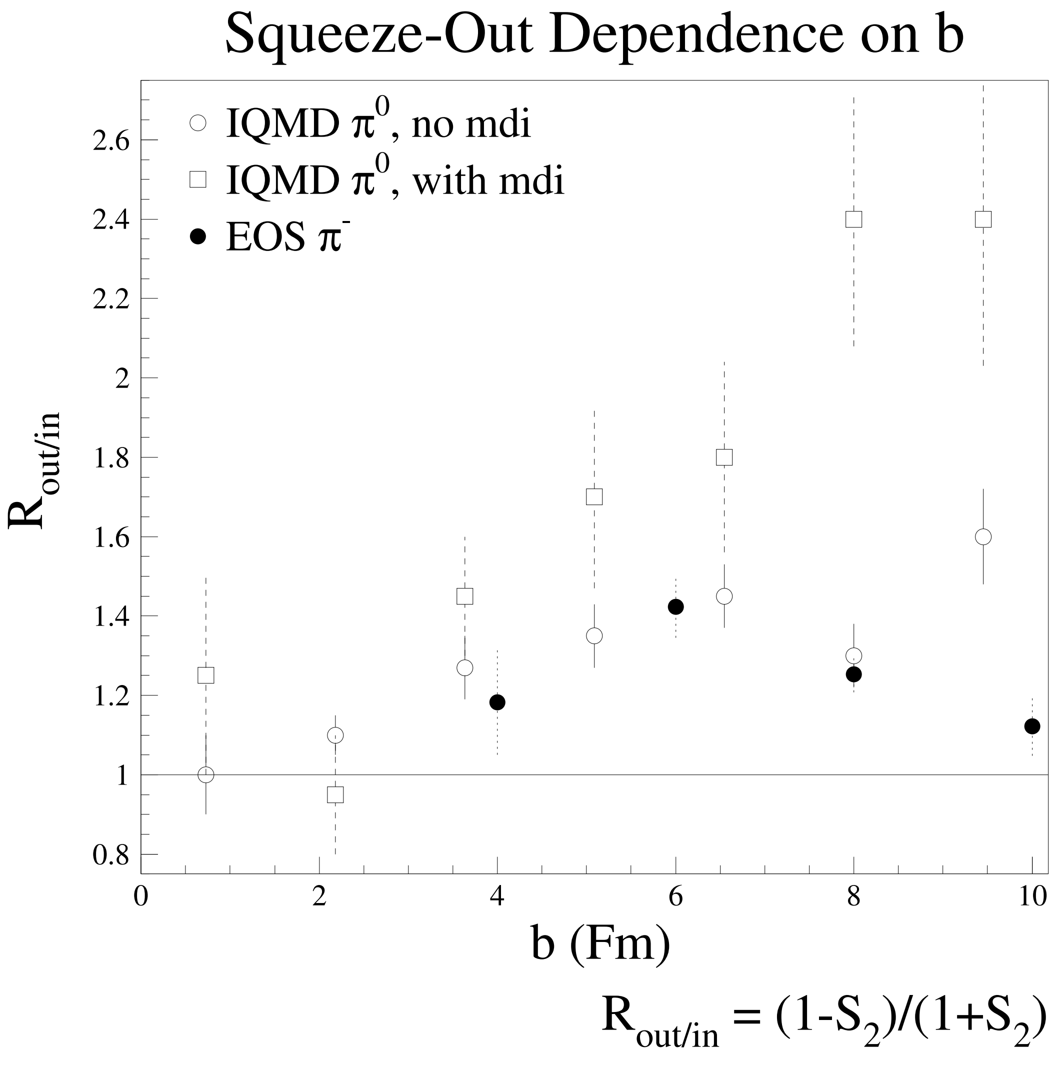

Figure 7.5: Comparison of extracted squeeze-out number ratios, $R_{out/in}$, as a function of impact parameter with the IQMD calculations published by Bass, et al. Excellent agreement is seen for EOS π^- (closed circles) and the IQMD hard eos with no momentum dependent interactions (open circles).

- 100 test particles were used.
- The code was run with soft and hard eos ($\sigma = 2$, $\sigma = 7/6$ respectively).
- Pauli-blocking was included.
- A Wood-Saxon potential was used.
- The density was spherical.
- Noncyclic boundary conditions were used.

EOS TPC experimental results are extremely well described by the BUU calculations, especially the pion flow results as a function of impact parameter. Figure 7.6 shows the comparisons of the impact parameter dependence of flow to the BUU calculations. The features of the proton flow which were qualitatively described in discussion of Figure 6.22 can be seen quantitatively in the top panel of Figure 7.6. Proton flow is always positive (by definition) and reaches a maximum value at an impact parameter of 4 Fm. The agreement with the flow values extracted from the BUU predictions is quite good; however, there is little differentiation between the soft and the hard equation of state.

The lower two panels of Figure 7.6 display the flow as a function of impact parameter for π^+ and π^-. For peripheral collisions ($b \geq 8\,Fm$), both π^+ and π^- display the anti-flow trait that was predicted by Bass, et al. [Bass95]; however, the magnitude of the anti-flow signal is much greater for the π^+ than for the π^-, which was not evident

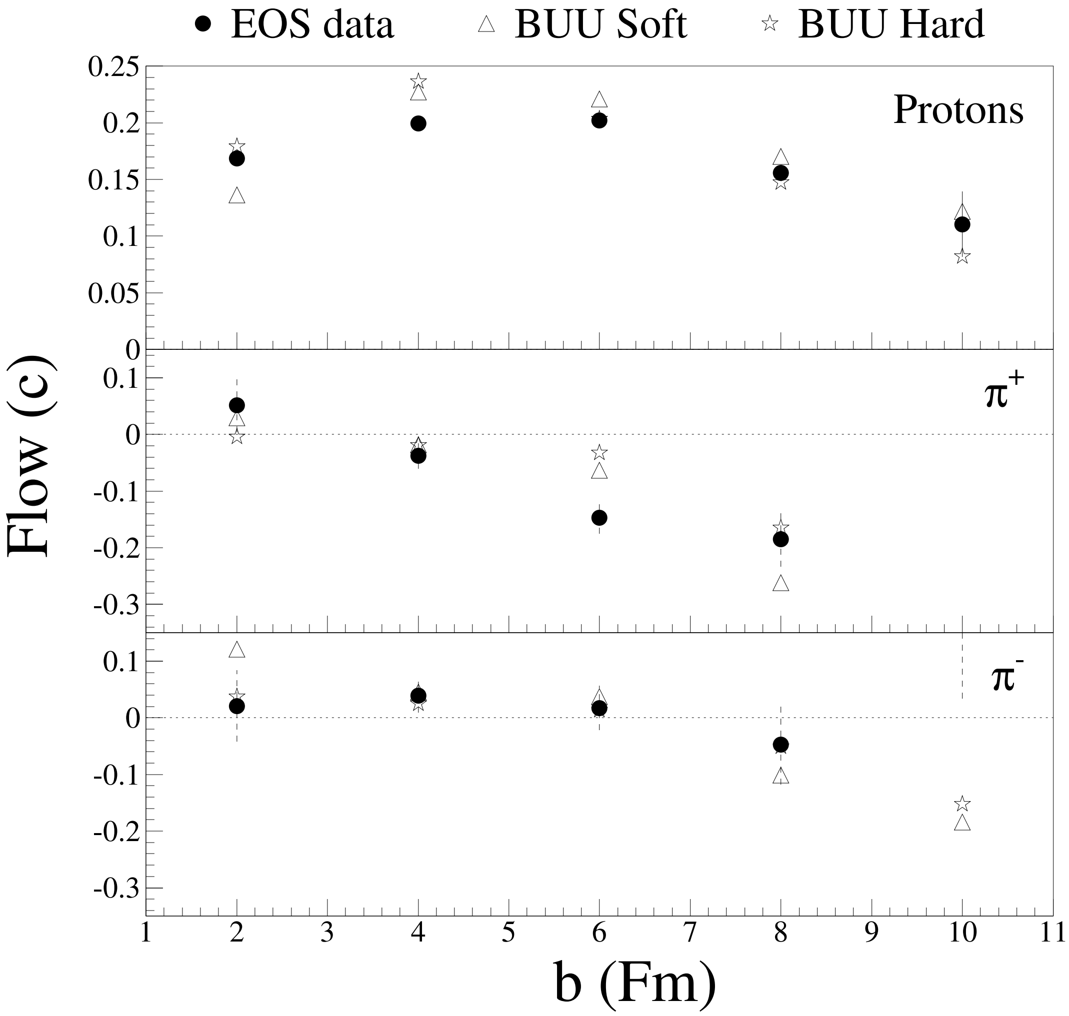

Figure 7.6: Comparison of extracted flow parameters with the BUU calculations. Good agreement is seen for protons, and excellent agreement is observed for pions.

in the IQMD predictions of Bass. There is a reduction in the magnitude of the flow signal with centrality for pions, and a slight but not statistically significant positive pion flow for the most central events. The peripheral events have massive baryonic spectators, which absorb or reflect pions emitted in their direction. The reduction in flow signal with centrality is possibly explained as a reduction in the size of the remnant.

The π^+ exhibit a clear anti-flow behavior that diminishes with impact parameter, while the π^- seem to be best described as exhibiting almost no flow regardless of impact parameter. This difference in behavior does not seem to be an artifact of the detector acceptance for two reasons. First, we have attempted to remove any differential detector biases from our data, and second, the same behavior is exhibited in the BUU simulations which have not been modified to simulate acceptance biases.

7.6 Discussion

There is a large asymmetry in the number of neutrons and protons in the $^{197}_{79}$Au nucleus. The π^+ have a higher cross section for interactions with protons, and the π^- have a higher cross section for interactions with neutrons. Experiments by the LAND group at GSI [Leif93] have indicated that the neutrons exhibit the same flow characteristics as the protons; so in essence, because gold has a large asymmetry between neutron and proton number, the π^- 'see' a shadowing nuclear remnant about 1.5 times larger than the π^+.

But exactly what should one expect to observe due to this larger shadowing? The larger cross-section means a higher probability of scattering or absorption of the π^- by a neutron. So, perhaps the question can be answered by results of previous squeeze-out analysis. Bass, et al. [Bass93b] have studied the effects of various pion interactions. They have found that when the reaction $\Delta N \Rightarrow NN$ is turned off in the IQMD model the squeeze-out disappears. When they suppressed absorption in this way, no anisotropy was observed. Therefore, they conclude that the anisotropy in pion emission is dominated by the pion *absorption* process.

If we assume that the pion absorption process is dominant, it is difficult to explain the new pion flow results presented here. If this were the case, the π^- should show more anti-flow due to the larger cross-section for interaction with neutrons (there are more neutrons). On the other hand, using similar arguments and comparing to DIOGENE results, Bass, et al. [Bass93] find that pion *scattering* dominates the pion flow results. Even so, one can only assume that since the π^- have more neutrons to interact with than the π^+ have protons, either effect would be exaggerated. Perhaps π^+ and π^- have different probabilities of being scattered or absorbed.

Another possibility mentioned in the previous chapter is the effect of the Coulomb force. The difference between the two species of pions has been studied with the BUU by turning off the Coulomb term, and no noticeable difference is observed in any of the π^+, π^-, or π^0 curves, with or without the Coulomb term. Although the BUU model does include the Coulomb interactions between each of the protons involved, it does not coalesce these protons into large spectators. One can imagine that allowing the protons to spread out is not the same as if the protons were coalesced into large spectators. However, it seems to indicate that the Coulomb force cannot account for the entire difference.

Another thing to consider is the importance of the Δ resonance. Not only do the π^- have a greater chance of interacting since there are more neutrons, they have a better chance of being focused along the Δ flow. Although Δ flow has not yet been studied at EOS, it has been suggested that this could be significant [Bass93b]. The π^- have a larger chance of being correlated with the neutron into which the Δ decays. Thus, the π^- may be emitted more towards the neutron (nucleon) flow. This seems a possible explanation for the noted difference between the π^+ and π^- signals.

In summary, the pions are produced in a participant volume which is like a prolate spheroid along the flow axis. They scatter and are absorbed as they try to escape. It is easier to get out the sides of the spheroid since there is less matter in the way. This tends to produce the squeeze-out and anti-flow signals. This is one factor; however, there is also the positive Δ flow which tends to carry the pions along, with the π^- more strongly correlated than the π^+. One must also consider the Coulomb force, which tends to push the π^+ away from the nucleon flow and pull the π^- in toward the nucleon flow.

There are several open questions which must be addressed in the future. How important are momentum dependent interactions? What is the effect of the Coulomb interaction? Do scattering and absorption account for the flow and squeeze-out? What is the impact of the Δ behavior?

Chapter 8

Conclusions

8.1 Summary

In this thesis, the first results showing pion collective effects from the final generation of relativistic heavy ion experiments at the Bevalac have been presented. The experimental method was described, the data reduction process presented, the analysis method leading up to the final results explained, choice of theory was discussed, and finally, the results were compared to the IQMD and BUU transport model predictions.

Pion squeeze-out and flow have been studied as functions of transverse momentum and impact parameter in a heavy, symmetric system (Au + Au) at 1.15 GeV/nucleon. A clear pion squeeze-out signal was observed as a function of transverse momentum and impact parameter. Qualitative agreement was good with an IQMD model calculation. These new results support previous observations which suggested a linear increase in squeeze-out as a function of transverse momentum. It is observed that the squeeze-out for protons and pions has a peak near 6 Fm, which is slightly less central than the flow peak.

The first "S-curves," the standard signature of flow, have been presented as a function of impact parameter. Previous observations had seen preferential emission of pions away from the heavy target remnant in asymmetric collisions. These new EOS TPC results indicate that both the π^+ and π^- exhibit anti-flow for peripheral collisions, and that this becomes positive flow or no flow for the most central collisions. These observations support theoretical predictions of Bass, et al. [Bass95], who have suggested that such features could be generated by interactions between created pions and nucleonic matter; however, the differences between the behavior of the π^+ and the π^- suggest that further consideration of this phenomenon is needed. The BUU calculations reproduce the pion flow results in magnitude, sign and trend. At this energy, there seems to be little difference between BUU model calculations using a hard equation of state and those using a soft equation of state.

8.2 The Equation of State

There are no direct observables which one can use, such as placing a thermometer into the participant region of the relativistic heavy ion collision. Therefore, careful comparison to models is necessary to make some claim about the nuclear equation of state. This is not straightforward, as different models describe different subsets of the data well.

The pion flow results show good agreement with the BUU model, but no particular sensitivity to the equation of state. The pion squeeze-out results show good agreement with IQMD calculations done for a hard eos and no momentum dependence. These are pieces in a very complex and growing data set. The results shown here will need to be assimilated into a large existing set of experimental evidence probing the stiffness of the equation of state.

8.3 Future Work

There is much exciting work yet to be done to get a clear understanding of the nuclear equation of state. The implications for the EOS experiment are many. There are more systems and energies in which to study all the same things presented in this thesis. A study of the mass and energy dependence of pionic flow and squeeze-out will prove quite interesting. Of the EOS Au + Au data set, approximately 10% of the available data have been analyzed.

To further study the energy dependence of the flow, the EOS TPC has been moved to the AGS. This will allow measurements to continue up to the 10 GeV/n energy range.

There are new models coming into existence. A particularly promising idea is a comparison to the next generation of BUU model calculations which include a momentum dependent interaction. Perhaps this new BUU model will better predict the pion squeeze-out. The question of momentum dependence influencing the apparent stiffness of the nuclear equation of state must also be addressed.

This is to some extent work still in progress: a contribution to the understanding of the nuclear equation of state.

Appendix A

Squeeze-out Projections — Transverse Momentum

Shown in this Appendix are projections from Figures 6.1, 6.3, and 6.5. The 2 dimensional figures were plotted as functions of normalized rapidity (Y_{cm}/Y_{beam}) and azimuthal angle (ϕ_{RP}). There were 9 of these plots for protons and 4 for the pions, one plot for each transverse momentum bin. The projections shown in this appendix have been sliced in rapidity, then projected onto the ϕ axis for each transverse momentum cut.

Each figure is labeled at the top with the particle identification, at the bottom with the transverse momentum cut, and at the top of each panel with the rapidity slice. The protons are shown for a midrapidity region while the pions are all forward going. The fourth panel ($0 < NY_{cm} < 0.2$) of each page of proton plots corresponds to a panel in Figure 6.7. For the pions, the second, third, and fourth panels of each figure added together correspond to the panels shown in Figures 6.8 and 6.9.

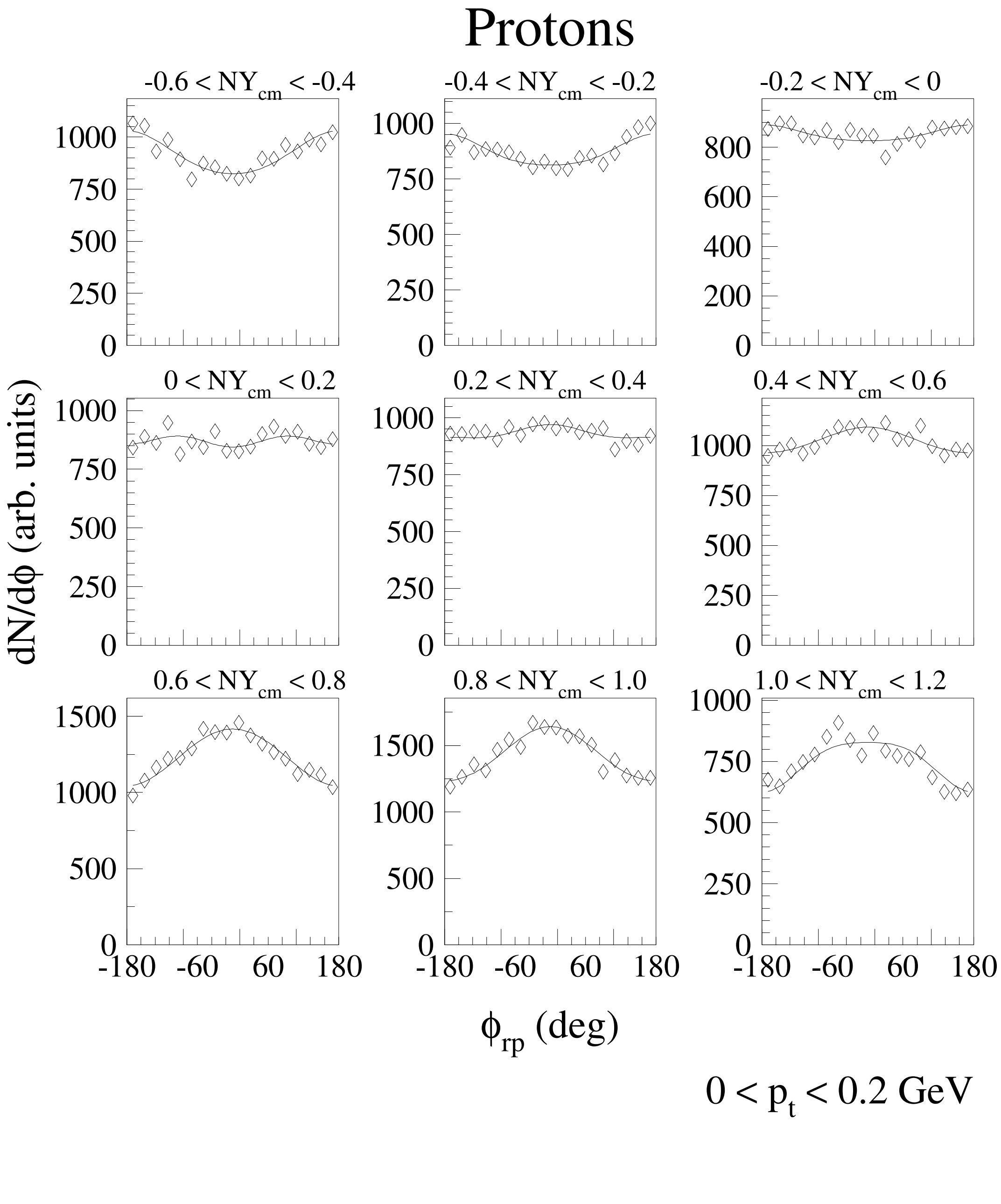
Protons
-0.6 < NY_cm < -0.4
-0.4 < NY_cm < -0.2
-0.2 < NY_cm < 0
0 < NY_cm < 0.2
0.2 < NY_cm < 0.4
0.4 < NY_cm < 0.6
0.6 < NY_cm < 0.8
0.8 < NY_cm < 1.0
1.0 < NY_cm < 1.2
dN/dϕ (arb. units)
ϕ_rp (deg)
0 < p_t < 0.2 GeV

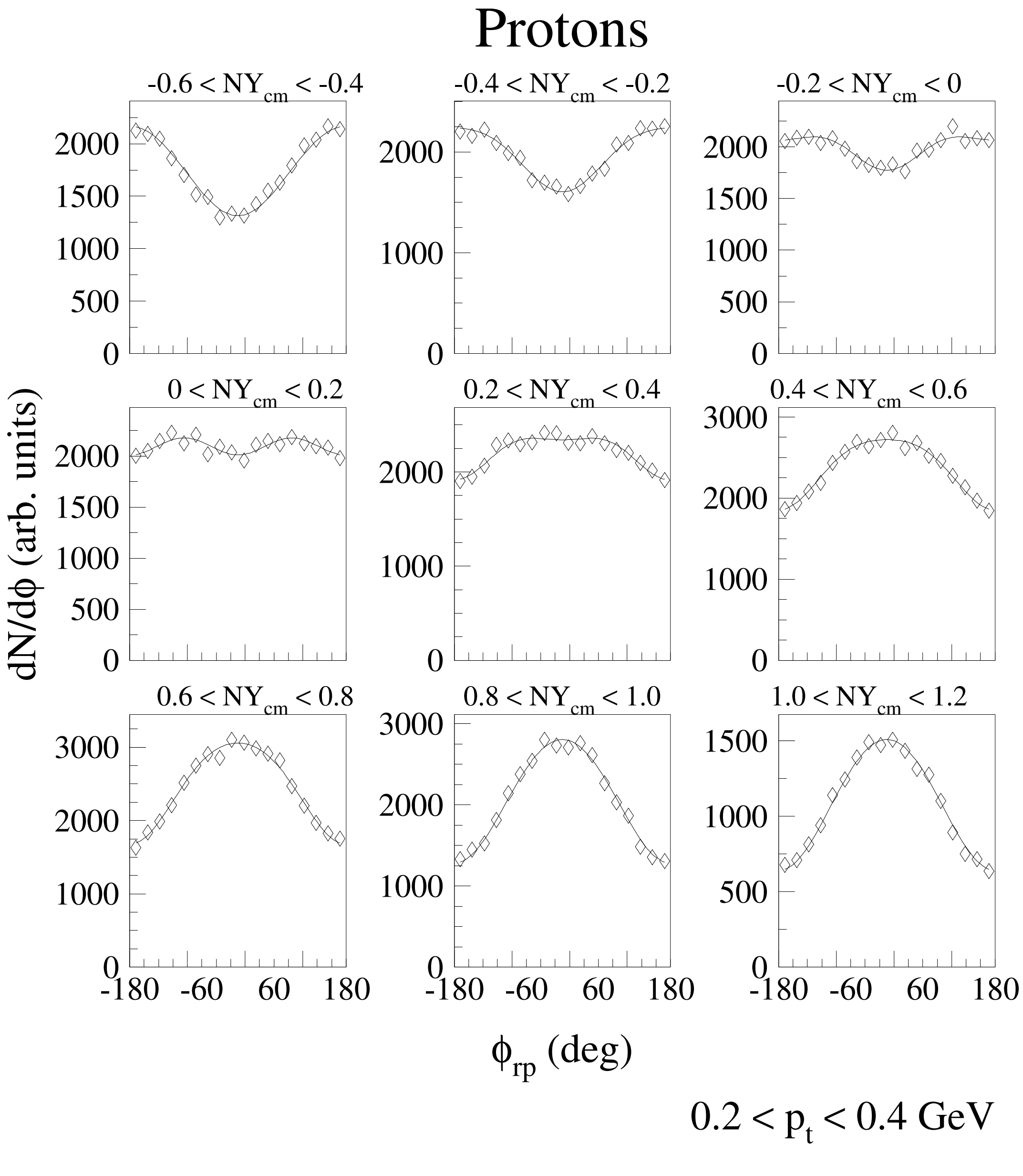
Protons
-0.6 < NY_cm < -0.4
-0.4 < NY_cm < -0.2
-0.2 < NY_cm < 0
0 < NY_cm < 0.2
0.2 < NY_cm < 0.4
0.4 < NY_cm < 0.6
0.6 < NY_cm < 0.8
0.8 < NY_cm < 1.0
1.0 < NY_cm < 1.2
dN/dφ (arb. units)
φ_rp (deg)
-180 -60 60 180
0.2 < p_t < 0.4 GeV

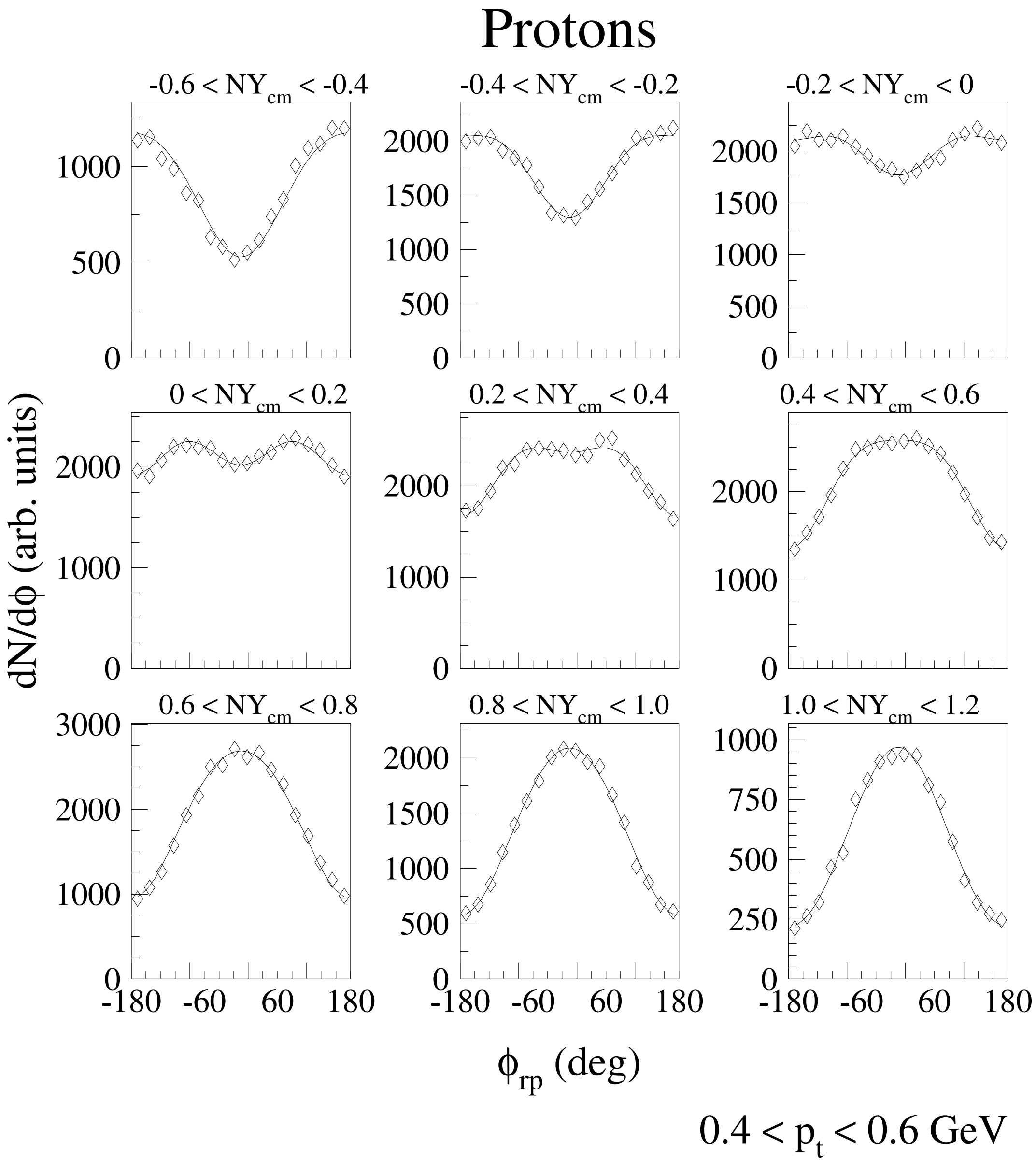
Protons
-0.6 < NY_cm < -0.4
-0.4 < NY_cm < -0.2
-0.2 < NY_cm < 0
0 < NY_cm < 0.2
0.2 < NY_cm < 0.4
0.4 < NY_cm < 0.6
0.6 < NY_cm < 0.8
0.8 < NY_cm < 1.0
1.0 < NY_cm < 1.2
dN/dφ (arb. units)
φ_rp (deg)
0.4 < p_t < 0.6 GeV

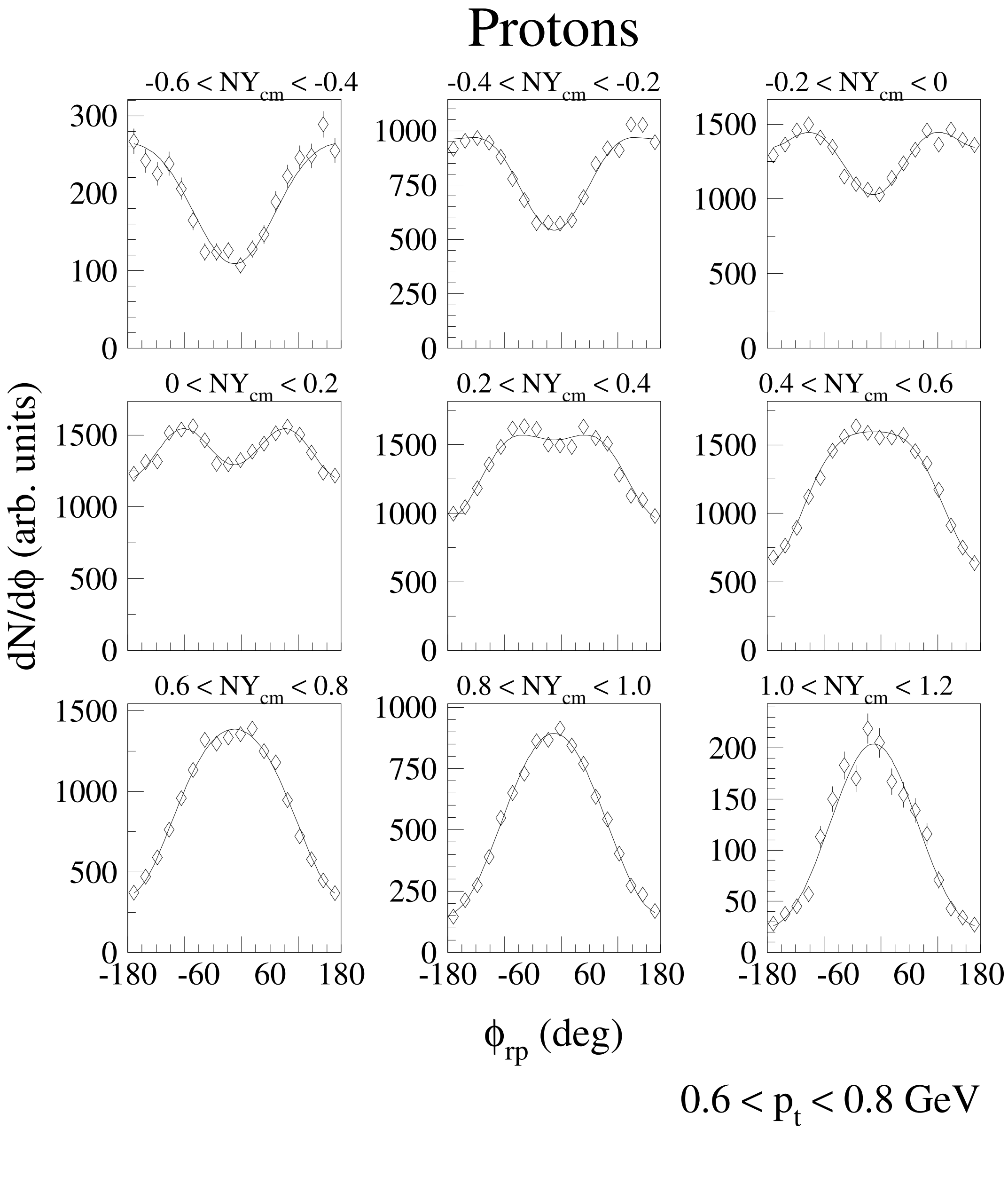
Protons
-0.6 < NY_cm < -0.4
-0.4 < NY_cm < -0.2
-0.2 < NY_cm < 0
0 < NY_cm < 0.2
0.2 < NY_cm < 0.4
0.4 < NY_cm < 0.6
0.6 < NY_cm < 0.8
0.8 < NY_cm < 1.0
1.0 < NY_cm < 1.2
dN/dϕ (arb. units)
ϕ_rp (deg)
0.6 < p_t < 0.8 GeV

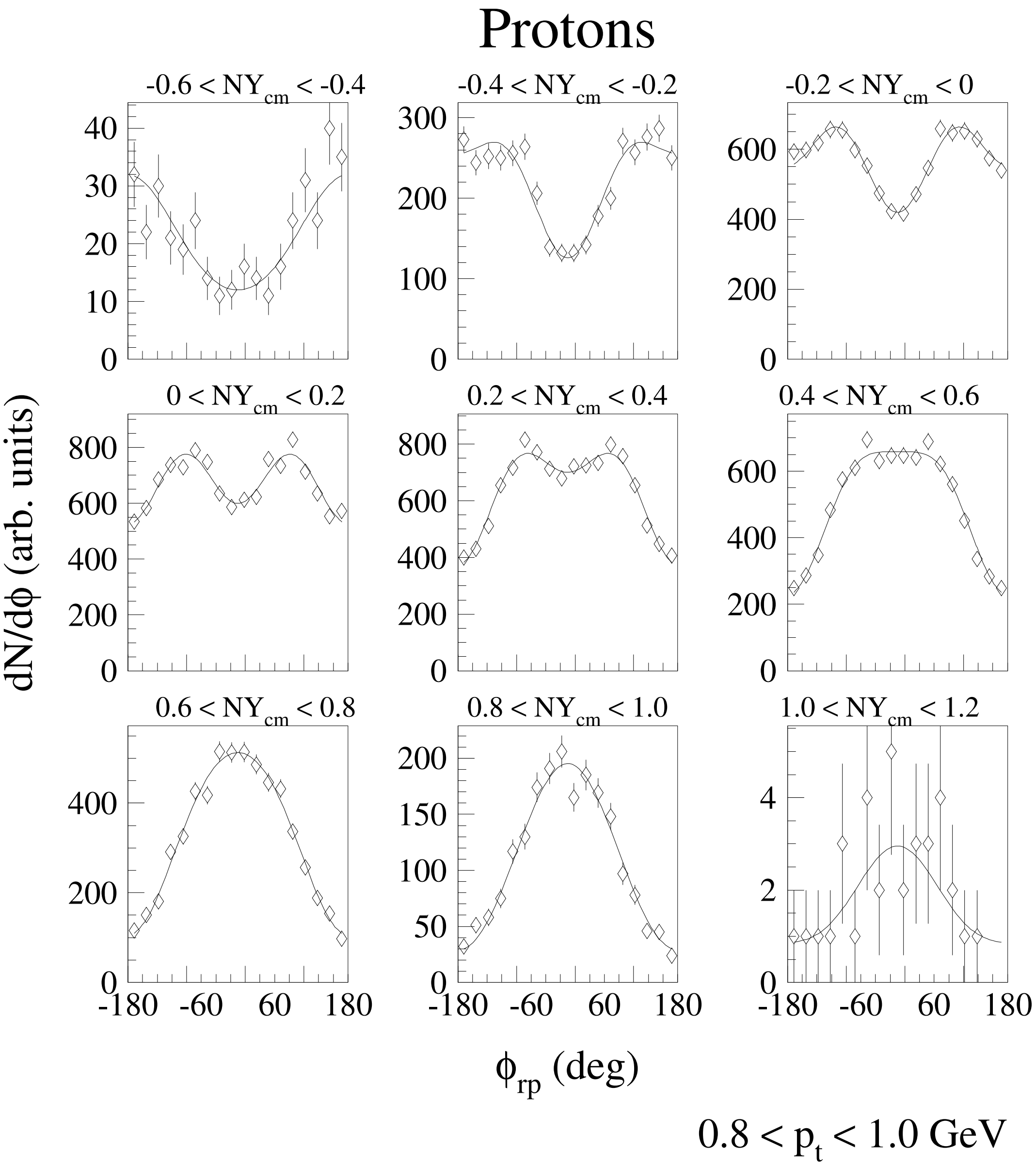

Protons
-0.6 < NY_cm < -0.4
-0.4 < NY_cm < -0.2
-0.2 < NY_cm < 0
0 < NY_cm < 0.2
0.2 < NY_cm < 0.4
0.4 < NY_cm < 0.6
0.6 < NY_cm < 0.8
0.8 < NY_cm < 1.0
1.0 < NY_cm < 1.2
dN/dφ (arb. units)
φ_rp (deg)
0.8 < p_t < 1.0 GeV

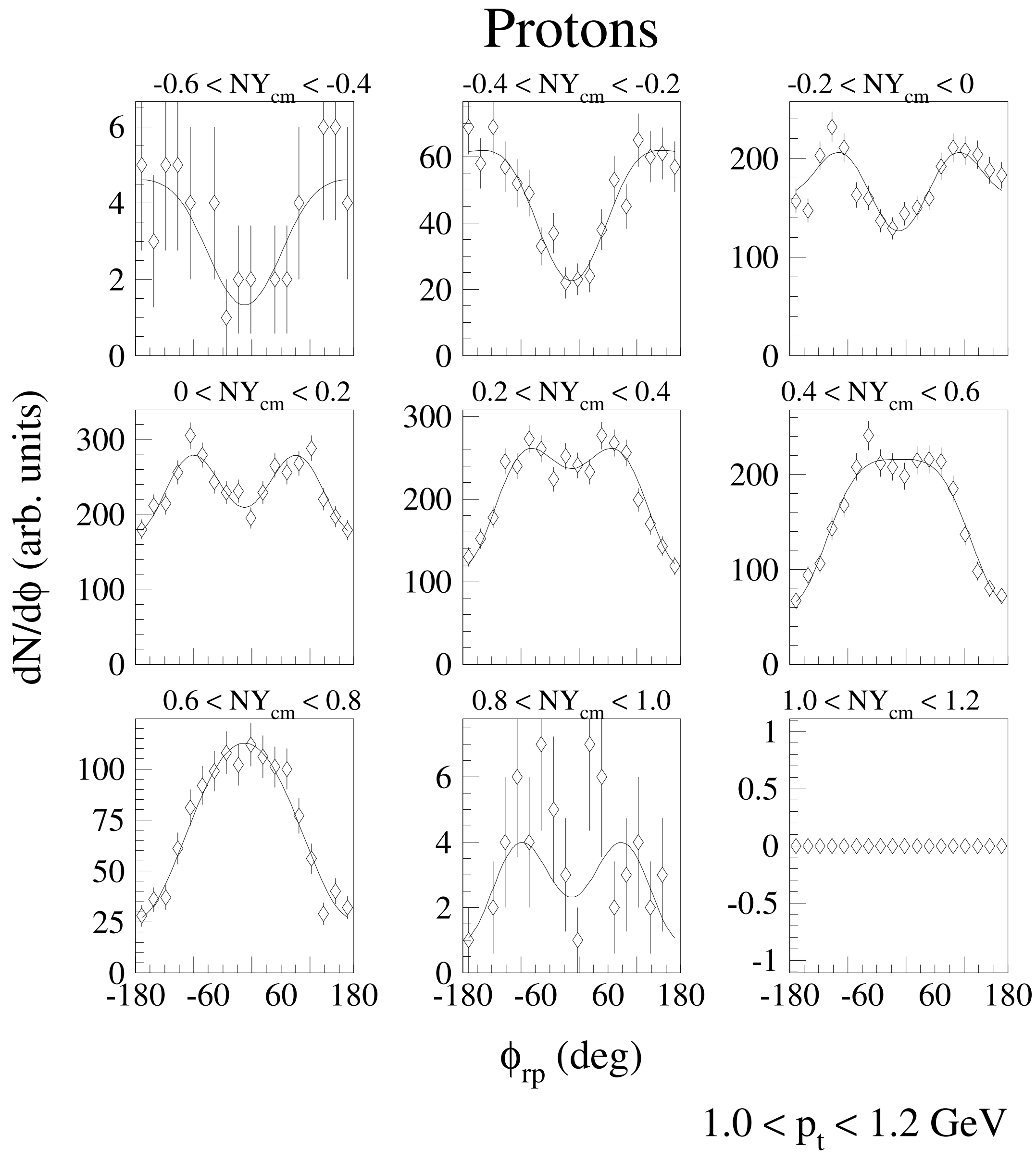

Protons
-0.6 < NY_cm < -0.4
-0.4 < NY_cm < -0.2
-0.2 < NY_cm < 0
0 < NY_cm < 0.2
0.2 < NY_cm < 0.4
0.4 < NY_cm < 0.6
0.6 < NY_cm < 0.8
0.8 < NY_cm < 1.0
1.0 < NY_cm < 1.2
dN/dφ (arb. units)
φ_rp (deg)
-180
-60
60
180
1.0 < p_t < 1.2 GeV

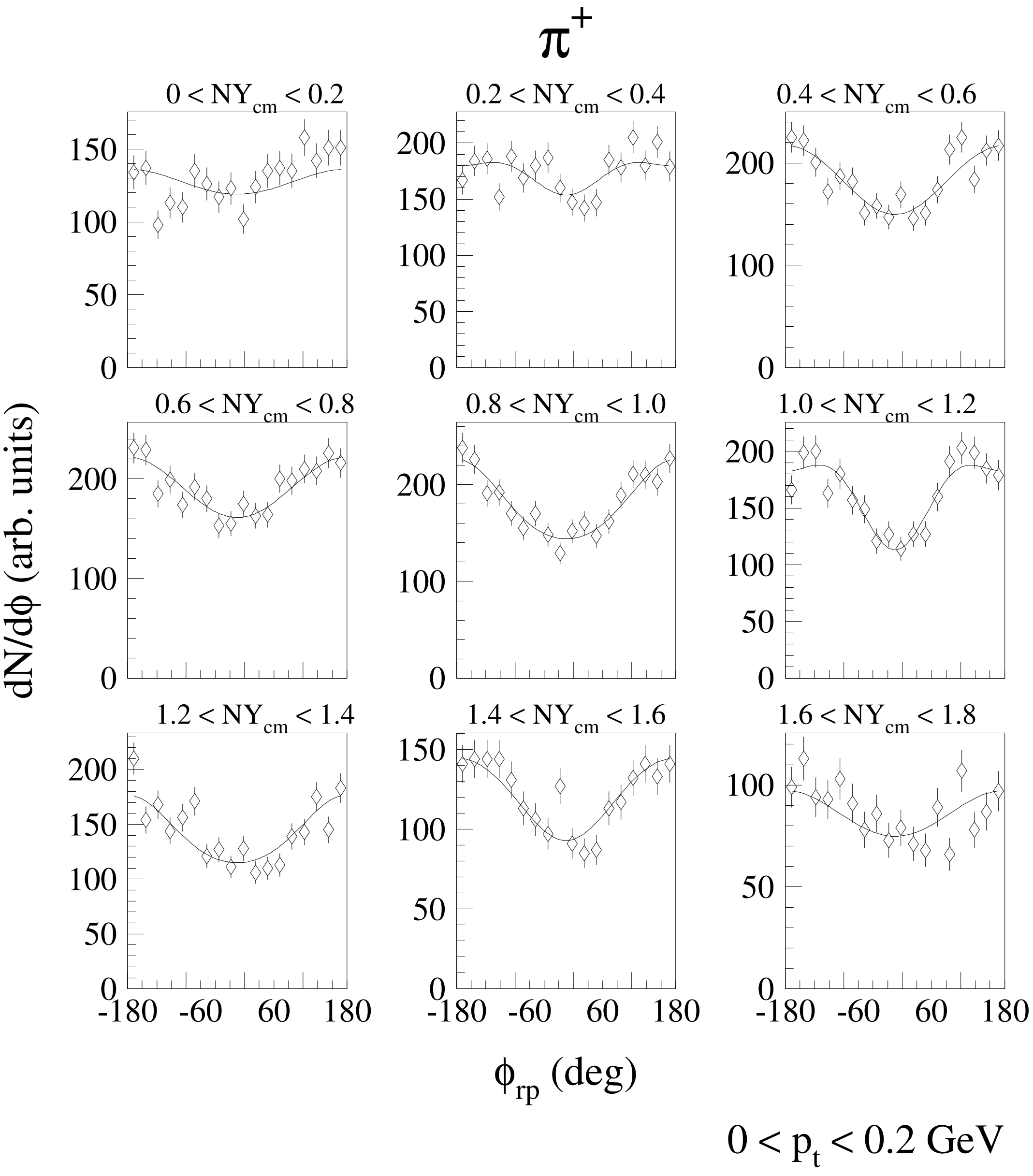

π^+
$0 < NY_{cm} < 0.2$
$0.2 < NY_{cm} < 0.4$
$0.4 < NY_{cm} < 0.6$
$0.6 < NY_{cm} < 0.8$
$0.8 < NY_{cm} < 1.0$
$1.0 < NY_{cm} < 1.2$
$1.2 < NY_{cm} < 1.4$
$1.4 < NY_{cm} < 1.6$
$1.6 < NY_{cm} < 1.8$
$dN/d\phi$ (arb. units)
ϕ_{rp} (deg)
$0 < p_t < 0.2$ GeV

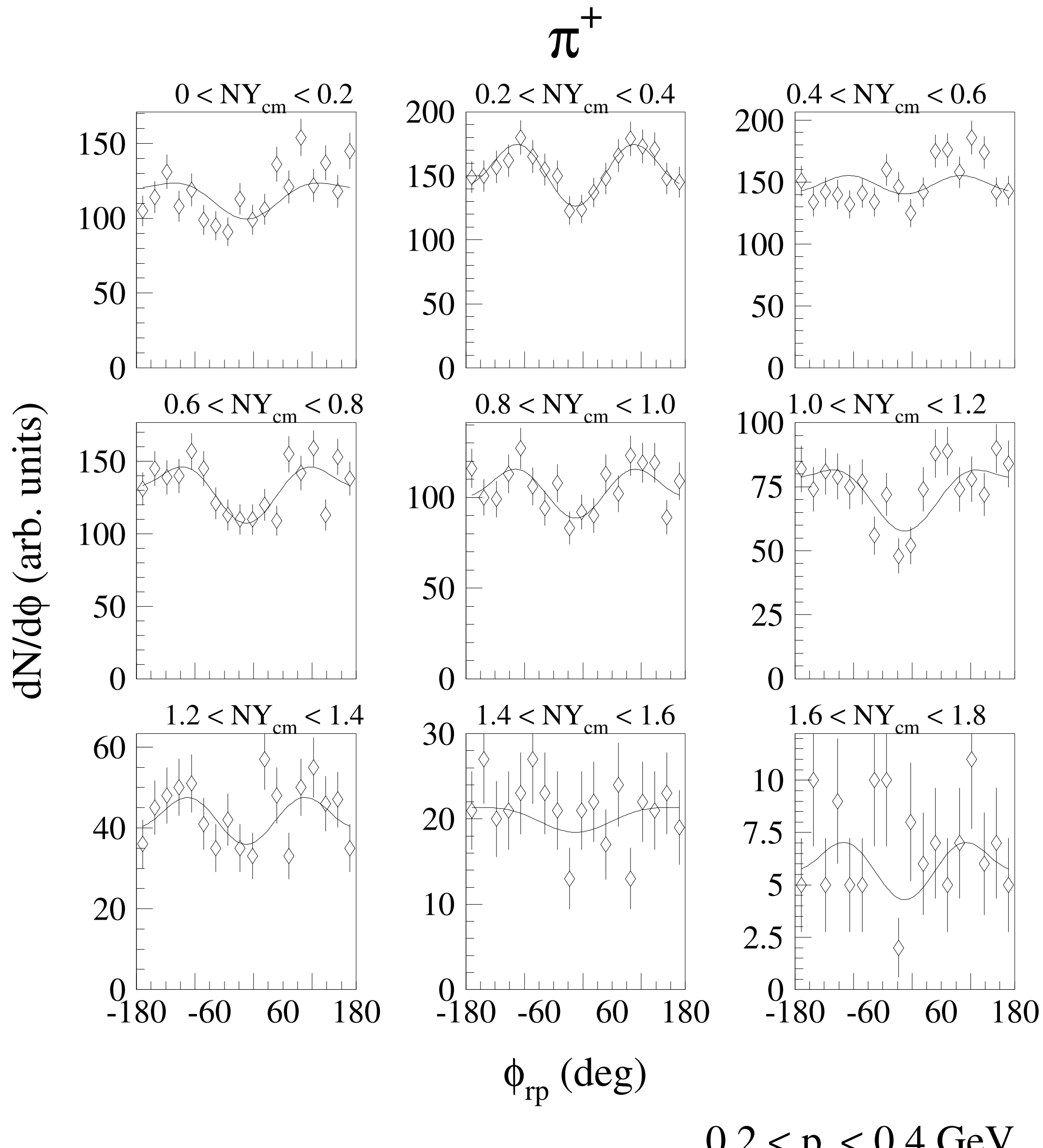

π^+
$0 < NY_{cm} < 0.2$
$0.2 < NY_{cm} < 0.4$
$0.4 < NY_{cm} < 0.6$
$0.6 < NY_{cm} < 0.8$
$0.8 < NY_{cm} < 1.0$
$1.0 < NY_{cm} < 1.2$
$1.2 < NY_{cm} < 1.4$
$1.4 < NY_{cm} < 1.6$
$1.6 < NY_{cm} < 1.8$
dN/dϕ (arb. units)
ϕ_{rp} (deg)
-180
-60
60
180
$0.2 < p_t < 0.4$ GeV

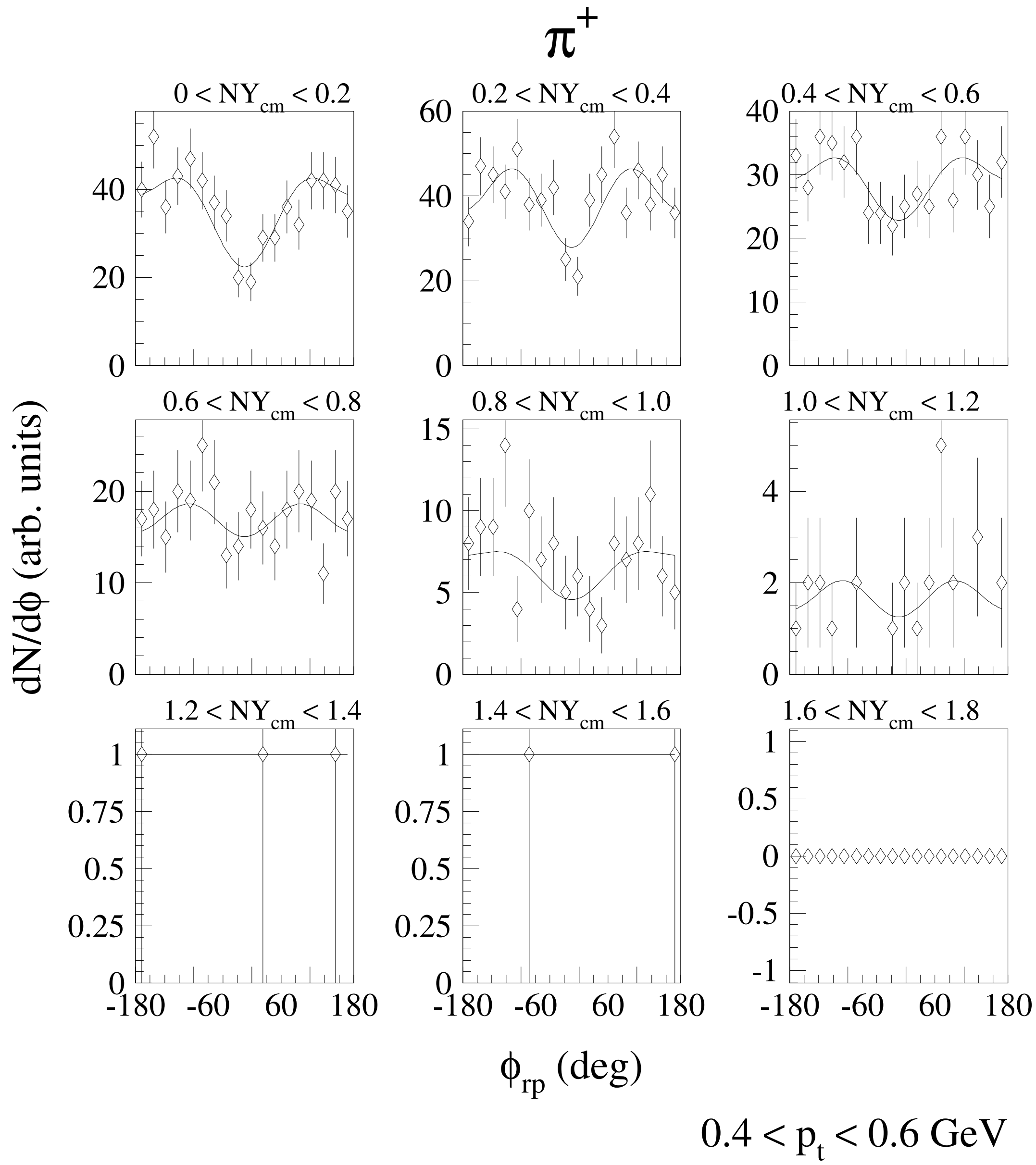

π+
0 < NYcm < 0.2
0.2 < NYcm < 0.4
0.4 < NYcm < 0.6
0.6 < NYcm < 0.8
0.8 < NYcm < 1.0
1.0 < NYcm < 1.2
1.2 < NYcm < 1.4
1.4 < NYcm < 1.6
1.6 < NYcm < 1.8
dN/dφ (arb. units)
φrp (deg)
0.4 < pt < 0.6 GeV

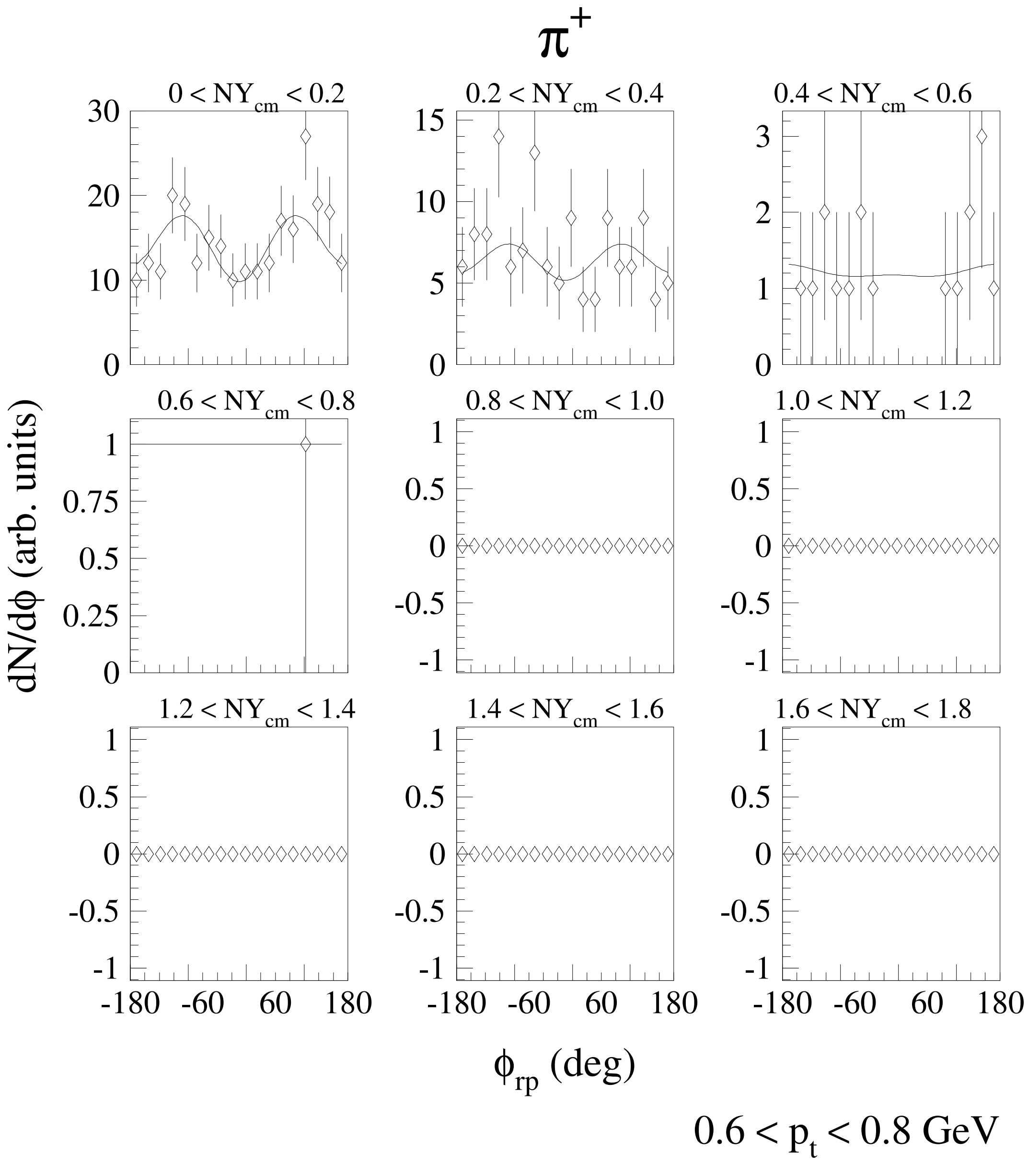

π^+
$0 < NY_{cm} < 0.2$
$0.2 < NY_{cm} < 0.4$
$0.4 < NY_{cm} < 0.6$
$0.6 < NY_{cm} < 0.8$
$0.8 < NY_{cm} < 1.0$
$1.0 < NY_{cm} < 1.2$
$1.2 < NY_{cm} < 1.4$
$1.4 < NY_{cm} < 1.6$
$1.6 < NY_{cm} < 1.8$
dN/dϕ (arb. units)
ϕ_{rp} (deg)
-180
-60
60
180
$0.6 < p_t < 0.8$ GeV

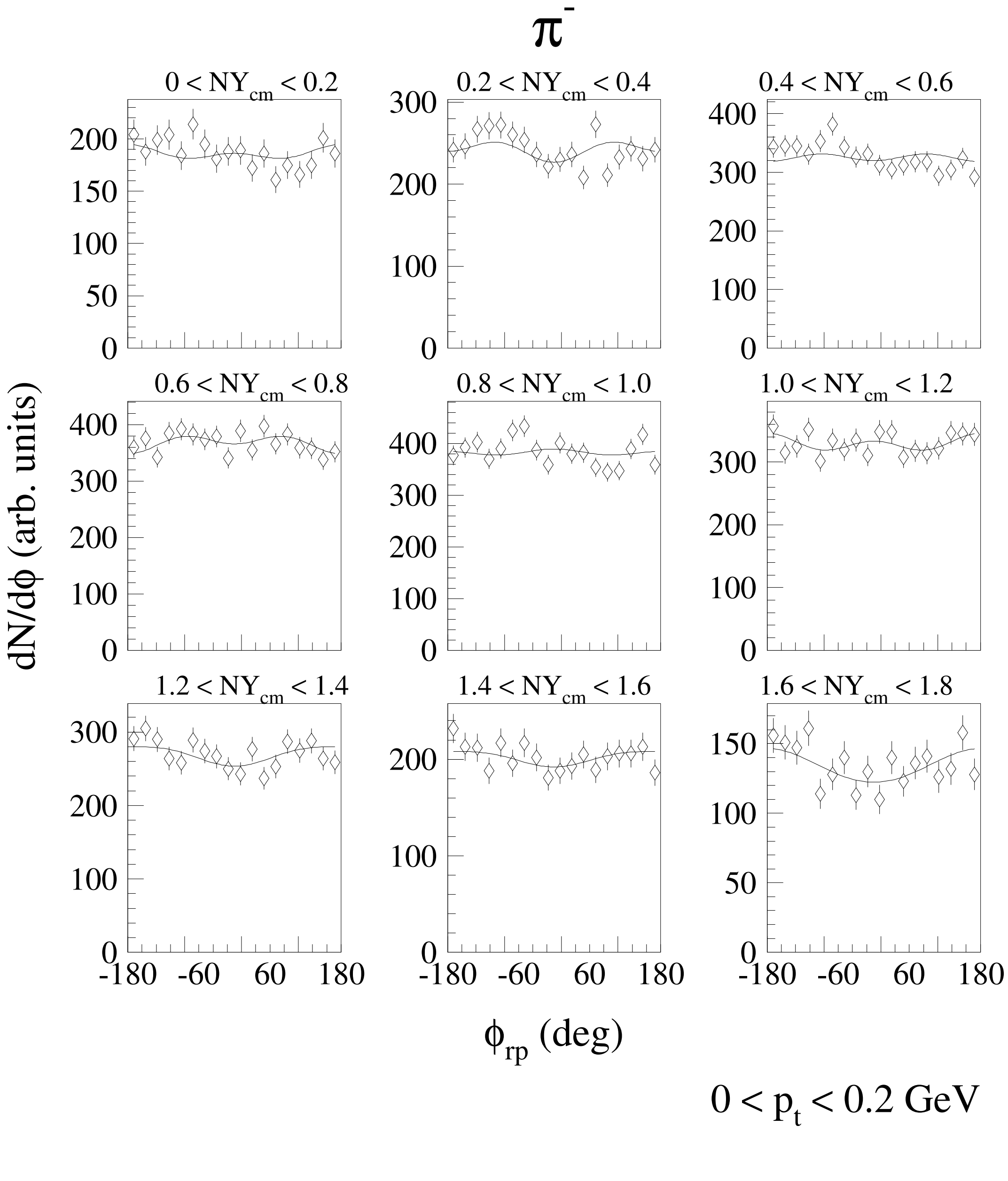
π-
0 < NY_cm < 0.2
0.2 < NY_cm < 0.4
0.4 < NY_cm < 0.6
0.6 < NY_cm < 0.8
0.8 < NY_cm < 1.0
1.0 < NY_cm < 1.2
1.2 < NY_cm < 1.4
1.4 < NY_cm < 1.6
1.6 < NY_cm < 1.8
dN/dφ (arb. units)
φ_rp (deg)
0 < p_t < 0.2 GeV

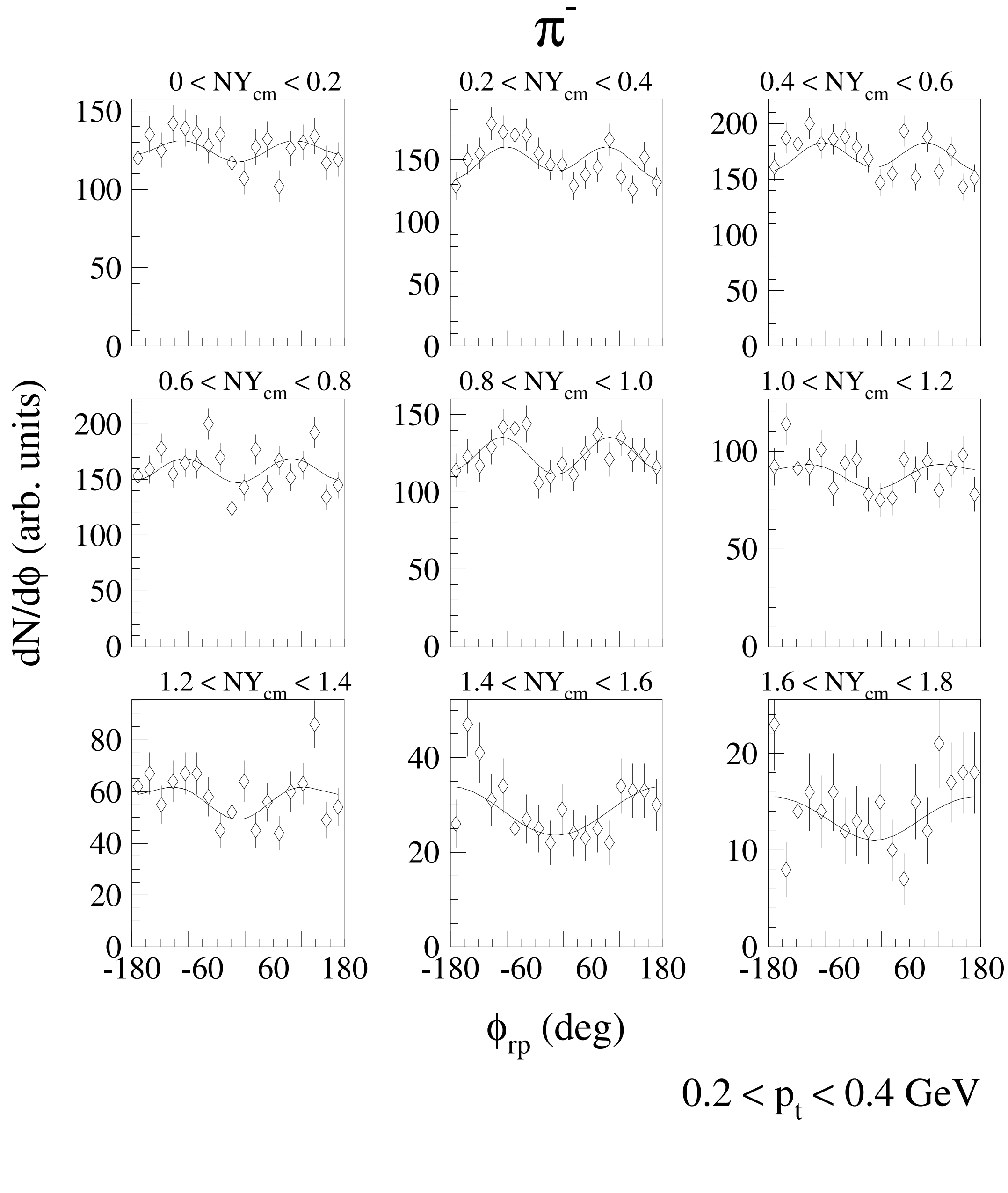
π⁻
0 < NY_cm < 0.2
0.2 < NY_cm < 0.4
0.4 < NY_cm < 0.6
0.6 < NY_cm < 0.8
0.8 < NY_cm < 1.0
1.0 < NY_cm < 1.2
1.2 < NY_cm < 1.4
1.4 < NY_cm < 1.6
1.6 < NY_cm < 1.8
dN/dφ (arb. units)
φ_rp (deg)
0.2 < p_t < 0.4 GeV

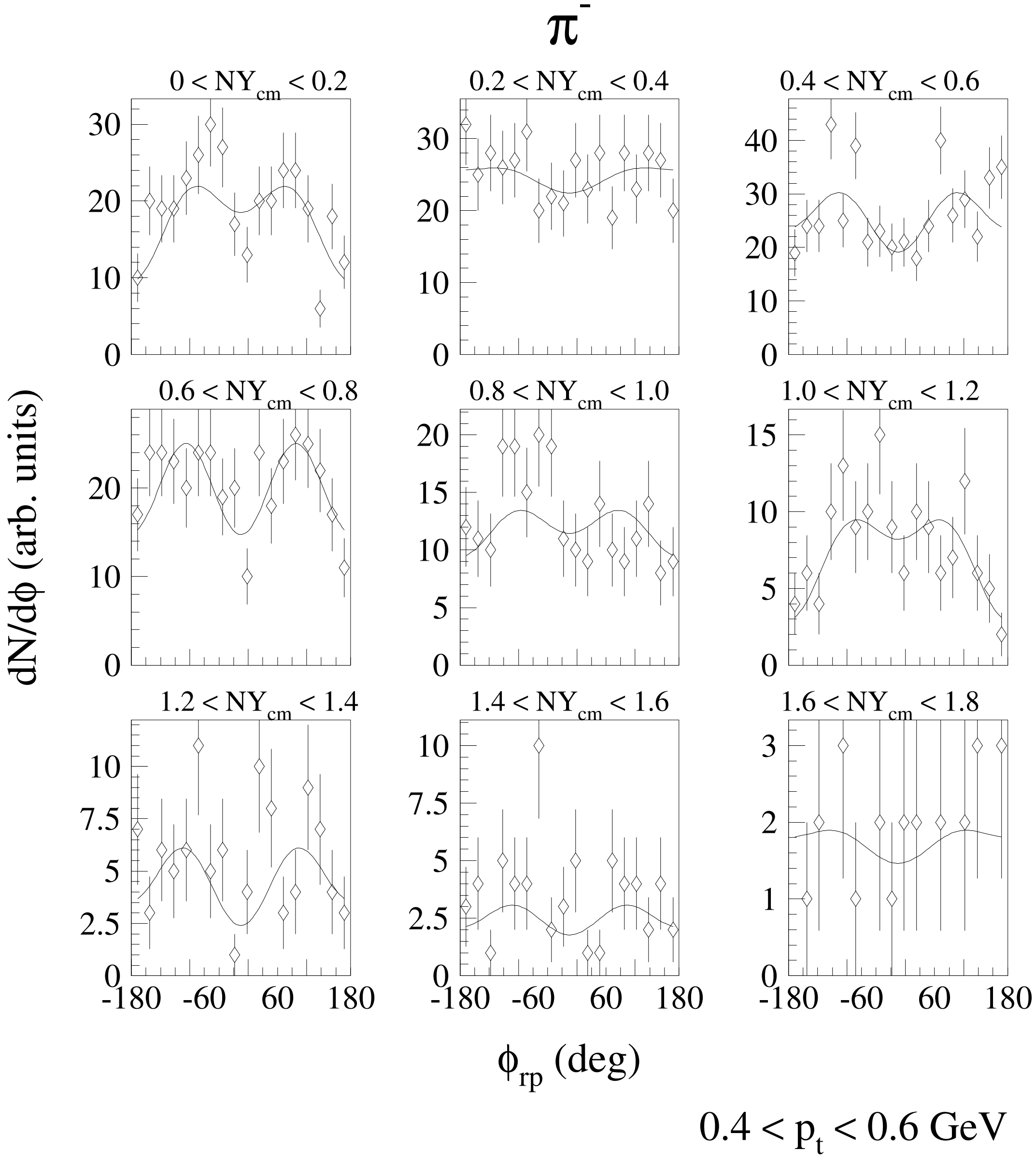
π⁻
0 < NY_cm < 0.2
0.2 < NY_cm < 0.4
0.4 < NY_cm < 0.6
0.6 < NY_cm < 0.8
0.8 < NY_cm < 1.0
1.0 < NY_cm < 1.2
1.2 < NY_cm < 1.4
1.4 < NY_cm < 1.6
1.6 < NY_cm < 1.8
dN/dϕ (arb. units)
ϕ_rp (deg)
0.4 < p_t < 0.6 GeV

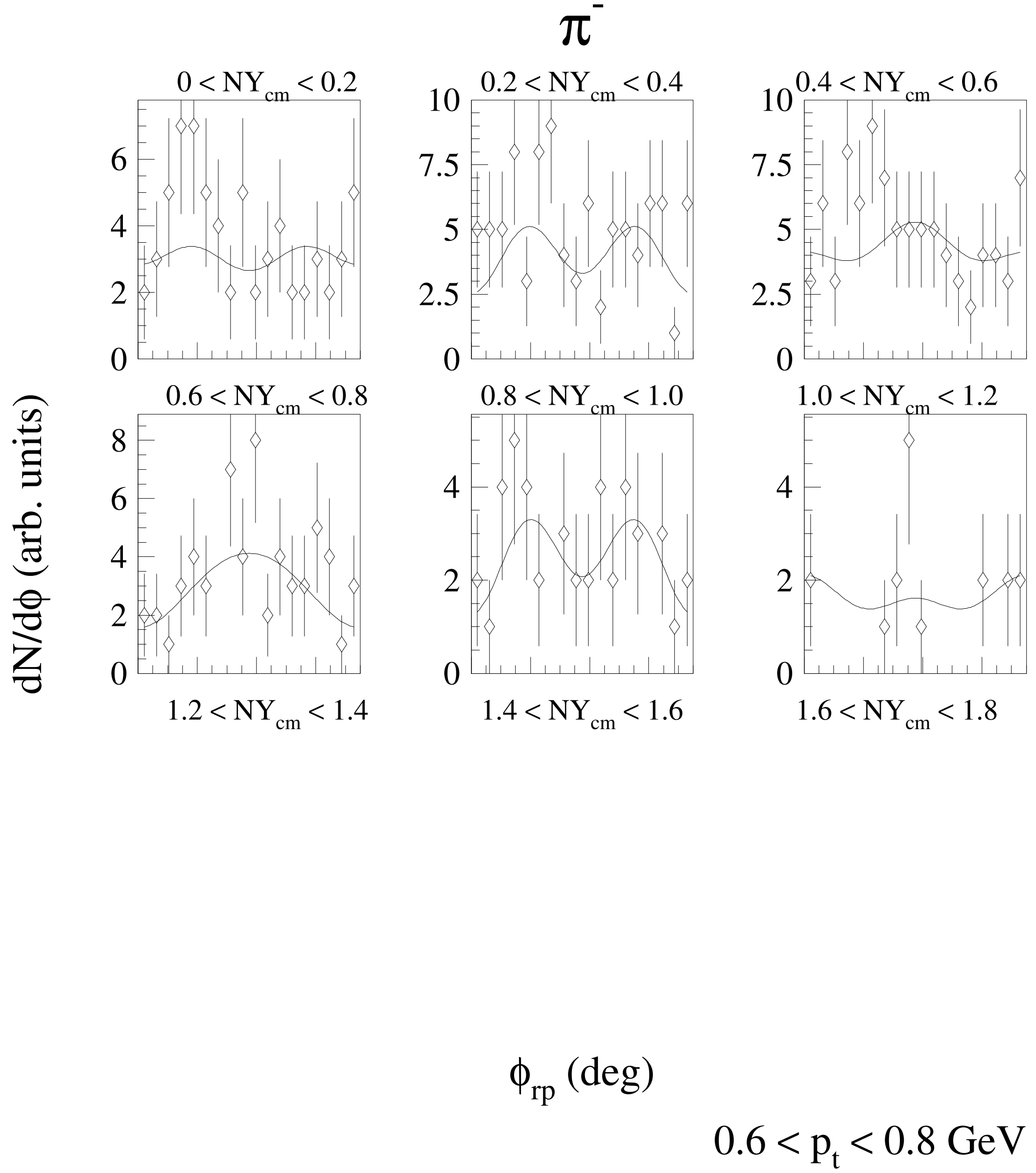

π⁻
0 < NY_cm < 0.2
0.2 < NY_cm < 0.4
0.4 < NY_cm < 0.6
0.6 < NY_cm < 0.8
0.8 < NY_cm < 1.0
1.0 < NY_cm < 1.2
1.2 < NY_cm < 1.4
1.4 < NY_cm < 1.6
1.6 < NY_cm < 1.8
dN/dφ (arb. units)
φ_rp (deg)
0.6 < p_t < 0.8 GeV

Appendix B

Squeeze-out Projections — Impact Parameter

Shown in this Appendix are projections from Figures 6.11, 6.12, and 6.13. The 2 dimensional figures were plotted as functions of normalized rapidity (Y_{cm}/Y_{beam}) and azimuthal angle (ϕ_{RP}). A series of these plots was then done, one for each impact parameter. The projections shown in this appendix have been sliced in rapidity, then projected onto the ϕ axis for each impact parameter.

Each figure is labeled at the top with the particle identification, at the bottom with the impact parameter cut, and at the top of each panel with the rapidity slice. The protons are shown for a midrapidity region while the pions are all forward going. The fourth panel ($0 < NY_{cm} < 0.2$) of each page of proton plots corresponds to a panel in Figure 6.14. For the pions, the second, third, and fourth panels of each figure added together correspond to the panels shown in Figures 6.15 and 6.16

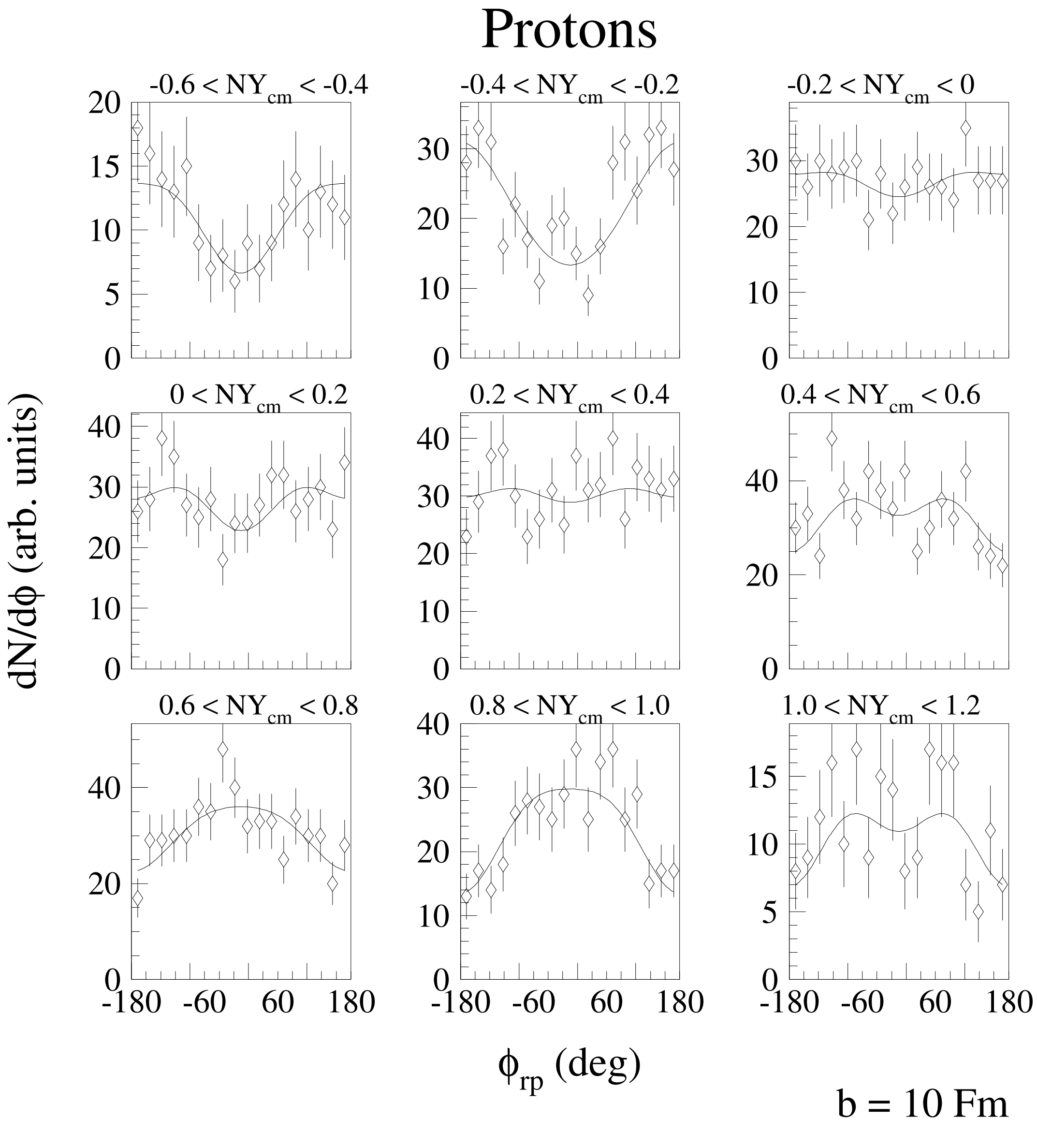
Protons
-0.6 < NY_cm < -0.4
-0.4 < NY_cm < -0.2
-0.2 < NY_cm < 0
0 < NY_cm < 0.2
0.2 < NY_cm < 0.4
0.4 < NY_cm < 0.6
0.6 < NY_cm < 0.8
0.8 < NY_cm < 1.0
1.0 < NY_cm < 1.2
dN/dφ (arb. units)
φ_rp (deg)
b = 10 Fm

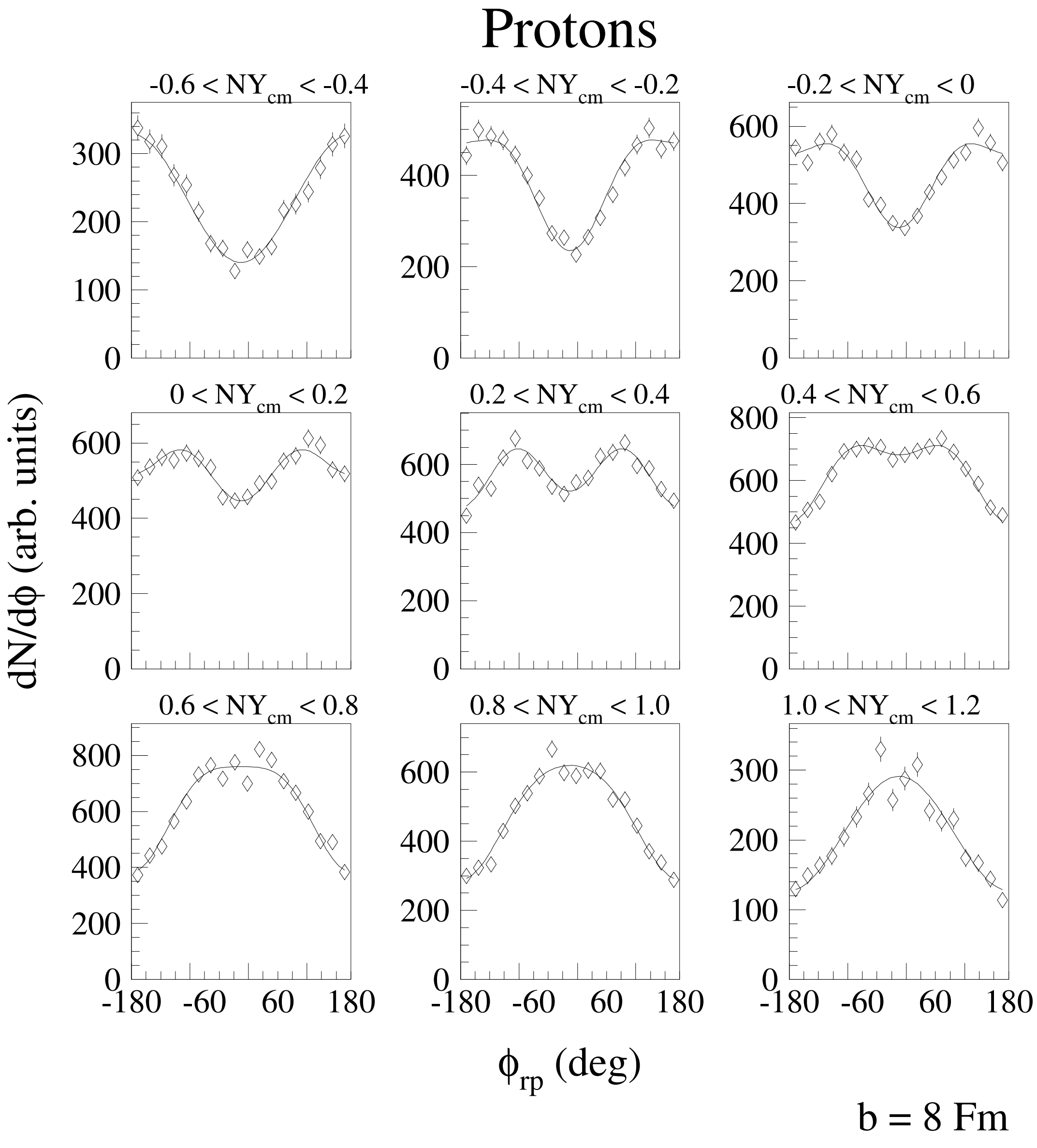

Protons
-0.6 < NY$_{cm}$ < -0.4
-0.4 < NY$_{cm}$ < -0.2
-0.2 < NY$_{cm}$ < 0
0 < NY$_{cm}$ < 0.2
0.2 < NY$_{cm}$ < 0.4
0.4 < NY$_{cm}$ < 0.6
0.6 < NY$_{cm}$ < 0.8
0.8 < NY$_{cm}$ < 1.0
1.0 < NY$_{cm}$ < 1.2
dN/dϕ (arb. units)
ϕ$_{rp}$ (deg)
-180 -60 60 180
b = 8 Fm

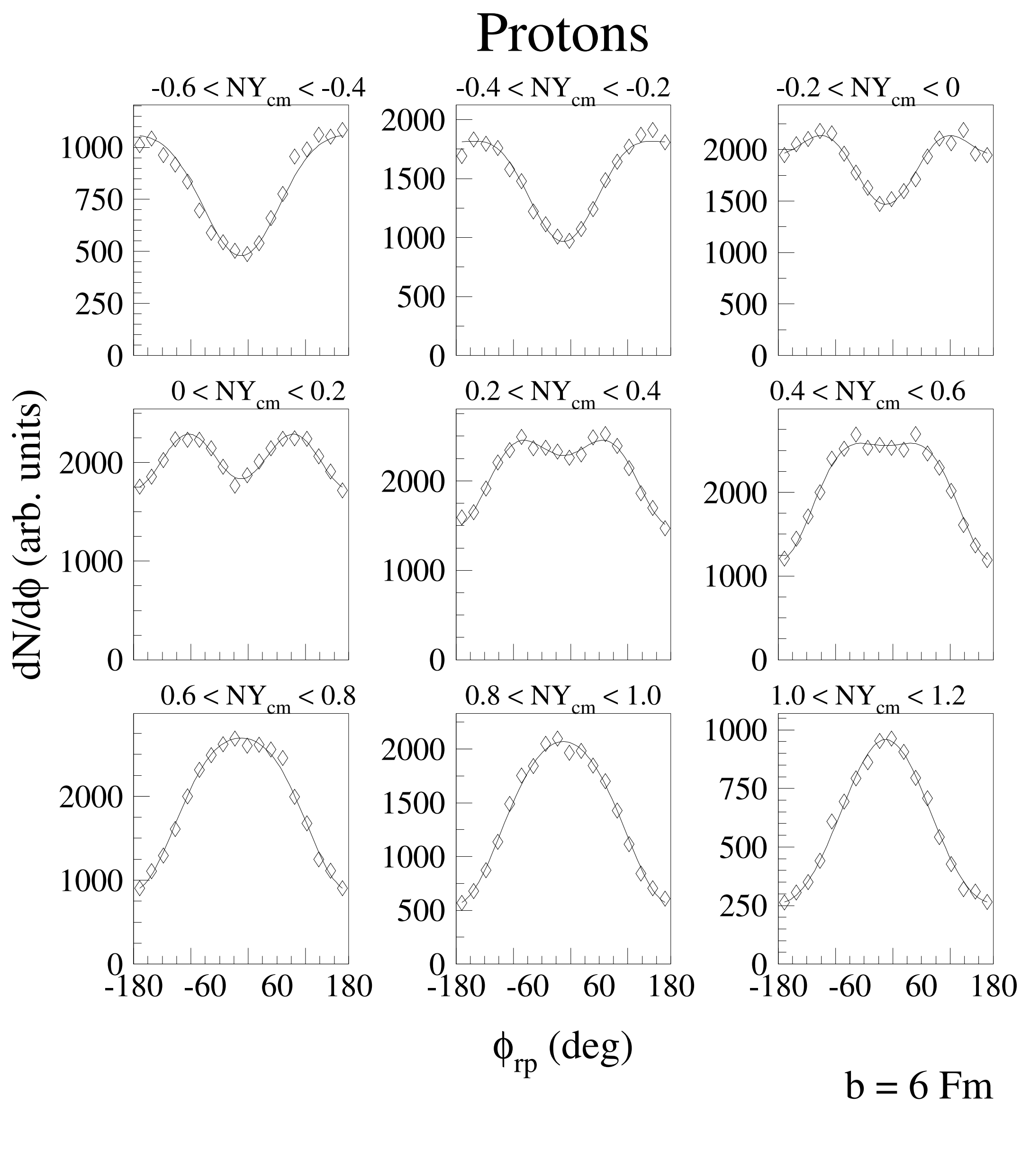

Protons
-0.6 < NY_cm < -0.4
-0.4 < NY_cm < -0.2
-0.2 < NY_cm < 0
0 < NY_cm < 0.2
0.2 < NY_cm < 0.4
0.4 < NY_cm < 0.6
0.6 < NY_cm < 0.8
0.8 < NY_cm < 1.0
1.0 < NY_cm < 1.2
dN/dϕ (arb. units)
ϕ_rp (deg)
b = 6 Fm

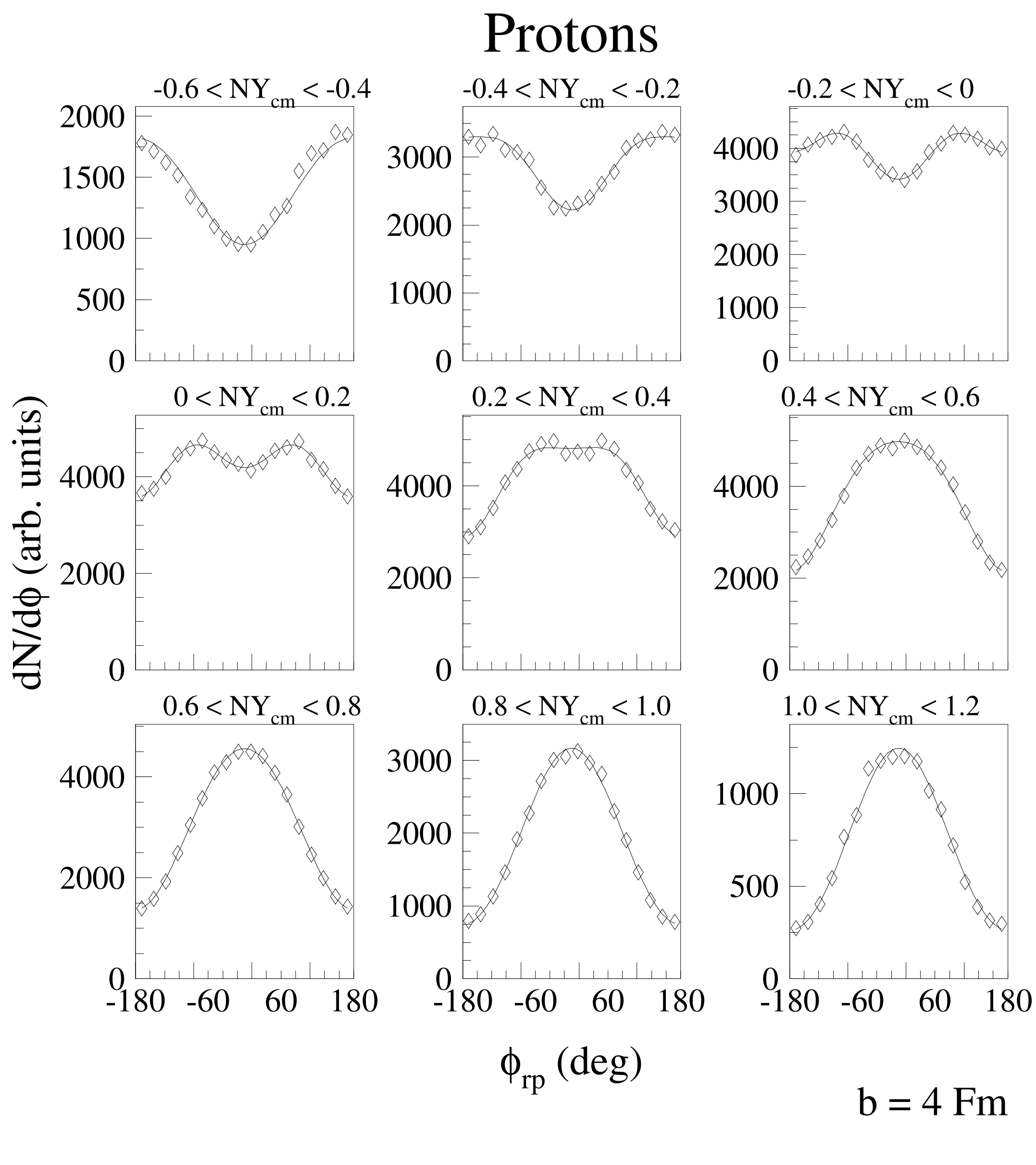

Protons
-0.6 < NYcm < -0.4
-0.4 < NYcm < -0.2
-0.2 < NYcm < 0
0 < NYcm < 0.2
0.2 < NYcm < 0.4
0.4 < NYcm < 0.6
0.6 < NYcm < 0.8
0.8 < NYcm < 1.0
1.0 < NYcm < 1.2
dN/dφ (arb. units)
φrp (deg)
b = 4 Fm

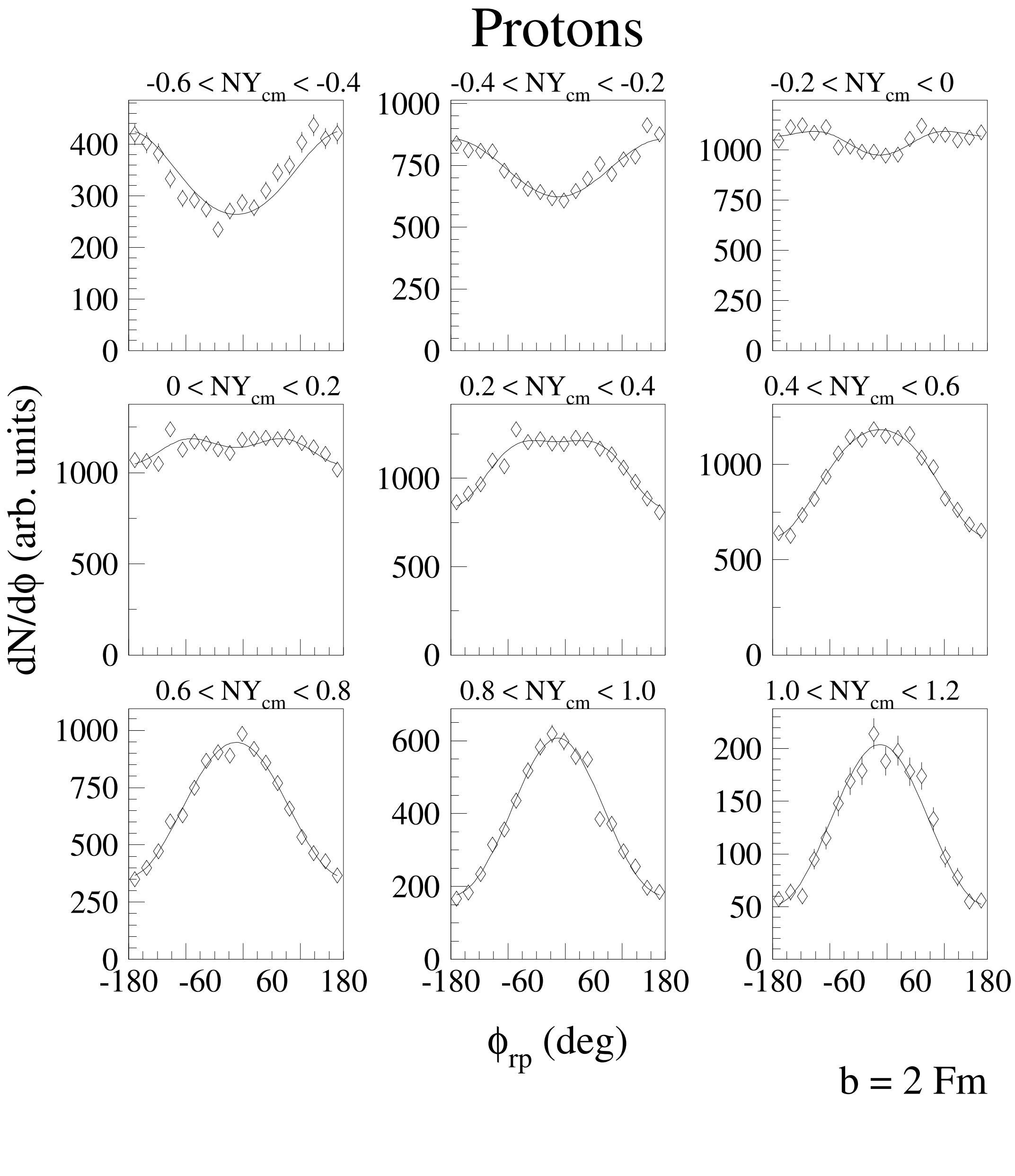

Protons
-0.6 < NY_cm < -0.4
-0.4 < NY_cm < -0.2
-0.2 < NY_cm < 0
0 < NY_cm < 0.2
0.2 < NY_cm < 0.4
0.4 < NY_cm < 0.6
0.6 < NY_cm < 0.8
0.8 < NY_cm < 1.0
1.0 < NY_cm < 1.2
dN/dϕ (arb. units)
ϕ_rp (deg)
b = 2 Fm

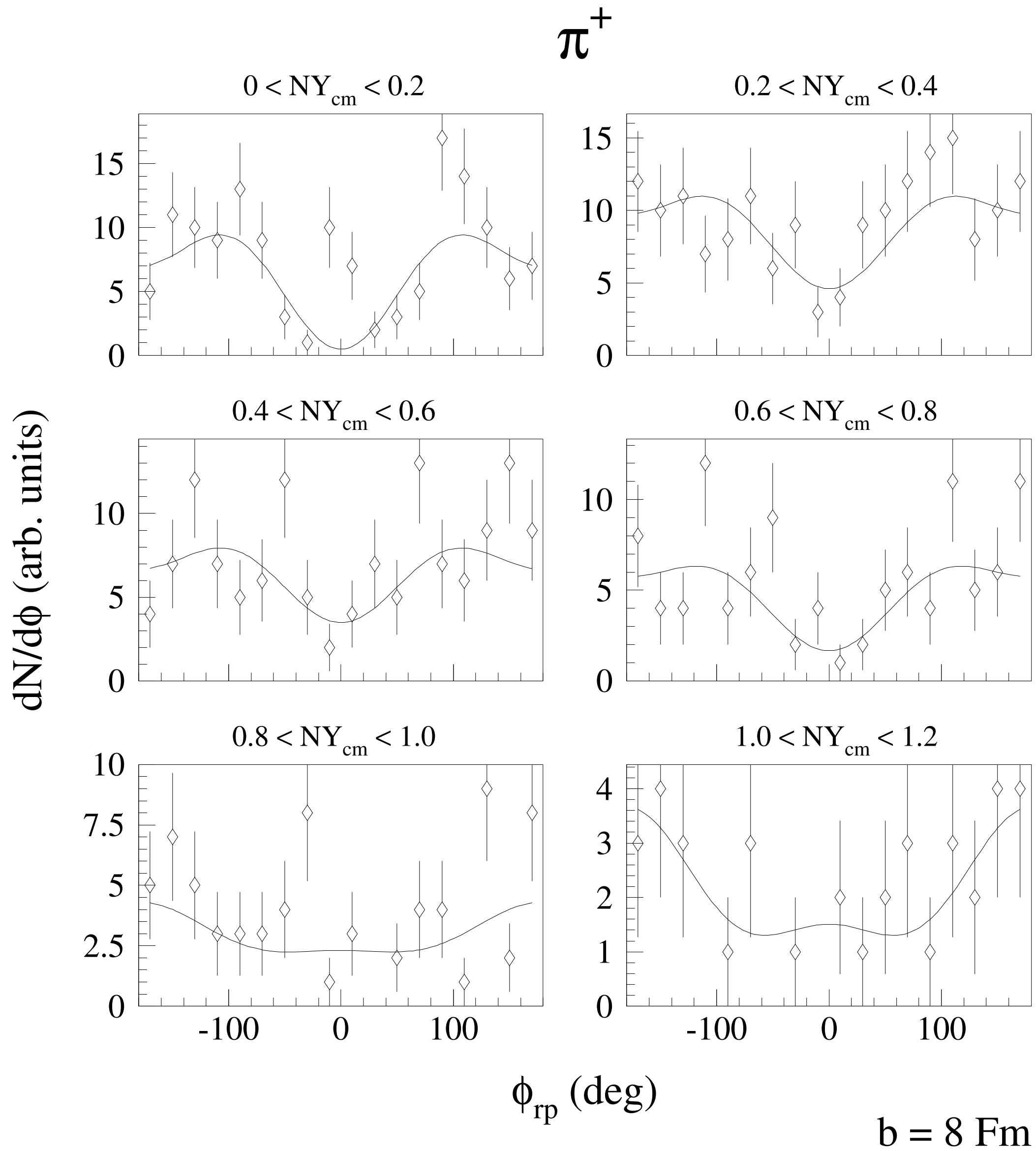

π+
0 < NYcm < 0.2
0.2 < NYcm < 0.4
0.4 < NYcm < 0.6
0.6 < NYcm < 0.8
0.8 < NYcm < 1.0
1.0 < NYcm < 1.2
dN/dφ (arb. units)
φrp (deg)
b = 8 Fm

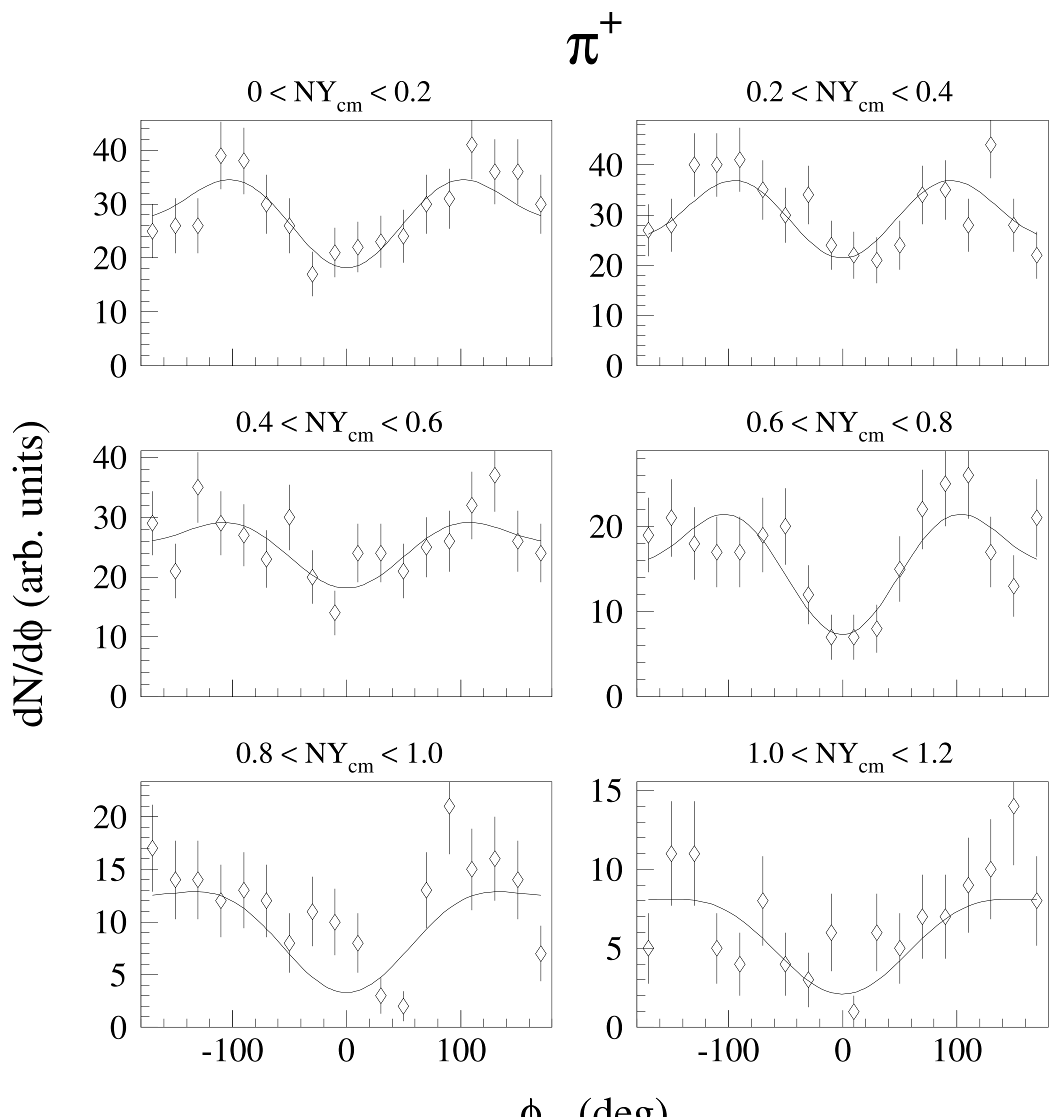

π+
0 < NYcm < 0.2
0.2 < NYcm < 0.4
0.4 < NYcm < 0.6
0.6 < NYcm < 0.8
0.8 < NYcm < 1.0
1.0 < NYcm < 1.2
dN/dϕ (arb. units)
ϕrp (deg)
b = 6 Fm

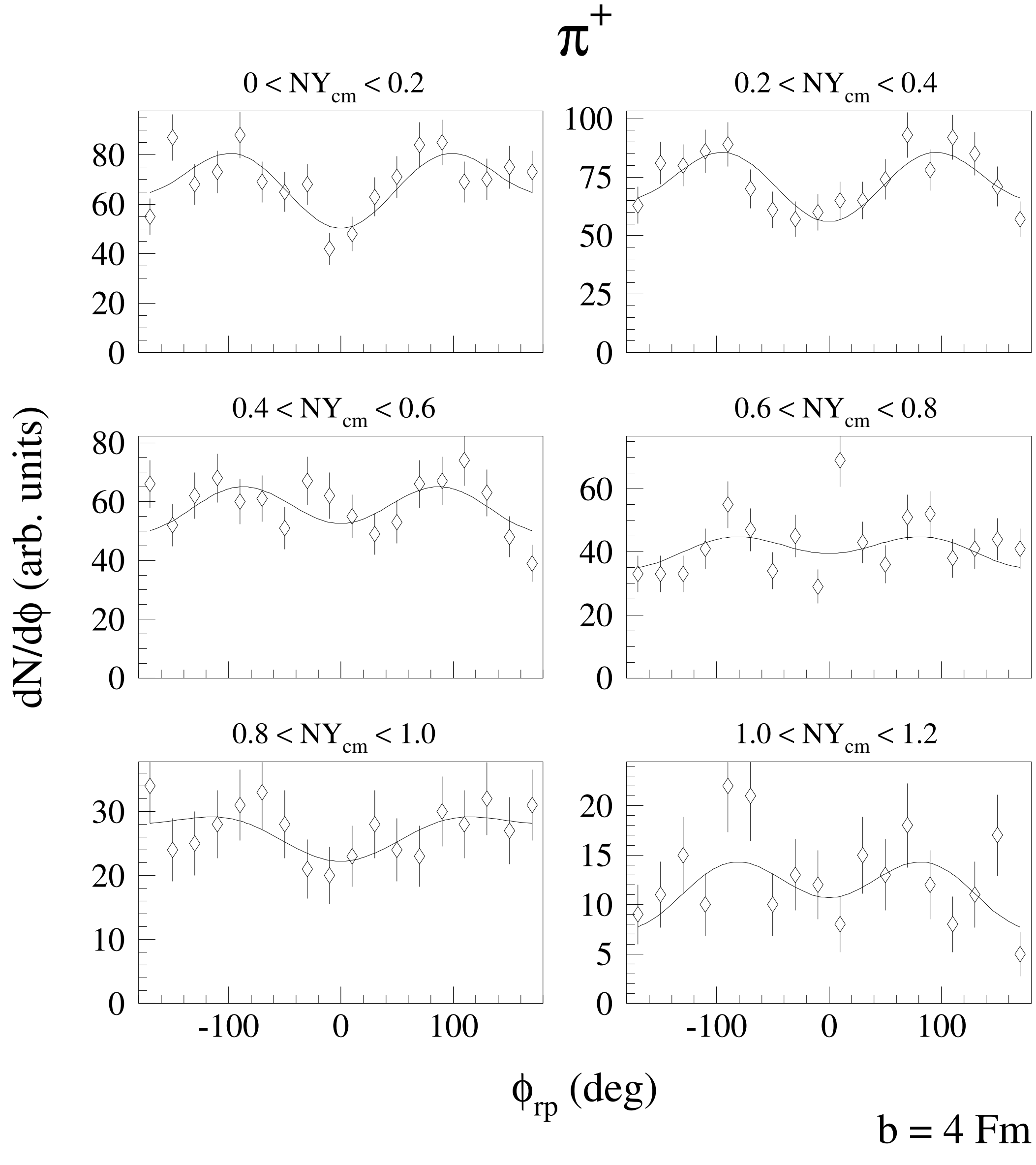

π^+
$0 < NY_{cm} < 0.2$
$0.2 < NY_{cm} < 0.4$
$0.4 < NY_{cm} < 0.6$
$0.6 < NY_{cm} < 0.8$
$0.8 < NY_{cm} < 1.0$
$1.0 < NY_{cm} < 1.2$
$dN/d\phi$ (arb. units)
ϕ_{rp} (deg)
b = 4 Fm

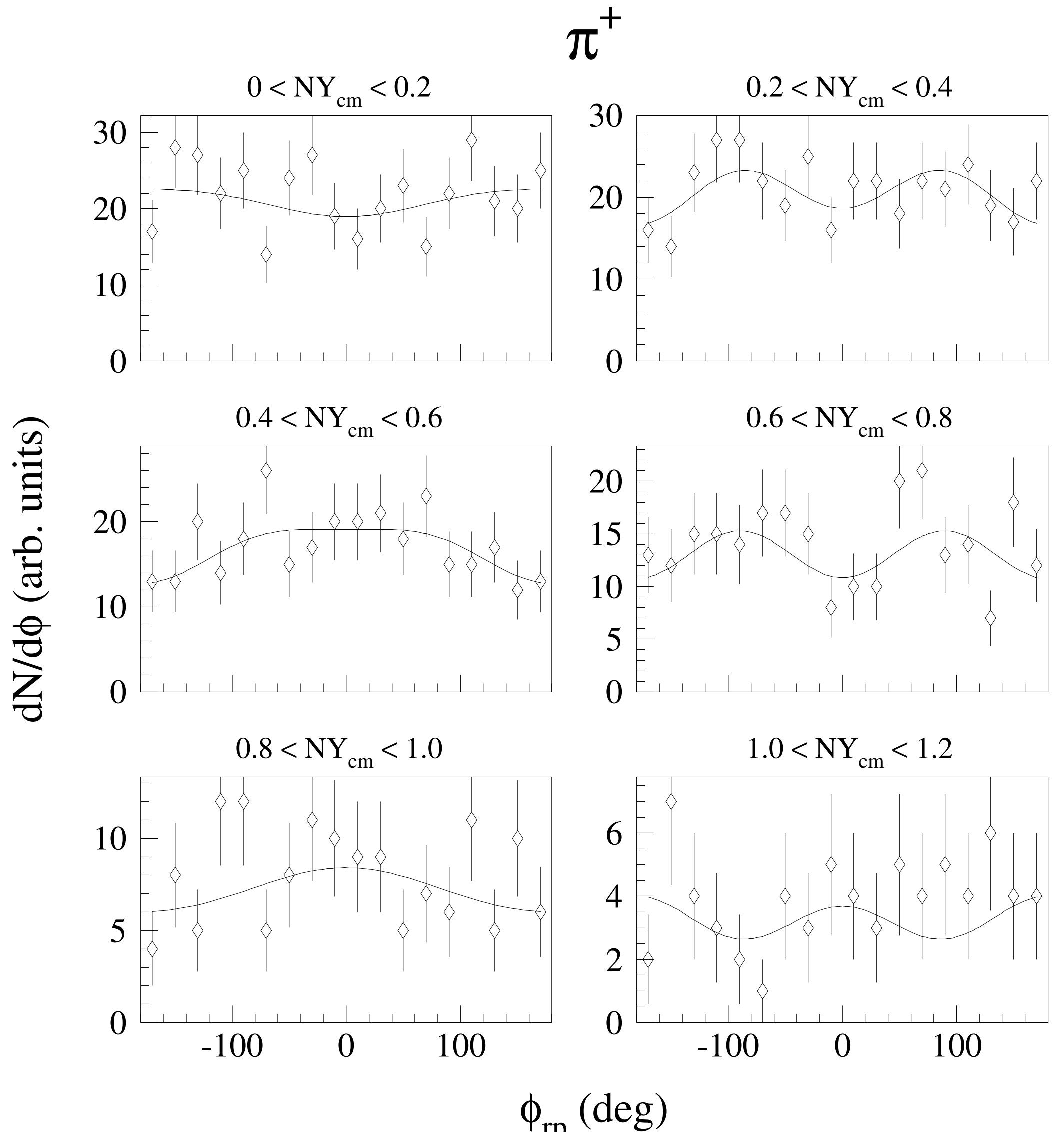
π+
0 < NYcm < 0.2
0.2 < NYcm < 0.4
0.4 < NYcm < 0.6
0.6 < NYcm < 0.8
0.8 < NYcm < 1.0
1.0 < NYcm < 1.2
dN/dφ (arb. units)
φrp (deg)
b = 2 Fm

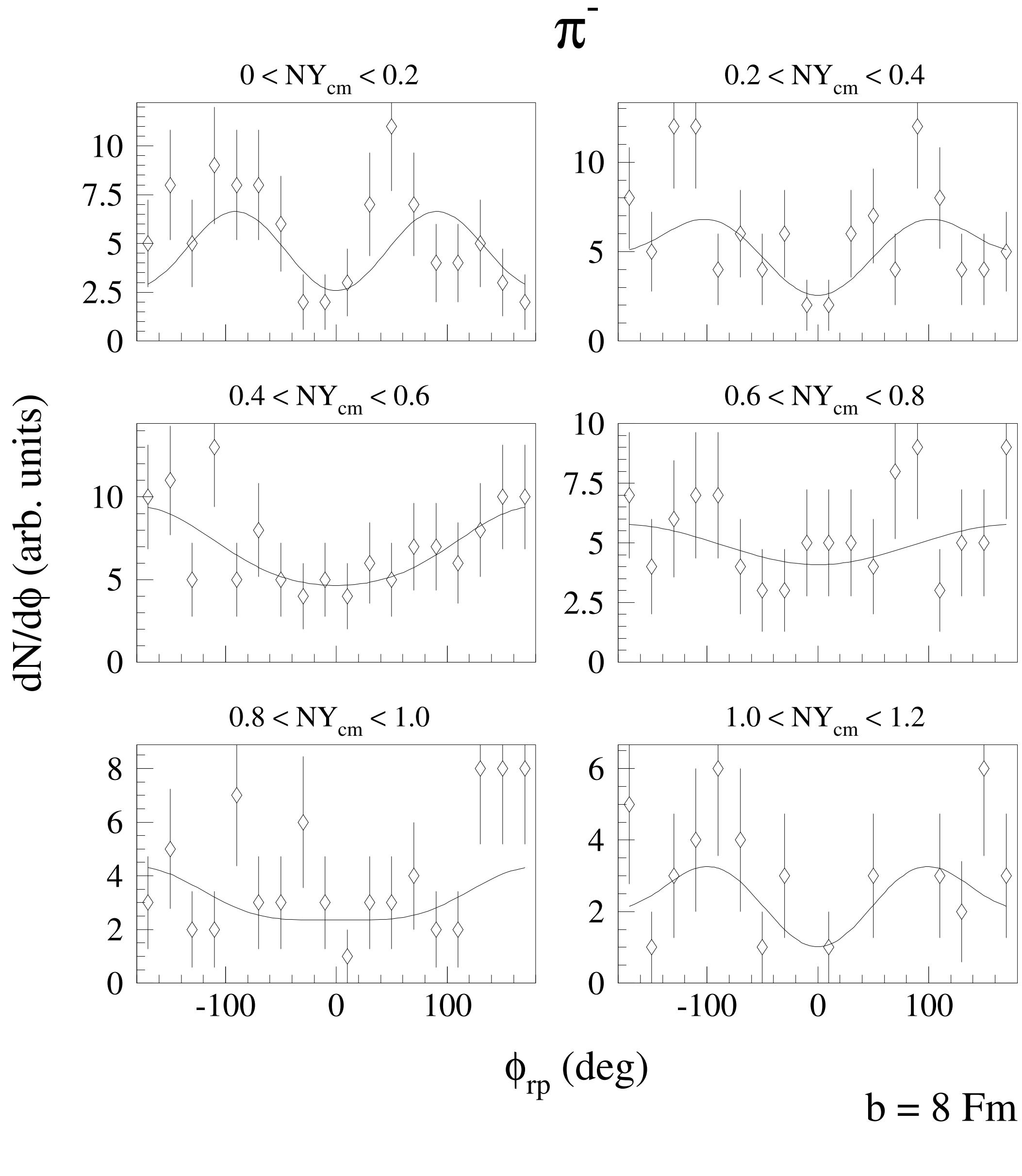

π^-
0 < NY$_{cm}$ < 0.2
0.2 < NY$_{cm}$ < 0.4
0.4 < NY$_{cm}$ < 0.6
0.6 < NY$_{cm}$ < 0.8
0.8 < NY$_{cm}$ < 1.0
1.0 < NY$_{cm}$ < 1.2
dN/dϕ (arb. units)
ϕ$_{rp}$ (deg)
b = 8 Fm

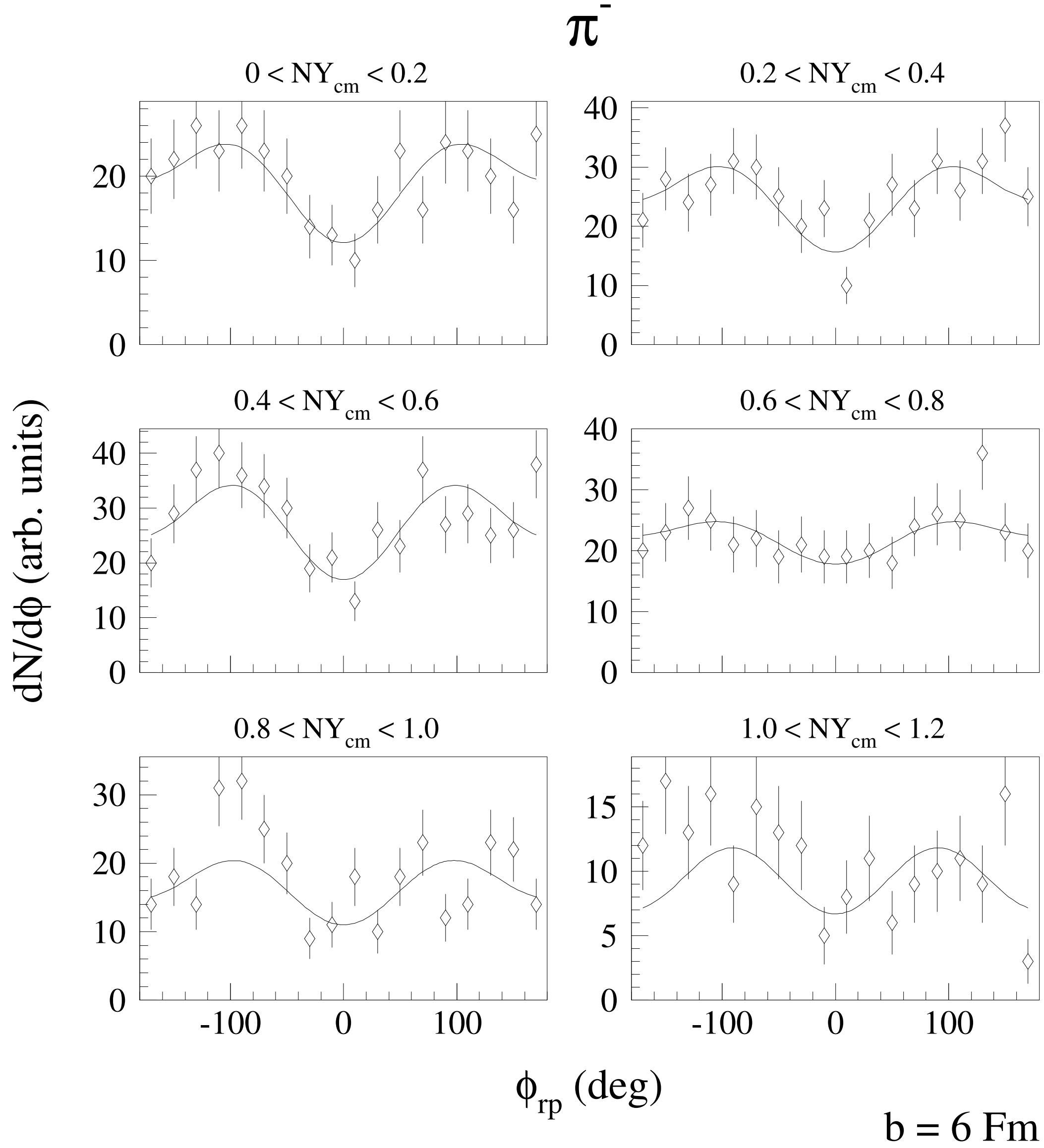

π-
0 < NYcm < 0.2
0.2 < NYcm < 0.4
0.4 < NYcm < 0.6
0.6 < NYcm < 0.8
0.8 < NYcm < 1.0
1.0 < NYcm < 1.2
dN/dφ (arb. units)
φrp (deg)
b = 6 Fm

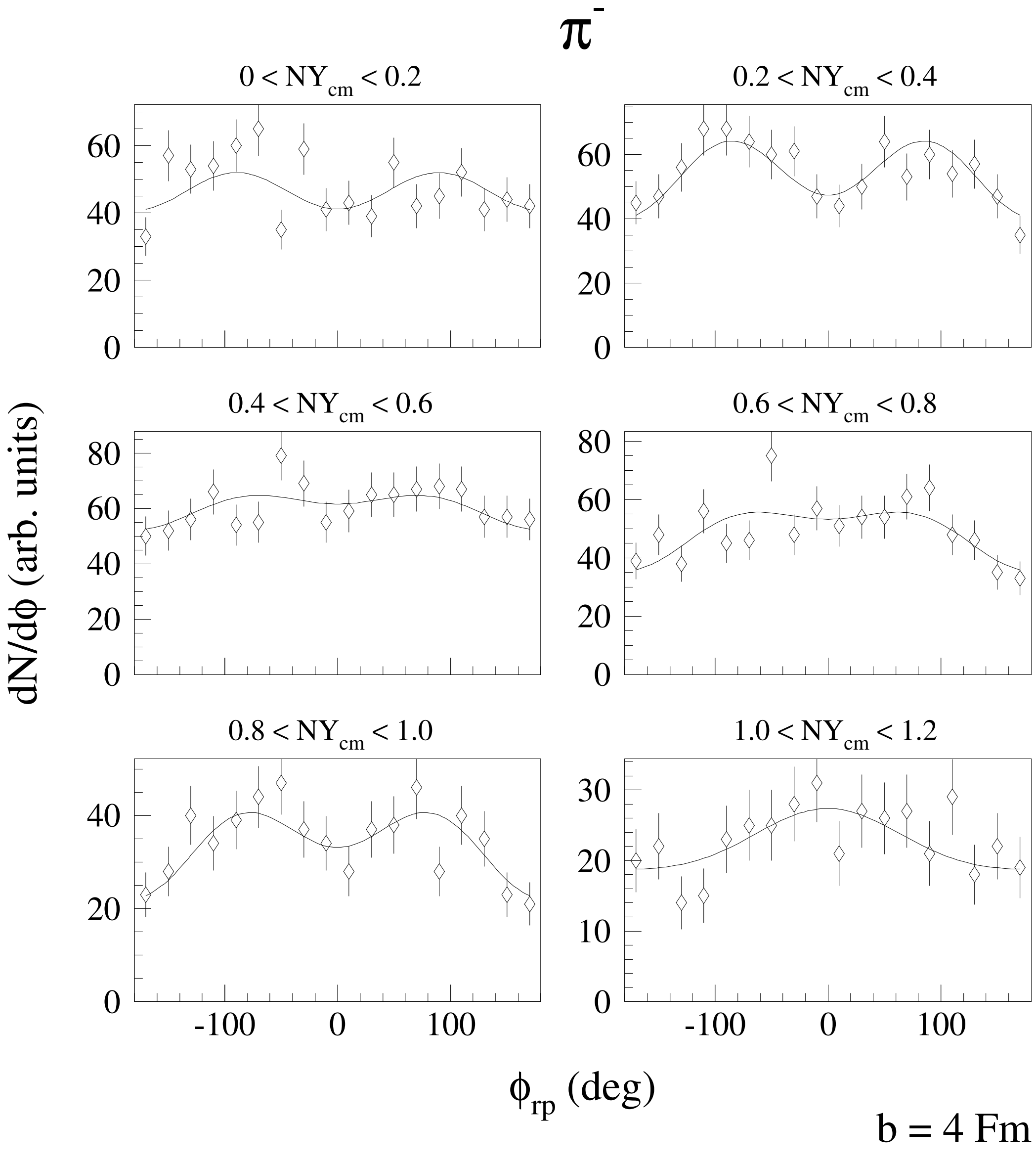

π-
0 < NYcm < 0.2
0.2 < NYcm < 0.4
0.4 < NYcm < 0.6
0.6 < NYcm < 0.8
0.8 < NYcm < 1.0
1.0 < NYcm < 1.2
dN/dφ (arb. units)
φrp (deg)
b = 4 Fm

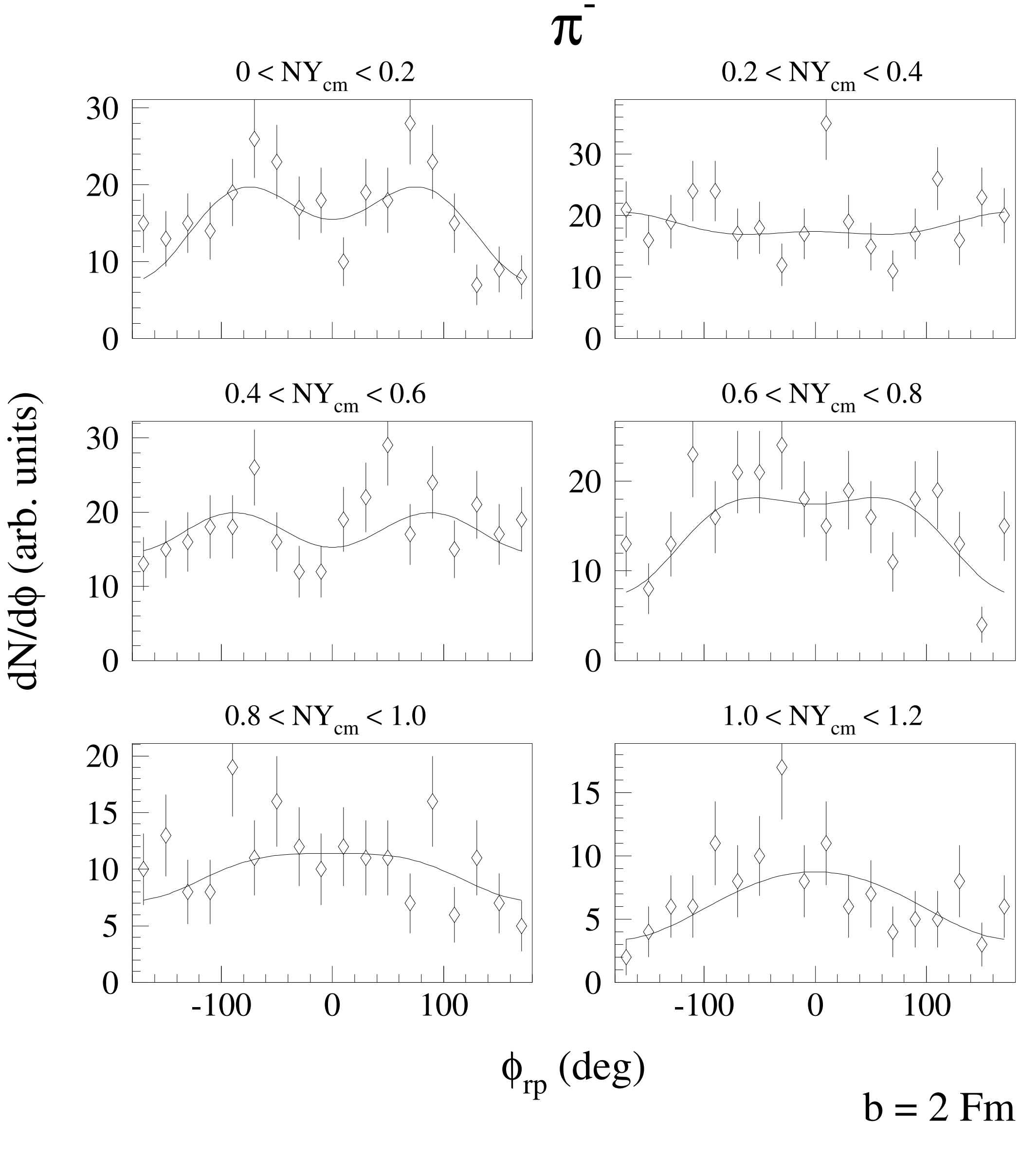

π⁻
0 < NY_cm < 0.2
0.2 < NY_cm < 0.4
0.4 < NY_cm < 0.6
0.6 < NY_cm < 0.8
0.8 < NY_cm < 1.0
1.0 < NY_cm < 1.2
dN/dφ (arb. units)
φ_rp (deg)
-100
0
100
b = 2 Fm

Bibliography

[Aich86] J. Aichelin and H. Stöcker, "Quantum Molecular Dynamics — a Novel Approach to n-body Correlations in Heavy Ion Collisions," *Physics Letters B*, 176(5):14, 1986.

[Albe92] S. Albergo, S. Costa, M Mazzeo, D. Nicotra, G Poli, R. Potenza, C. Tuve, H.J. Crawford, and I. Flores, "Position Sensitive Scintillator Discs for Intermediate and High Energy Neutron Spectroscopy," *Nuclear Instruments and Methods*, A(311):280, 1992.

[Alli80] W.W. Allison and J.H. Cobb, "Relativistic charged particle identification," *Annual Review of Nuclear and Particle Science*, 30(253), 1980.

[Baro85] E. Baron, J. Cooperstein, and S. Kahana, "Type-II Supernovae in 12M$\odot$ and 15M$\odot$ Stars: The Equation of State and General Relativity," *Physical Review Letters*, 55(1):126, 1985.

[Bass93] S.A. Bass, R. Mattiello, H. Stöcker, W. Greiner, and C. Hart *Physics Letters B* 302:381, 1993.

[Bass93b] S.A. Bass, C. Hartnack, H. Stöcker, and W. Greiner, "Out-of-Plane Pion Emission in Relativistic Heavy-Ion Collisions: Spectroscopy of Δ Resonance Matter," *Physical Review Letters*, 71(8):1144, 1993.

[Bass95] S.A. Bass, C. Hartnack, H. Stöcker, and W. Greiner, "Azimuthal correlations of pions in relativistic heavy ion collisons at 1 GeV/nucleon," Preprint from LANL preprint server.

[Bass95b] S.A. Bass, C. Hartnack, H. Stöcker, and W. Greiner, "π-N Correlations Probe the Nuclear Equation of State in Relativistic Heavy-Ion Collisions," *Physical Review C*, 51(1):R12, 1995.

[Bogu83] J. Boguta and H. Stöcker, *Physics Letters*, 120B:289, 1983.

[Byst78] J. Bystricky and F. Lehar, *Nucleon-Nucleon Scattering Data Nr. 11-1*, (Fachinformationszentrum, Karlsruhe), 1978.

[Bert84] G.F Bertsch, H. Kruse, and S. Das Gupta, "Boltzmann Equations for Heavy Ion Collisions," *Physical Review C*, 29(2):673, 1984.

[Bert88] G.F. Bertsch and S. Das Gupta, "A Guide to Microscopic Models for Intermediate Energy Heavy Ion Collisions," *Physics Reports*, 160(4):189, 1988.

[Bies91] F. Bieser, R. Jones, and C. McParland, "Data links for the EOS TPC," *IEEE Trans. on Nuclear Science*, 38(2):335–336, 1991.

[Blai76] J.P. Blaizot, D. Gogney, and B. Grammaticos, "Nuclear Compressibility and Monopole Resonances," *Nuclear Physics A*, 265:315-336, 1976.

[Bran79] S. Brandt and H.D. Dahmen, "Axes and Scalar Measures of Two-Jet and Three-Jet Events," *Zeitschrift für Physik C*, 1:61, 1979.

[Bril93] D. Brill *et al.*, "Azimuthually Anisotropic Emission of Pions in Symmetric Heavy-Ion Collisions," *Physical Review Letters* 71:336, 1993.

[Broc84] R. Brockmann, J.W. Harris, A. Sandoval, R. Stock, H. Ströbele, G. Odyniec, H.G. Paugh, L.S. Schroeder, R.E. Renfordt, D. Schall, D. Bangert, W. Rauch, and K. L. Wolf, "Pion and Proton "Temperatures" in Relativistic Heavy-Ion Reactions," *Physical Review Letters*, 53(21):2012, 1984.

[Brun91] R. Brun, F. Bruyant, M. Maire, A. C. McPherson, and P.Zanarini, "GEANT3: Users's Guide," the CERN computing center; distributed as an electronic document, so there is no publisher in the usual sense, 1991.

[Buch84] G. Buchwald, G. Graebner, J. Theis, J. Maruhn, W. Greiner, and H. Stöcker, "Kinetic Energy Flow in Nb(400*A MeV)+Nb: Evidence for Hydrodynamic Compression of Nuclear Matter," *Physical Review Letters*, 52(18):1594, 1984.

[Chri87] W.B. Christie, J.L. Romero, F.P. Brady, C.E. Tull, C.M. Costaneda, E.F. Barasch, H.J. Crawford, I. Flores, D.E. Greiner, P.J. Lindstrom, H. Sann, and J.C. Young, "A Multiple Sampling Ionization Chamber (MUSIC) for Measuring the Charge of Relativistic Heavy Ions," *Nuclear Instruments and Methods*, A(255):466, 1987.

[Cugn80] J. Cugnon, *Physical Review C*, 22:1885, 1980.

[Cugn81] J. Cugnon, T. Mizutani, and J. Vandermeulen, *Nuclear Physics A*, 352:505, 1981.

[Cugn88] J. Cugnon and M.C. Lemaire, *Nuclear Physics A*, 489:781, 1988.

[Dani83] P. Danielewicz and M. Gyulassy, "Jacobian Free Global Event Analysis," *Physics Letters B*, 129B(5):283, 1983.

[Dani85] P. Danielewicz and G. Odyniec, "Transverse Momentum Analysis of Collective Motion in Relativistic Nuclear Collisions," *Physics Letters B*, 157B(2-3):146-150, 1985.

[Dani88] P. Danielewicz, H. Ströbele, G. Odyniec, D. Bangert, R. Bock, R. Brockmann, J.W. Harris, G.G. Pugh, W. Rauch, R.E. Renfordt, A. Sandoval, D. Schall, L.S. Schroeder, and R. Stock, "Collective motion in nucleus-nucleus collsions at 800 MeV/nucleon," *Physical Review C*, 38(1):120, 1988.

[Dani91] P. Danielewicz and G.F. Bertsch, "Production of Deuterons and Pions in a Transport Model of Energetic Heavy-Ion Reactions," *Nuclear Physics A*, 533:712, 1991.

[DasG79] S. Das Gupta and C.S. Lam, *Physical Review C*, 20:1192, 1979.

[Enge88] J. Engelage *et al.*, "Design of the Bevalac Heavy Ion Spectometer System and its Performance in Studying ^{12}C Fragmentation," *Nuclear Instruments and Methods in Physics Research*, A(277):431–444, 1988.

[Enge94] A. Engel, W. Cassing, U. Mosel, M. Schäfer, and Gy. Wolf, *Nuclear Physics A*, 572:657, 1994.

[Fern86] R.C. Fernow, *Introduction to Experimental Particle Physics*, Cambridge University Press, 1986.

[Glen86] N.K. Glendenning, "Neutron Star Masses as a Constraint in the Nuclear Compression Modulus," *Physical Review Letters*, 57(9):1120, 1986.

[Goss77] J. Gosset, H.H. Gutbrod, W.G. Meyer, A.M. Poskanzer, A Sandoval, R. Stock, and G.D. Westfall, *Physical Review C*, 16:629, 1977.

[Goss89] J. Gosset, O. Valette, J.P. Alard, J. Augerat, R. Babinet, N. Bastid, F. Brochard, N. DeMarco, P. Dupieux, Z. Fodor, L. Fraysse, P. Gorodetzky, M.C. Lemaire, D. L'Hôte, B. Lucas, J. Marronele, G. Montarou, M.J. Parizer, J. Poitou, C. Racca, A. Rahmani, W. Schimmerling, and Y. Terrien, "Nuclear Collective Flow and Charged-Pion Emission in Ne-Nucleus Collisions at E/A=800 MeV," *Physical Review Letters*, 62:1251, 1989.

[Gust84] H.A. Gustafsson, H.H. Gutbrod, B. Kolb, H. Löhner, B. Ludewigt, A.M. Poskanzer, T. Renner, H. Riedesel, H.G. Ritter, A. Warwick, F. Weik, and H. Wieman, "Collective Flow Observed in Relativistic Nuclear Collisions," *Physical Review Letters*, 52(18):1590, 1984.

[Gutb90a] H.H. Gutbrod, K.H. Kampert, B. Kolb, A.M. Poskanzer, H.G. Ritter, R. Schicker, and H.H. Schmidt, "Squeeze-out of nuclear matter as a function of projectile energy and mass," *Physical Review C* 42(2):640, 1990.

[Gyul82] M Gyulassy, K.A. Frankel, and H. Stöcker, "Do Nuclei Flow at High Energies?," *Physics Letters B*, 110(3-4):185, 1982.

[Hahn85] D. Hahn and H. Stöcker, MSUCL-535, 1985.

[Hart88] C. Hartnack, H. Stöcker, and W. Greiner, in Proceedings of the International Workshop on Gross Properties of Nuclei and Nuclear Excitations XVI, Hirschegg, Austria, edited by H. Feldmeier, GSI Report, ISSN 0720-8715, p. 138, 1988.

[Hufn77] J. Hüfner and J. Knoll, *Nuclear Physics A* 290:460, 1977.

[Kaha95] D. Kahana, D. Keane, Y. Pang, T. Schlagel, and S. Wang, "Collective Flow from the Intranuclear Cascade Model," *Physical Review Letters*, 74(22):4404, 1995.

[Kean86] D. Keane, *et al.*, Proceedings of Nuclear Dynamic Workshop IV, editor V. Viola (conf - 860270), p. 151, 1986.

[Klei88] S.A. Kleinfelder, "Development of a Switched Capacitor Based Multi-Channel Transient Waveform Recording," *IEEE Trans. on Nuclear Science*, 35:151, 1988.

[Klei90] S.A. Kleinfelder, "A 4096 Cell Switched Capacitor Analog Waveform Storage Integrated Circuit," *IEEE Trans. on Nuclear Science*, 37:1230, 1990.

[Leif93] Y. Leifels *et al.*, "Exclusive Studies of Neutron and Charged Particle Emissions in Collisions of $^{1}97$Au + $^{1}97$Au at 400 MeV/Nucleon," *Physical Review Letters* 71:963, 1993.

[Li91] B.-A. Li and W. Bauer, "Pion spectra in a hadronic transport model for relativistic heavy ion collisions," *Physical Review C* 44(1):450, 1991.

[Li91b] B.-A. Li and W. Bauer, *Physical Review C* 44:2095, 1991.

[Lync83] W.G. Lynch and W.A. Friedman, *Physical Review C*, 28:16, 1983.

[Moli85] J.J. Molitoris and H. Stöcker, "Further evidence for a Stiff Nuclear Equation of State from a transvers-momentum analysis of Ar(1800 MeV/nucleon) + KCl," *Physical Review C*, 32:346, 1985.

[Myer78] W.D. Myers, *Nuclear Physics A* 296:177, 1978.

[Naka91] M. Nakamura, D.A. Landis, and G. Rai, "Low Power Shaper Amplifier for the EOS TPC Detector," *IEEE Trans. on Nuclear Science*, 38(2):50–52, 1991.

[Part90] The Particle Data Group, "Review of particle properties. *Physics Letters B*, 239(III.23), 1990.

[Part94] M.D. Partlan, "Collective Flow in Au + Au Collisions with Incident Energies from 0.25 to 1.15 A GeV," Graduate Thesis, 1994.

[Part94b] M.D. Partlan and the EOS Collaboration, "Fragment Flow in Au + Au Collisions," Submitted to *Physical Review Letters*, 1994.

[Perk87] Donald H. Perkins, *Introduction to High Energy Physics*, Addison-Wesley Publishing Company, Inc., 1987.

[Regl90] M. Regler and R. Fruhwirth, "Reconstruction of charged tracks," in Thomas Ferbel, editor, *NATO Advanced Study Institute on Techniques and Concepts of High-Energy*, p 407, Plenum Press, 1990.

[Sche74] W. Scheid, H. Müller, and W. Greiner, "Nuclear Shock Waves in Heavy-Ion Collisions," *Physical Review Letters*, 32(13):741, 1974.

[Scot93] A. Scott, "dE/dx Resolution and Gas Gain in the EOS TPC," *EOS Internal Report*, 1993.

[Serb47] R. Serber, *Physical Review*, 72:1114, 1947.

[Stoc82] R. Stock, R. Bock, R. Brockman, J.W. Harris, A. Sandoval, H. Stroebele, K.E. Wolf, H.G. Pugh, L.S. Schröder, M. Maier, R.E. Renfordt, A. Dacal and M.E. Ortiz, *Physical Review Letters*, 49:1236, 1982.

[Stoc86] H. Stöcker and W. Greiner, "High Energy Heavy Ion Collisions — Probing the Equation of State of Highly Excited Hadronic Matter," *Physics Reports*, 137(5-6):277-392, 1986.

[Trza94] M. Trzaska, D. Best, J. Bieganski, T. Engelhardt, M. Gnirs, A. Gobbi, G. Goebels, E. Häfele, N. Herrmann, K.D. Hildenbrand, H. Marlitz, S. Mohren, D. Pelte, Ch. Pinkenburg, and D. Schüll, "Pion Production Studies with FOPI," *Proceedings of the XXXII International Winter Meeting on Nuclear Physics*, Editor I. Iori, 1994.

[Uehl33] E.A. Uehling, and Uhlenbeck, *Physical Review*, 43:552, 1933.

[Vene93] L.B. Venema, H. Braak, H. Löhner, A.E. Raschke, R.H. Siemssen, M. Sumbera, H.W. Wilschut, F.-D. Berg, W. Kühn, V. Metag, M. Notheisen, R. Novotny, M. Pfeiffer, J. Ritman, O. Schwalb, A. Gobbi, K. D. Hildenbrand, S. Hlavac, R. Holzmann, R.S. Simon, U. Sodan, K. Teh, J.P. Wessels, N. Herrmann, T. Wienold, R. Kotte, J. Mösner, W. Neubert, D. Wohlfarth, R. Ostendorf, Y. Schutz, N. Brummund, and R. Santo, "Azimuthal Asymmetry of Neutral Pion Emission in Au + Au Reactions at 1 GeV/nucleon," *Physical Review Letters* 71(6):835, 1993.

[VerW82] B.J. VerWEst and R.A. Arndt, "NN Single Pion Production Cross Sections below 1500 MeV," *Physical Review C*, 25:1979, 1982.

[West76] G.D. Westfall, J. Gosset, P.J. Johansen, A.M. Poskanzer, W.G. Meyer, H.H. Gutbrod, A. Sandoval, and R. Stock, *Physical Review Letters*, 37:1202, 1976.

[Wu79] S.L. Wu and G. Zobernig, "A Method of Three jet Analysis in e^+e^- Annihilation," *Zeitschrift für Physik C*, 2:107, 1979.

[Yari79] Y. Yariv and Z. Frankel, *Physical Review C*, 20:2227, 1979.